Universidade de Aveiro Departamento de Química
2017

Joana Maia Miranda

Síntese, caracterização e avaliação do desempenho de aditivos nanoestruturados com propriedades anti-corrosivas no betão armado

Synthesis, characterization and performance evaluation of nanostructured additives with anti-corrosive properties in reinforced concrete

Universidade de Aveiro Departamento de Química
2017

Joana Maia Miranda

Síntese, caracterização e avaliação do desempenho de aditivos nanoestruturados com propriedades anti-corrosivas no betão armado

Synthesis, characterization and performance evaluation of nanostructured additives with anti-corrosive properties in reinforced concrete

dissertação apresentada à Universidade de Aveiro para cumprimento dos requisitos necessários à obtenção do grau de Mestre em Engenharia Química, realizada sob a orientação científica da Doutora Ana Luísa Daniel Silva, Investigadora Auxiliar do Departamento de Química da Universidade de Aveiro e orientação da Doutora Cláudia Manuela Mesquita da Rocha e do Doutor Frederico Calheiros Maia, da Smallmatek, Lda.

o júri

presidente

Professor Doutor Carlos Manuel Santos da Silva
Professor Auxiliar do Departamento de Química da Universidade de Aveiro

Doutora Márcia Carvalho Neves
Investigadora de Pós-doutoramento, CICECO da Universidade de Aveiro

Doutor Frederico Calheiros Maia
Diretor de Investigação e Desenvolvimento da Smallmatek, Lda.

agradecimentos

Gostaria de exprimir algumas palavras de agradecimento à minha família, que sempre acreditou em mim; aos meus melhores amigos/irmãos, por toda a curiosidade, paciência e apoio (uma *boss*); ao meu namorado, por toda a jornada que ambos temos caminhado; a todos os meus colegas e amigos da Smallmatek, por todo o bom ambiente, por me fazerem sentir parte de vós; aos meus três Maravilhosos orientadores que me ajudaram bastante durante todo o trabalho e a todas as outras pessoas que tornaram este trabalho possível.
Acreditem do fundo do meu ser que sozinha não teria conseguido chegar aqui.
A minha gratidão é diária e enorme para com todos vós.

palavras-chave Hidróxidos duplos lamelares, inibidores, corrosão, betão armado

resumo

Este trabalho tem como objetivo aplicar hidróxidos duplos lamelares (LDHs) intercalados com inibidores de corrosão em betão armado por forma a proteger as estruturas de aço da corrosão e aumentar a longevidade do mesmo. Para tal, foram sintetizados LDH-NO_3 e LDH-NO_2. A partir da suspensão de LDH-NO_3, procedeu-se à intercalação com iões citrato e tartarato. Todas as amostras foram caracterizadas utilizando técnicas como espetroscopia de FT-IR, X-RD, potencial zeta, DLS, SEM/TEM e ICP. Realizaram-se estudos de libertação, colocando, em agitação, alíquotas de soluções aquosas de cloreto de sódio (NaCl) às concentrações de 5, 50 e 500 mM com LDH em pó. Recolheram-se alíquotas durante um mês e analisaram-se as amostras por cromatografia líquida (HPLC), para determinar as concentrações dos inibidores em solução ao longo do tempo. Procedeu-se, ainda, a estudos de impedância eletroquímica para avaliação do desempenho dos materiais na prevenção do ataque corrosivo ao aço. Para tal, expôs-se uma placa de aço a suspensões de diferentes concentrações de espécie agressiva (ião cloreto) com LDHs e mediram-se os valores de impedância ao longo do tempo. Com este trabalho conseguiu-se avaliar o desempenho anticorrosivo de diferentes aniões, além dos já conhecidos, e perceber quais trariam vantagens com o seu uso. Observou-se que nas suspensões com maior concentração de espécie agressiva, a libertação de inibidor foi superior. Através dos espetros de FT-IR e imagens de SEM/TEM, depreendeu-se que a encapsulação decorreu com sucesso. Apesar de não se ter tido oportunidade de testar o desempenho dos materiais encapsulados, seria um ponto vantajoso no desenvolvimento do trabalho.

Key-words Layered double hydroxide, inhibitors, corrosion, reinforced concrete

Abstract

This work consisted in the preparation and characterization of layered double hydroxides (LDHs) intercalated with corrosion inhibitors with the purpose of including them in concrete, to protect steel from corrosion and increase concrete's longevity. LDH-NO_3 and LDH-NO_2 were synthesized and, using, LDH-NO_3 suspension, intercalation with citrate and tartrate ions was performed. All samples were characterized using FT-IR spectroscopy, X-RD, Zeta potential measurements, DLS, SEM/TEM and ICP. Release studies were performed, mixing NaCl solution at different concentrations (5, 50, 500 mM) with each LDH sample. Several aliquots were collected over a month and analysed by HPLC to determine the concentration of inhibitors released over time. Electrochemical impedance studies were performed to evaluate the performance of LDHs intercalated with inhibitors against steel corrosion. Thus, a carbon steel board was exposed to a suspension with the aggressive specie (chloride ion) at different concentrations and LDHs. Impedance data was collected over time. Therefore, it was possible to analyse the pertinence of the inclusion of the tested materials into concrete's mixture, when comparing their action against the corrosive process. It was verified that for suspensions with higher concentrations in aggressive specie, the release of the inhibitor was superior. Through FT-IR spectra and SEM/TEM images, it was concluded that the encapsulation occurred successfully. Even though the performance of the functionalized materials was not tested, it would be advantageous for the on-going development of the work.

Table of Contents

List of Figures

List of Tables

List of Appendix Figures

List of Abbreviations

5-ASA – 5-aminosalicylic acid;
AA2024 – Aluminium alloy 2024;
ATR – Attenuated total reflectance;
BS – Basal spacing;
CSA – Calcium sulphoaluminate;
CTAB - Cetyltrimethylammonium bromide;
DLS – Dynamic light scattering;
DNA – deoxyribonucleic acid;
EDS – Energy dispersive spectroscopy;
EIS – Electrochemical electron spectroscopy;
FTIR – Fourier transformer infra-red;
FWHM – Full width at half-maximum;

GPTMS - 3-glycidoxypropyltrimethoxysilane;

HPLC – High performance liquid performance;

HT – Hydrotalcite;

ICP-AES – Induced coupled plasma- atomic emission spectroscopy;

K – Scherrer constant;

L – Crystallite size;

LC – Liquid column chromatography;

LDH – Layered double hydroxide;

PC – Paper chromatography;

SEM – Scanning electron microscopy;

STEM – Scanning transmission electron microscopy;

TEM – Transmission electron microscopy;

TEOS – Tetraethylorthosilicate;

TGA – Thermogravimetric analysis;

TLC – Thin layer chromatography;

TPOZ - Tetra-n-propoxyzirconium;

UV – Ultra-violet;

XRD – X-ray diffraction;

ZP –Zeta potential.

Introduction

Concrete has numerous applications and utilities, being large support structures and constructions the most interesting for this work. However, steel corrosion in concrete is one of the most frequent problems faced. To increase reinforced concrete lifetime, the performance of layered double hydroxide intercalated with potential corrosion inhibitors has been studied and evaluated, as well as the pertinence of its integration in the concrete mixture. The corrosion inhibitors chosen were nitrite, citrate and tartrate anions.

This thesis is divided in four main chapters. The first section includes the state of the art, which reports information about layered double hydroxides (LDHs) and its main characteristics and application areas, specifically, in concrete structures and its ability to avoid corrosion problems, followed by the thesis main objectives. In the second chapter, is reported the experimental procedure of LDHs synthesis and characterization of the obtained materials. The third section includes the interpretation and discussion of the results obtained from the characterization techniques used and the evaluation performance of the corrosive inhibitors obtained by release tests and electrochemical impedance spectroscopy (EIS). In the last chapter, the conclusions inferred from the work developed and future expectations for this assignment are exposed.

1. State of the art

1.1. Layered Double Hydroxides (LDH)

Layered double hydroxides (LDHs), also called hydrotalcite (HT)-like materials or anionic clays are a family of materials that have been scrutinized for the past years, mainly due to their versatile utilization [1],[2]. They integrate a group of minerals called 'non-silicate oxides and hydroxides' [3].

1.1.1. LDH structure

The formula of the LDH can be generalized to $[M_{1-x}^{2+}M_x^{3+}(OH)_2]^{x+}[A_{x/n}^{n-}.mH_2O]^{x-}$, where M represents metallic ions M^{2+} such as Ni^{2+}, Zn^{2+}, Mn^{2+}; and M^{3+}, Al^{3+}, Ga^{3+}, Fe^{3+}; and A^{n-} represents an interlamellar anion that can be: NO_3^-, Cl^-, CO_3^{2-} [1].

The structure of these materials consists of layers with similar arrangement to brucite, $Mg(OH)_2$, with octahedral units of cations encircled by edge-sharing hydroxide ions, where some divalent cations are replaced by trivalent cations, which attributes a residual positive charge to the layers.

These external positive charges are balanced by the interlamellar anions and water molecules, that are weakly bounded to the hydroxyl groups through hydrogen bonds, electrostatic effects and dispersive forces [4]. The result is a three-dimensional structure that can be observed below in Figure 1. Usually, synthetic LDH have hexagonal units, unless when the ratio between M^{2+} and M^{3+} is equal to 1. In this situation, the cell exhibit an orthorhombic shape [5].

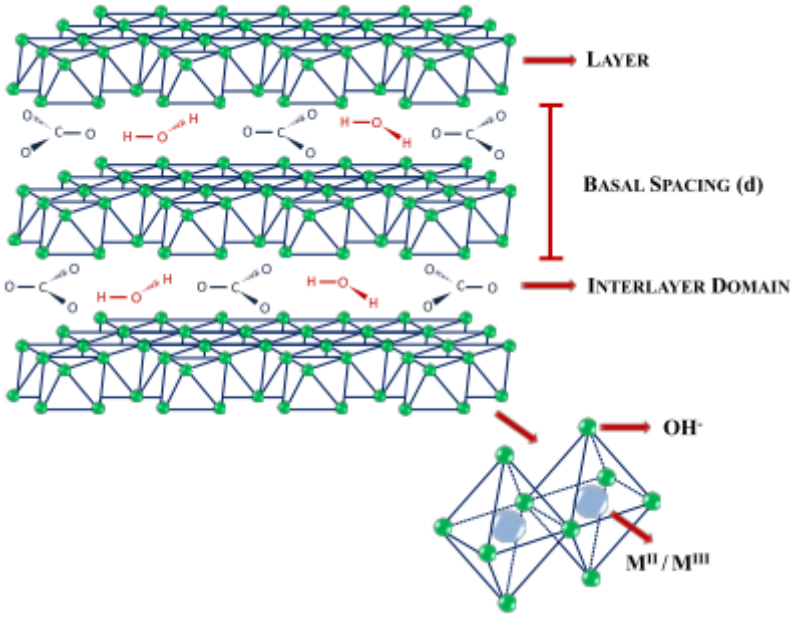

Figure 1: Layered Double Hydroxides structure scheme [5].

1.1.2. LDH methods of synthesis and morphologies

The most frequent methods of LDH preparation are co-precipitation, ion-exchange method, rehydration using structural memory effect and hydrothermal method. Co-precipitation is by far the most commonly used technique, being the production possible to scale up. The mechanism is based on the condensation of hexaaquo complexes in solution to produce brucite-like layers, resulting in a well distributed arrangement of metallic cations and solvated interlamellar anions. The performed thermal treatment process that follows the reaction aim an increase of yields and/or the crystallinity of amorphous or badly crystallized materials. The ion-exchange method is especially needed when co-precipitation is unsuitable, for example, when the divalent or trivalent metal cations or anions involved are unstable in alkaline solution, or the direct reactions between metal ions and guest anions is more favourable. Using this methodology, the guests are exchanged with the anions present in the interlayer regions, to obtain specific anion pillared LDHs. The rehydration using structural memory effect is interesting, because it makes possible the regeneration of the layered structure. After calcination of previously prepared LDHs, the water, anions and the hydroxyl groups from the interlayer are removed, achieving a mixed metal oxide. When water is absorbed, the hydroxyl layers are restored and anions and water integrate again the interlayer galleries. The hydrothermal treatment is used to control the particle size and its distribution when magnesium and aluminium salts are used together, specifically [6].

According to Kuang et al. [7], LDH can be presented in different forms such as:

- Powdery: Gursky et al. produced nanosized colloidal MgAl-LDH particles through co-precipitation with metal salts dissolved in methanol in the presence of NaOH [8]. O'Hare et al. used microemulsions and prepared very small LDH particles in isooctane-sodium dodecyl sulphate/aqueous solution and a 14 Å thick LDH monolayer [9]. Xu et al. also prepared MgAl-LDH by co-precipitation and included a controlled hydrothermal treatment in the process, producing LDH platelets in a dimensional size range of 30 to 500 nm [10].

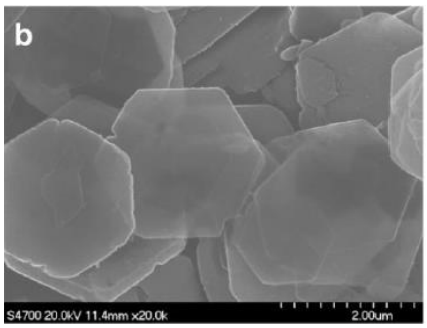

Figure 2: Scanning electron microscope (SEM) image of typical LDH crystals [7].

- Spherical structure: this structure is achieved mainly through template-direct synthesis using soft and hard templates. Their main applications are in catalysis, sorption, battery electrodes and carriers for cellular drug and gene delivery.

- 1-D nanostructures: the structure mentioned is obtained through the control of nucleation and growth of LDH crystals, as nanobelts or fibrous structures (Figure 3).

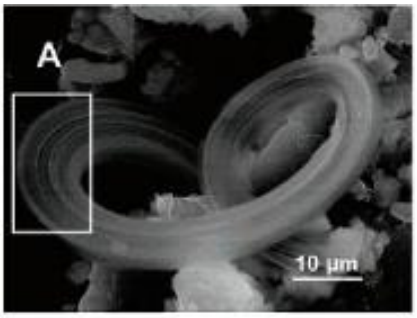

Figure 3: SEM image of a belt-like structure with parallel linear pattern (highlighted in the white rectangle) [7].

- 2-D films: when fabricating this well-oriented or self-supporting LDH films, the natural aggregation of LDH powders is prevented.
  - Parallel-oriented LDH films: the direct ways to prepare LDH films are solvent evaporation and colloid deposition technique. The LDH nanosheets are evenly scattered in the solvent, which can be methanol, ethanol or water. This approach shows a great adherence between substrates and LDHs (Figure 4).

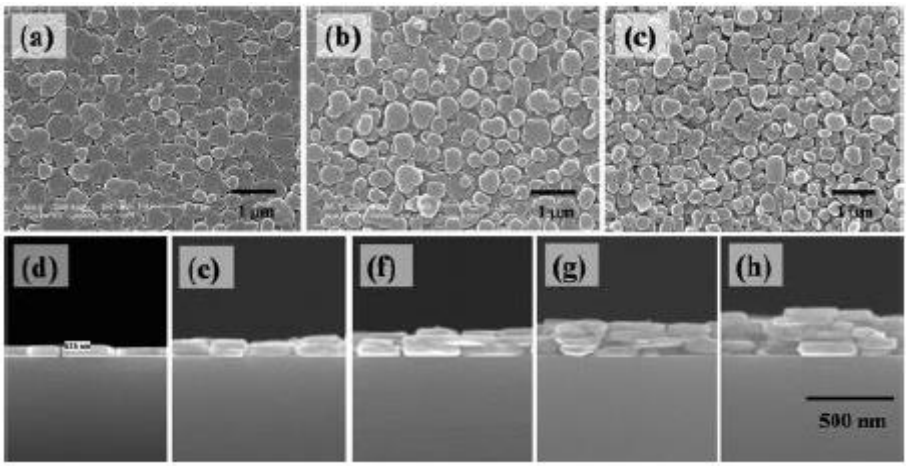

Figure 4: SEM images of LbL LDH nanocrystals: 1 layer (L) (a); 3 L (b); and 5 L MgAl-LDH/Si (c); Cross-sectional views of 1 L (d); 2 L (e); 3 L (f); 4 L (g) and 5 L (h) samples [7].

- Perpendicular-oriented LDH films: these films are usually composed of edge-on oriented LDH platelets [7]. Lei et al. studied the production of edge-on oriented MgAl-LDH thin films with microscale thickness on the sulfonated PS flat substrates via urea hydrolysis reaction at 70-80 ºC over more than eight days. They concluded that for highly sulfonated substrates, the (00*l*) direction of the MgAl-LDH platelets is perpendicular to the surface (Figure 5).

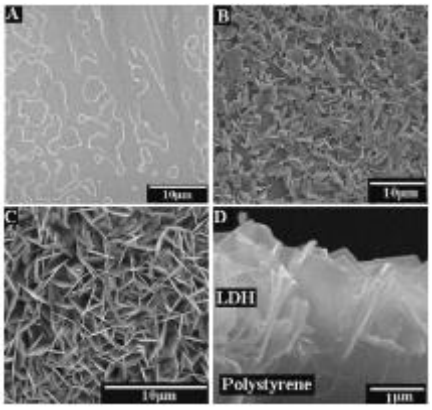

Figure 5: SEM graphs for basal surface of (I) type samples on polystyrene substrates for 0 h (A), 24 h (B), and 72 h (C), edge of the samples on substrate sulfonated for 72 h (D) [11].

1.1.3. Main Characteristics and Applications

Throughout the previous sections, it has been mentioned the versatile and various properties and uses of LDH based materials, which will be exposed in the following topics.

1) Thermal Stability

Hydrotalcite-like compounds are very stable when exposed to high temperatures, up to 400 ºC. If the material is exposed to a range of temperatures between 500-800 ºC, the hydroxides of the double layer easily oxidize. The mixture can restore the hydrated initial form and recombine the anions to form again HT. It is observed that when LDH have organic anions intercalated, the thermal stability is higher relatively to the free organic anion.

2) Anion Exchange ability

Due to their high anion-exchange capacity and ability to retain organic and inorganic anions, LDHs became one of the most interesting inorganic materials. For systems with colloidal characteristics, it is very important the small particle size and low charge density of some LDHs.

3) Morphology, surface area, porosity and particle size

These physical properties are vital to describe LDH and define its applications. However, they are dependent of the method of synthesis used, as mentioned above. The morphology can be analysed using Scanning Electron Microscopy (SEM). Depending on composition and crystallinity differences, the particle sizes of LDH can vary [5].

4) Layer rigidity

To the space between the host layers is called gallery and usually contains the guest species that can permute with anionic species to maintain overall electroneutrality. The interlayer rigidity parameter connects the changes in the anionic concentration within the guest layer and the change in basal spacing. Since the cation substitution in the host layer wasn't quantified, the concept of interlayer rigidity appears to explain the cation substitution within the host layer [12].

The characteristics mentioned above reveal some of the reasons to the application of layered double hydroxides in some application areas for our times. It can be applied to thermal stability, catalyst supports, as an intermediate in organic reactions, adsorption processes and ion-exchange, medicine, pharmaceuticals utilities and procedures, and corrosion prevention and fighting.

Thermal stability

Lin et al. studied the integration of MgAl-LDH-CO_3 in a PVC resin with different Mg/Al ratio and concluded that with the increase of Mg/Al ratio, the electrostatic force of attraction between layers and interlayer counter-ions and the driving force for ion exchange decrease. It was Kyowa chemical Industries that tested firstly this hypothesis and observed that the addition of MgAl-LDH-CO_3 to PVC resin in combination with other additives increased the thermal stability of the resin [13]. Nyambo et al. applied phosphonate-intercalated MgAl-LDH into EVA-based materials with the intention of preventing premature decomposition of phosphorus-containing additives, which is vastly studied as flame retardant additive. Therefore, the use of EVA in daily materials became possible, avoiding the release of large quantities of toxic smoke when exposed to high temperatures [14].

Catalyst supports

Due to LDHs properties, they can be synthetized in an easy and inexpensively form and used as catalyst support, precursor or a catalyst. It is not a novelty that, throughout the years, it has been shown the utility and effectiveness of LDHs in catalysis. Published works reported MgCoAl-LDH-derived heterogeneous catalyst used for ethanol transesterification [15]; noble metallic metals LDHs were used for methane reforming [16] and, latterly, LDHs and their organic-derived products can behave as supports for immobilisation of enzymes [2].

Intermediate in organic reactions

Throughout the years, many researchers have reported the large utility and versatility of LDHs, from photo-inhibitor complexes in UV curing systems and flame retardant additives in coatings to drug containers and catalyst carriers [17]. Combining polymer materials and LDH, nanocomposites can be prepared with advanced mechanical and thermal properties, enormous chemical stability and diminished flammability, such as using a silsesquioxane complex [17], a modified Mg-Al

hydrotalcite as the base catalyst of Michael additions [18] or apply them on Friedl-Crafts alkylations [19].

Adsorption

LDHs have great properties of anion-exchange and surface adsorption, if the species in question have an anionic character. Thus, the sorption applications are limitless, from water residues, medical/industrial residues [20] to sulphur residues produced in fuels treatments [21] and rare earth elements capture [22].

Medicine and Pharmaceuticals

Primarily, LDHs were applied in the medical field mainly as antacid and antipepsin agents [2] and, throughout the years, the growth of medical innovation demanded research, evolution and solutions- as new alternatives for controlled and selective release of drugs are still emerging. For example, Ribeiro et al. used an intercalated MgAl-LDH with 5-ASA (5-aminosalicylic acid) and incorporated it into a chitosan matrix to enhance its mucoadhesiveness to the treatment of colon diseases [23]. Recently, it has been studied the use of LDH for drug and gene delivery carrier. Evans et al. produced NiAl, MgAl and ZnAl LDHs by coprecipitation intercalated with L-Tyr and concluded that they stabilized the amino acid's racemization – process in which one enantiomer of an L-amino acid converts to the other enantiomer – under the influence of sunlight, high temperature and ultraviolet light [24]. Choy et al. found that LDHs are not employed in pharmaceuticals vastly yet. However, they can intercalate various biomolecules with negative charge such as oligomers, single or double stranded DNA and nucleotides [25].

Corrosive protection

To prevent or delay corrosion in metal surfaces, the options to integrate the inhibitors are various, since adding them directly to the matrix in contact with the metal, mixing the inhibitor in a coating to apply in the surface or loading nanoreservoirs with the inhibitive species for a prolonged release and more efficient and continuous protection.

Zhang et al. produced a coating filled with ZnAl LDH nanocontainers, which can provide self-healing effect and higher corrosion properties. They found out that the direct addiction of the inhibitors into the hybrid coatings caused easily deterioration of the materials and to avoid this situation, encapsulation has shown to be more favourable [26]. Snihirova et al. studied the inhibiting effect of LDH nanocontainers loaded with mercaptobenzothiazole, added to epoxy coatings applied on AA2024 and the use of tubular halloysites (HS) filled with 8-hydroxiquinoline and chromate pigments (Cr-reference). The use of the nanocontainers revealed to be effective at the early-stage of corrosion inhibition, while tubular halloysites loaded with inhibitor turn more effective after the first step of corrosion activity [27].

1.2. Reinforced Concrete

1.2.1. Concrete Composition

Concrete is composed by an aggregate of gravel and grit, cement, water and adjuvants, which can act as superplasticizers and/or accelerators [28]. As a superplasticizer, steel or polypropylene fibres can be added to concrete, reducing greatly concrete's workability and water/cement ratio and increase the mechanical properties of concretes [29]. Accelerators are needed to improve the setting time and the hardening rate and usually the ones selected are calcium salts (calcium chloride, nitrate, nitrite or thiocyanate), but sodium silicate or aluminate and alkali metal hydroxides are also used for this purpose [30],[31].

To assemble the mixture, binder materials are used such as:

- Hydraulic binder: it is composed by fine dust, that when stirred with water, reacts and hardens. To this cement, it is given the name of Portland's cement, one of the most common. Besides hardening in the air, it easily acquires elevated resistance under water.
- Air binder: it only hardens when exposed to air. The atmospheric carbon dioxide produces carbonate ions. It is the oldest Portland cement and no longer serves a purpose.
- "Hydrocarbons" and synthetic resin binders: these binders have an organic origin; they are incorporated into the cement, and at last, impregnated into the concrete.

Being cement one of the principal components of concrete, it is important to have a brief idea of how it is made. The main raw ingredients that compose cement are limestone and clay. These are finely grounded, homogenised and stacked in appropriate ovens at 1400-1500 ºC. The obtained product is a clinker stone, which is then powdered as fine as possible and mixed with gypsum and additives. Gypsum is added to the clinker as a controller of setting time of cement [32]. The preparation of reinforced concrete consists in fulfilling molds with concrete, where the metallic rebar is already inside. These structures can have various sizes and shapes to suit the desired usages.

1.2.2. Degradation of reinforced concrete: the impact of corrosion

The degradation of metallic structures is caused mostly by corrosion. Thus, being a problem with great economic impact, protective solutions for the infrastructures turned vital [33]. Steel is naturally less durable than concrete, which allows to infer that when the steel is encased in concrete, the probability of corrosion occurrence is expected to be highly diminished. The steel entrenched in concrete is, normally, in a passive state towards corrosion as a thin iron oxide film is formed on steel surface and remains stable at the high alkaline environment of concrete. Following, there are three main consequences that may occur: reduction of reinforcement cross section, concrete cover cracking and cleaving, as result of carbonation.

The first step of corrosion is called depassivation and occurs when this protective film is destroyed. It can happen mainly in two ways: by carbonation of concrete external layer owing to the reaction with carbon dioxide, which reduces concrete alkalinity (General corrosion) or by the chlorides attack on the steel surface (seawater, de-icing salt, unwashed sea sand, etc.) (Pitting corrosion). Once initiate the corrosion process, it can continue until total disintegration of the reinforced concrete structure [34].

The carbonation reaction occurs due to the reaction of atmospheric carbon dioxide with alkaline components of concrete. Carbon dioxide in solution forms an acid aqueous solution that can react with the hydrated cement paste, which can cause concrete alkalinity to decrease. The carbonation starts at the external surface and penetrates the concrete, decreasing its pH value. In environments with high levels of CO_2, the carbonation is accelerated. When the concrete is wet, CO_2 has more difficulty to penetrate concrete, which delays carbonation. Since the rust (corrosion product) has a lower density than the metal, it expands and origins cracking in concrete. To the breakage of concrete surface, it is called *spalling*. Sometimes, during the settlement of concrete, pockets of air or water are formed, which create below the surface, weakened spots that can disaggregate. This is also one of the most common phenomenon of concrete degradation, known as *delamination* of the concrete cover [35].

The chloride-induced localized corrosion, also known as *Pitting Corrosion* is one of the most severe and destructive forms of corrosion in reinforced concrete [35], as shown in Figure 6.

Since the signs of corrosion are hardly observable until an advanced stage, this type of corrosive process is considered dangerous, because as soon as the corrosion is detected, the cross section of the reinforcement, the loading capacity and the fatigue strength are most likely to be significantly decreased. In the presence of oxygen and humid environment, an electro-chemical process is unleashed that creates a current flow causing metal to disintegrate [36]. The areas of steel attacked by chlorides that no longer have the passive film, act as anodes (active zones) and the surroundings that are still protected, act as cathodes (passive or less active zones). In these regions occurs the cathodic reaction of oxygen reduction. In the corrosion process or galvanic corrosion, as it is also called, the two electrochemical reactions are known as ‘anodic’ (Eq.1) and ‘cathodic’ (Eq.2) reactions, to which one of the correspondent areas are called ‘anodic’ and ‘cathodic’, as mentioned above. The iron removed by an electrochemical reaction (i.e. oxidation) is dissolved in the water solution [37].

Anodic reaction (iron oxidation):

$$2\,Fe^{0} \rightarrow 2\,Fe^{2+} + 4e^{-} \quad \text{Eq.1}$$

(Metallic atoms at the steel surface) (Ions dissolved in solution)

Cathodic reaction (oxygen reduction):

$$O_2 + 2\,H_2O + 4e^{-} \rightarrow 4(OH^{-}) \quad \text{Eq.2}$$

(Dissolved oxygen molecules) (Ions dissolved in solution)

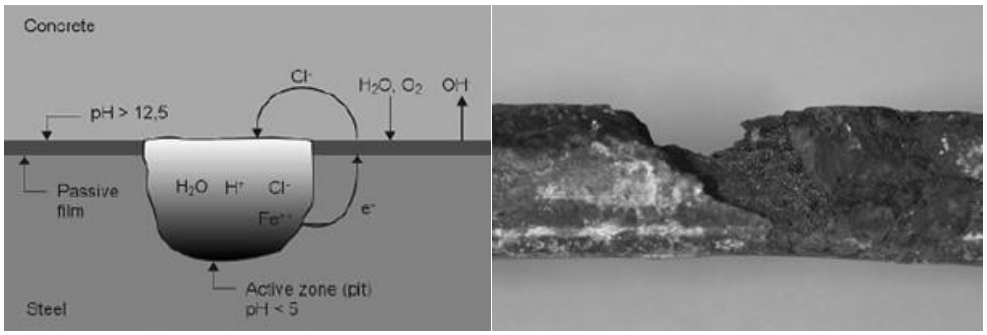

Figure 6: Schematic representation of pitting corrosion of steel in concrete and an example of localized corrosion attack in a steel bar [35].

To offer some protection against this process, steel in concrete structure is usually coated with an anti-corrosion layer and this can be destroyed when exposed to chlorides and a pH reduction of concrete pore solution, due to the reaction of concrete salts with CO_2 from the atmosphere [38].

1.2.3. Existent Corrosion Inhibitors

Being corrosion, the major threat to concrete's longevity, throughout the years, attempts to revert this problem have been made. In the late 50's, studies were developed regarding the inclusion of nitrite in concrete structures as a corrosion inhibitor. In the late 70's, it was started to be applied. It seems that it might be something already widely applied. More recently, M. Ormellese et al. tested about 80 organic substances, since amines, amino acids, mono- and poly-carboxylates, with the intention of analysing the effect of functional groups (amine or carboxyl), the position and number of the substituents and the influence of electron-donor or electron-attractor groups in the inhibition effect of corrosion. They concluded that amines and alkanolamines have no influence in the solubility and properties of both fresh and hardened concrete. Organic carboxylate substrates showed to have a very good inhibitive effectiveness [38].

One of the most common ways to protect metallic substrates from corrosion was the application of chromium based materials. Nevertheless, due to chromium (VI) high toxicity, its use was forbidden and the search for an environmentally friendly solution became mandatory [33].

There are several self-healing corrosion processes, being one of them the incorporation of nanocontainers filled with corrosion inhibitors. Some research has already been made regarding the

corrosion protection of metallic surfaces. Hang et al. treated a montmorillonite clay with an organic compound (aminotrimethylphosphoric acid (ATMP)) and dispersed in an epoxy resin to improve corrosion protection of carbon steel. It was revealed that this process had significant results due to improvement of barrier properties of the coating [39]. Hayatdavoudi et al. used an inhibitor-intercalated layered double hydroxide nanocontainers dispersed in zinc-rich epoxy coating, as an anti-corrosive solution for carbon steel substrate. They found that the addition of LDH nanocontainers into the resin provided a superior corrosion protection, due to the combination of barrier effect, sacrificial cathodic protection and smart inhibition action [40].

Calcium sulphoaluminate (CSA) cements which contains dicalcium silicate and calcium aluminates, are produced from gypsum, bauxite and limestone at 1300 ºC. Being CO_2 one of the most abundant pollutants, concrete's corrosion caused by carbonation easily prevails. Haining et al. tested that when LDHs are included into concretes mixtures, the carbonation resistance increases and the depth of the carbonation process is lower [41].

1.2.3.1. Corrosion Inhibitors involving LDHs

LDHs have been studied with great interest for application as protective coatings or incorporated inhibitor in reinforced concrete, for example. One of the application of LDH is as a corrosion preventive additive in concrete and it has been studied vastly in the past 10 years [36].

The use of layered double hydroxides in corrosion prevention solutions has been studied, being largely used as coating additives. Due to LDHs anionic exchange capability, the inhibitors are released and aggressive species can be entrapped into the interlayer galleries [4]. Zhang et al. investigated the variety of properties that LDHs offer, evermore, their ability to modify the properties of the coatings by varying the layer composition and the intercalation of other anions [42]. Li et al. focused their investigation in the preparation and characterization of Mg-Al LDH intercalated with tungstate anions by co-precipitation method, which was used as a new corrosion inhibitor with environmentally friendly properties in epoxy resin for anticorrosion of Mg alloys [43]. A silica-zirconia based hybrid film was prepared as an anticorrosion coating deposited on 2024 aluminium and it showed an effective self-healing capacity on the damaged areas [44]. Hayatdavoudi et al. used intercalated LDH nanocontainers with inhibitors to disperse into a zinc-rich epoxy coating, with the purpose of entrap chloride anions and release inhibitor species to protect carbon steel [39]. With few examples, it was observed the great interest of explore LDH utility in corrosion protection. Therefore, after observing the intrinsic potential of LDHs, these could be a very interesting solution to prevent corrosion of carbon steel in reinforced concrete.

1.3. Thesis goal

The main goal of this master thesis was to investigate solutions to increase the lifetime of concrete when exposed to extreme environmental conditions, using LDH-based materials as corrosion inhibitor carriers and traps for the aggressive species. To achieve this goal three different materials were prepared: ZnAl-NO_2 LDH by co-precipitation, and ZnAl-citrate and ZnAl-tartrate LDH by intercalation using ZnAl-NO_3 LDH as precursor. The synthesized materials were all characterized using the following techniques: X-ray Diffraction (X-RD), Fourier transform infrared spectroscopy (FT-IR), Scanning electron microscopy (SEM)/ Transmission electron microscopy (TEM), Dynamic light scattering (DLS), Zeta Potential, Thermogravimetric analysis (TGA) and Inductively coupled plasma spectroscopy (ICP). Mesoporous silica-coated LDH nanoparticles were prepared, using the LDH base (LDH-NO_3) and one intercalated with inhibitor (LDH-citrate). The interest was to analyse how this coating layer could affect the corrosion inhibitor release kinetics.

Release studies and electrochemical impedance spectroscopy (EIS) experiments in solution were performed for further parallel interpretation between the reference solution (NaCl) and the suspensions with the prepared materials: LDH-NO_3, LDH-NO_2, LDH-citrate and LDH-tartrate.

2. Experimental Procedures

2.1. Materials

For the synthesis of LDHs by co-precipitation (ZnAl-NO_3 and ZnAl-NO_2 LDH), the following reactants were used: sodium hydroxide (NaOH, 99,0%, Merck-Germany), sodium nitrite ($NaNO_2$, 98%, Alfa Aesar), sodium nitrate ($NaNO_3$, 99%, VWR Chemicals –PROLABO), zinc nitrate hexahydrate ($Zn(NO_3)_2.6H_2O$, 98%, Sigma Aldrich) and aluminium nitrate nonahydrate ($Al(NO_3)_3.9H_2O$, 98%, Sigma Aldrich).

Intercalation of selected corrosion inhibitors was pursued using two reactants: tri-sodium citrate dihydrate ($C_6H_5Na_3O_7.2H_2O$, 99.9%, VWR chemicals – PROLABO) and tartaric acid ($C_4H_6O_6$, 99%, F.Mesquita Araújo).

For LDH functionalization with mesoporous silica the following reactants were used: ammonia solution (NH_4OH, 25%, Panreac), cetyltrimethylammonium bromide (CTAB, 99%, Sigma Aldrich) and tetraethyl orthosilicate (TEOS, >99.0%, Sigma Aldrich).

All chemicals were used without further purification.

2.2. Synthesis of LDHs

In the first synthesis, ZnAl-NO_3-LDH (base material) was prepared by co-precipitation method, following a similar procedure used by Poznyak [33].

The following solutions were prepared: 200 mL of sodium hydroxide solution with a molarity of 3 M, 400 mL of $NaNO_3$ solution with a concentration of 1.5 M and 200 mL of metallic nitrates, $Zn(NO_3)_2.6H_2O$ and $Al(NO_3)_3.9H_2O$ with molarities of 0.75 M and 0.38 M, respectively (ratio 2:1). To avoid contamination with carbonate ions, all solutions were prepared with deionized water and before moving on to the synthesis, the three solutions were exposed to nitrogen bubbling for 15 minutes.

The synthesis of LDH-NO_3 and LDH-NO_2 were performed the same way, changing only the 1.5 M $NaNO_3$ solution for 1.5 M $NaNO_2$ solution. The reaction occurred by co-precipitation, which means that the metallic nitrates and sodium hydroxide solutions were added simultaneously to the sodium nitrate/nitrite solution. Addition was carried out at room temperature, under continuous nitrogen flow, vigorous agitation and controlled pH (9-10). In the end, pH was set around 10.

Since the mixture became more viscous with reaction time, the magnetic stirring was increased from 300 rpm to 350/400 rpm. The reaction terminated when the metallic nitrates was completely depleted (limiting reactants).

Afterwards, the suspension was heated for 4 h at 100 ºC with vigorous stirring, and then let to cool at room temperature. After removing the supernatant fluid, the cake-like material was washed with deionized water, until ionic conductivity reached ≤ 1 mS/cm^2. The ionic conductivity was measured as a control parameter of little contamination by starting materials. Finally, the slurry was filtered under vacuum and collected as a slurry.

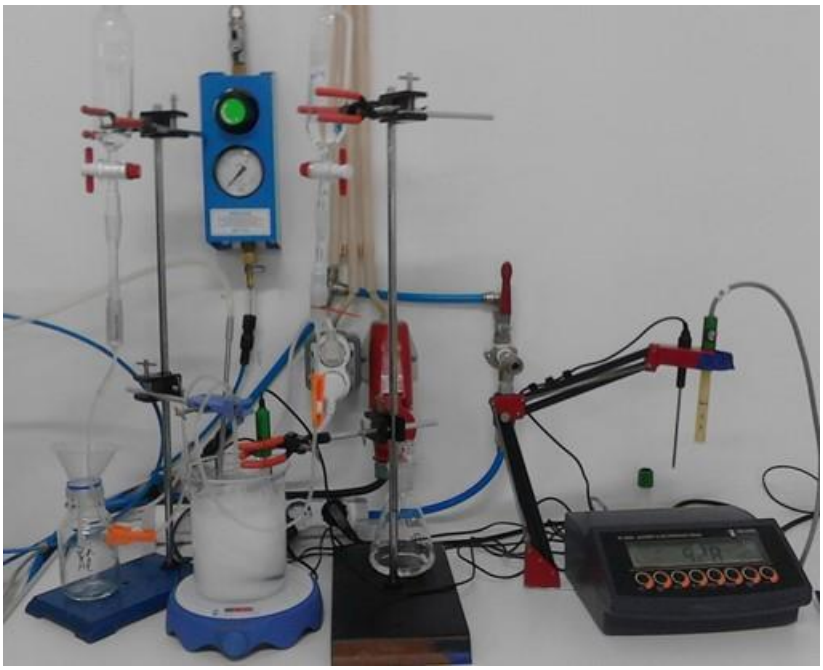

Figure 7: Experimental installation for the LDH synthesis.

2.3. Intercalation of LDHs with corrosion inhibitors

Since the main goal of this work is to study the impact of the use of corrosion inhibitors into concrete, the previously prepared LDH-NO_3 was further intercalated with tartrate and citrate anions.

In a beaker, 250 mL of 0.1 M sodium tartrate solution, obtained by neutralization of tartaric acid with NaOH, was added to 80 g of LDH-NO_3 suspension. In the case of intercalation with citrate anion, 250 mL of 0.1 M tri-sodium citrate dihydrate solution was prepared.

Intercalations lasted 24h under vigorous agitation, at room temperature.

Then, the mixtures were washed with deionized water and filtered under vacuum. The intercalated LDHs were totally dried overnight in an oven at 60 ºC and manually grinded to a fine powder.

2.4. Encapsulation/LDH functionalization with silica

The nanoparticles LDH-NO_3@mSiO_2 and LDH-citrate@mSiO_2 were synthesized following the encapsulation procedure described by Harrison et al [45].

2.4.1. Preparation of LDH-NO_3@mSiO_2 nanoparticles

To 10 mL of a 0.4 wt% LDH-NO_3 suspension was added NH_3H_2O (0.3 mL, 25 %) and the temperature raised to 50 ºC. 0.25 g of CTAB was then added to the heated suspension and stirred for 15 minutes, followed by TEOS (0.3 mL) dropwise addition under vigorous agitation (~ 300 rpm) and let to age during 4 hours. The reaction mixture was centrifuged (4700 rpm, 12 min), washed twice with deionized water and dried in the incubator overnight at 50/60 ºC.

To remove the surfactant, dried LDH-NO_3@mSiO_2 (6 mg) was placed in a roundbottom flask and refluxed with 15 mL of ethanol during 8 hours. Then, the mixture was centrifuged and washed several times with ethanol and dried overnight at 50-60 ºC.

Since the quantity of particles obtained was very low (~ 6 mg), the preparation of LDH-NO_3@mSiO_2 nanoparticles was repeated using ten times the quantities of reactants and replacing the aqueous environment for ethanol to avoid TEOS hydrolysis.

2.4.2. Preparation of LDH-citrate@mSiO_2 nanoparticles

LDH-citrate@mSiO_2 nanoparticles were prepared using the same method described above, using a 0.4 % LDH-citrate suspension.

2.5. Release studies

For the release studies, each LDH material loaded with corrosion inhibitors was tested in 3 different conditions of salinity ([NaCl]=5, 50 and 500 mM), as shown in Table 1. In a typical experiment 40 mL of sodium chloride solution was added to 200 mg of powdered LDH and agitated for one month. Aliquots were collected at distinct times (1 h, 2 h, 3 h, 6 h, 24 h, 48 h, 72 h, 1 week, 2 weeks and 4

weeks) and numbered. These samples were analysed in triplicate using high performance liquid chromatography (HPLC) to monitor the inhibitor concentration over time.

2.6. High-performance liquid chromatography (HPLC)

Liquid chromatography is an analytical technique used to separate components of a mixture based on their affinity with the mobile/stationary phases. There are three different types of stationary phases: thin layer chromatography (TLC), paper chromatography (PC) and liquid column chromatography (LC). HPLC is the LC technique with the highest efficiency, which means that it separates different sample compounds of distinct retention times with a given resolution. The selectivity of this technique is dependent of the stationary and mobile phase [46]. The equipment used was a ThermoScientific Ultimate 3000 (Figure 8), under the following conditions: $1x10^{-6}$ M sulfuric acid as eluent; isocratic column, C18 Waters Spherisorb S10 ODS2; T=40ºC; UV detector with λ=210 nm; injection volume=20 μL and flow rate=1.0 mL/min. Before analysing the collected samples, calibration curves obtained with nitrite, citrate and tartrate standard solutions were traced, achieving square correlation coefficients higher than 0.98 (Appendix A).

Table 1: Different conditions of release studies for each LDH material loaded with inhibitor.

System	Condition
LDH-NO_2	5 mM NaCl
	50 mM NaCl
	500 mM NaCl
LDH-citrate	5 mM NaCl
	50 mM NaCl
	500 mM NaCl
LDH-tartrate	5 mM NaCl
	50 mM NaCl
	500 mM NaCl

Figure 8: ThermoScientific Ultimate 3000 HPLC system used in this work.

2.7. Electrochemical impedance spectroscopy (EIS) studies

This technique is normally used to evaluate the efficiency of coating permeability or barrier capacities against corrosion of metallic structures. This allows to determine an inhibitor performance and to quantify kinetic information on coating and/or substrate deterioration [47].

In order to assess the performance of the prepared materials, suspensions of 50 mg powdered LDH-NO_3 and LDH-inhibitors in 10 mL of NaCl solutions with different concentrations and pH=13 were prepared and placed in individual tubes in contact with a carbon steel board. The alkaline pH was chosen to simulate the characteristic basicity of concrete.

The carbon steel board was, firstly, sanded, washed with detergent, dried with ethanol and saved wrapped in tissue paper to avoid the contact with air. Methacrylate tubes were juxtaposed in the carbon steel board and the outside edges were coated with epoxy-resin for isolation, so the solution was not in touch with the resin. These tubes were filled with the suspensions prepared before. EIS measurements were carried out on a bare carbon steel board at room temperature using a three-electrode cell consisting of a saturated calomel reference electrode, a platinum foil counter electrode and a carbon steel plate as the working electrode in the horizontal position, as shown in Figure 9 (right).

The cell was placed in a Faraday cage (Figure 9, left) to avoid external electromagnetic interferences. Measurements were made after 1 h, 2 h, 24 h, 48 h, 72 h, 1 week, 2 weeks and 4 weeks of contact.

The impedance values acquired for the samples were compared to the data obtained for the reference solutions, which corresponds to the native NaCl solutions at 5, 50 and 500 mM without any additive. The measurements were performed using a Gamry 600 potentiostat/galvanostat/ZRA. The typical frequency range chosen was from 1×10^{5} to 1×10^{-2} Hz, with a 10 mV RMS sinusoidal perturbation vs. open circuit potential. The software used for data analysis was Gamry Echem Analyst 5.1.

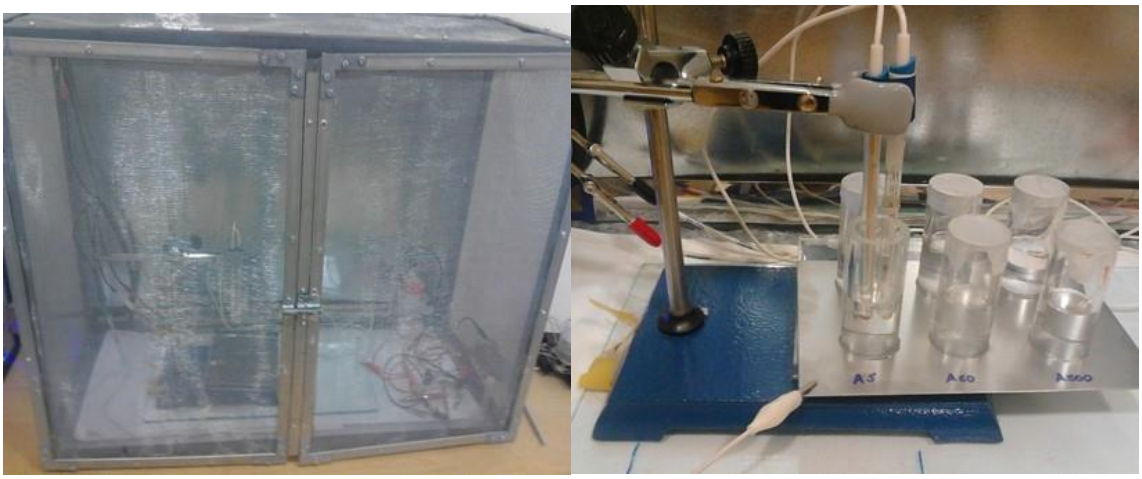

Figure 9: Faraday cage (left) and experimental installation (right).

2.8. Characterization techniques

LDH-NO_3, LDH-NO_2 and the intercalated LDHs, LDH-citrate and LDH-tartrate were characterized using the techniques described below. Functionalized samples with silica were analysed only by FTIR spectroscopy and SEM, to verify the presence of silica and the morphology of the modified materials.

2.8.1. X-Ray diffraction (X-RD)

X-ray diffraction is one of the most commonly used techniques for the study of crystal structures and atomic spacing. The X-ray diffraction is based on the constructive interference of monochromatic x-rays and a crystalline sample. A cathode ray tube generates the x-rays by heating a filament to produce electrons. These electrons are accelerated due to applied voltage, the target material is bombarded with electrons and a characteristic X-ray spectra is produced.

When conditions are satisfying to Bragg's Law, constructive interference and a diffracted ray are produced, due to the interaction between the incident rays and samples. Bragg's Law connects the wave-length of electromagnetic radiation to the diffraction angle (θ) and the lattice spacing (d) in a crystalline sample. The diffracted x-rays are detected, processed and counted. Below in Equation 3 is presented Bragg's law [48].

$$2d\sin\theta = n\lambda \quad \text{Eq.3}$$

This technique was used as a quality parameter of the prepared LDHs. The identification of LDH characteristic reflections angles, was used to verify the success of the co-precipitation and intercalation procedures. For this work, X-RD data were collected in a X'PERT-MPD Philips diffractometer working with a CuKα1 radiation (λ= 0.154056 nm), from 5 to 80º with a stepped size of 0.02º.

The X-ray diffractograms allowed the determination of the lattice parameters *a* and *c*, basal spacing (BS), gallery height and crystallite size. At low angles, the X-ray patterns presented two principal reflections for LDHs: (*003*) and (*006*). The reflection (*003*) gives the information to calculate one of the lattice parameters, *c*, and the basal spacing (BS). The basal spacing or layer stacking, *d*, which is the equivalent to the thickness of a brucite-like layer plus the gallery height or interlayer spacing. The value considered for the thickness of brucite-like layers was 0.48 nm [49].

$$c = 3d_{003} \quad \text{Eq.4}$$

$$BS = d_{003} = \frac{c}{3} \quad \text{Eq.5}$$

$$BS = gallery\ height + (thickness\ of\ a\ brucite - like\ layer) \quad \text{Eq.6}$$

Having the gallery height and ions size, it can be inferred the probable orientation of the ions within the layers. At angles near 60º, for CuKα radiation, the (*110*) reflection allowed to calculate the lattice parameter, *a*, which corresponds to the inter-cation distance within the hydroxide layers, suggesting a constant inter-metallic distance [50],[51].

$$a = 2d_{110} \quad \text{Eq.7}$$

The intermediate angles have correspondent (01*l*) and/or (10*l*) reflections, which can help to determine the stacking sequence of hydroxide layers.

Appealing to Scherrer equation, it was determined the crystallite size:

$$L = \frac{K \times \lambda}{FWHM \times cos\theta} \quad \text{Eq.8}$$

Where L=crystallite size (nm); λ=X-ray wavelength (cm^{-1}); FWHM= Full width at half maximum (radians); θ= angular peak position (radians); K= Scherrer constant (0.94, if used FWHM).

2.8.2. Dynamic light scattering (DLS) e Zeta Potential

The dynamic light scattering (DLS) technique is a method currently used to measure the hydrodynamic size distribution of particles typically in the submicron region, that can be related to the distribution of the real sizes of particles [49],[53]. At a fixed angle, the instrument can determine a mean particle size in a limited size range. Instruments that have multiangles can determine the full

particle size distribution [54]. The particles are suspended in a liquid with Brownian motion. The larger the particle, the slower the Brownian motion will be. The Brownian motion is monitored with light scattering. To characterize a dispersion, the average particle size and particle size distribution are important parameters. In DLS, large particles scatter the light much more intensely that smaller particles, which causes the production of artefacts [55].

It also measures the zeta potential of a particle and measures/estimates the molecular weight of organic compounds.

Figure 10: Zeta potential cell - equipment Zetasizer Nano-ZS.

An ionic solution has an intrinsic charge. Zeta potential is an electrokinetic potential in colloidal dispersions, which means that this parameter indicates the stability of the dispersions. Zeta potential reflects the potential difference between the electric double layer of the mobile particles and the layer of dispersant phase around them. It is used to determinate if the particle within the liquid will flocculate or not. The colloid stability is given by ranges of values: ± 0-10 mV: highly unstable; ± 10-20 mV: relatively stable; ± 20-30 mV: moderately stable; >± 30 mV: highly stable [53]. The equipment used was a Zetasizer Nano-ZS under the following conditions: T=25ºC, with a variable count rate and a measurement angle of 173º. The analysed solutions were prepared, suspending a small amount of LDH slurry in deionized water until it acquires a slightly white aspect.

2.8.3. Inductively coupled plasma- Atomic emission spectroscopy (ICP-AES)

This analysis is used to identify and measure almost every element in the spectrum necessary for the analysis of metal samples [56]. Technique that can determine elemental concentrations from trace to major while detecting most elements in the periodic table. The ICP-AES spectrometer detects the atomic emissions produced as light.

This technique was used to confirm the metallic ratio zinc/aluminium in LDHs layers. The equipment used for the determination was ICP-OES Jobin Yvon Activa.

2.8.4. Thermogravimetric analysis (TGA)

This technique is used to investigate the thermal characteristics of substances.

When a thermogravimetric analysis is performed, the sample is heated under nitrogen or synthetic air with a programmed heat rate, while the mass difference during this process is measured. A mass loss implicates that a degradation of the analysed substance takes place. The reaction with oxygen from the synthetic gas can lead to an increase of mass [46]. This technique was used to determine the temperatures to which the most drastic mass losses occur. Thermogravimetric analysis was performed under an air atmosphere using a Shimadzu TGA-50 thermogravimetric analyser. Curves were recorded at a rate of 10 ºC/min with a temperature range of 20-800 ºC.

2.8.5. Fourier-transform infrared (FT-IR) spectroscopy

When a sample is exposed to IR radiation, some of it is absorbed by the sample and some passes through. The resultant signal of the detector is a characteristic spectrum of the sample, which are created due to the conversion of the Fourier transform output into a spectrum. Each molecule produces a spectrum.

FT-IR spectroscopy helps the identification of chemical bonds in a molecule by producing an infrared absorption spectrum and it is an effective analytical technique that can be used to detect functional groups and characterizing covalent bonding information [46]. FT-IR spectra were collected in a Perkin Elmer FT-IR spectrometer Spectrum Two with a UATR TWO unit (Diamond), 64 scans, 4 cm^{-1} resolution, in a wavelength range of 400-4000 cm^{-1}. Resorting to attenuated total reflectance (ATR), the samples were used as powder and they were recoverable.

2.8.6. Scanning electron microscopy/ transmission electron microscopy (SEM/TEM)

Scanning electron microscopy and transmission electron microscopy are techniques vastly used for examination and analysis of the microstructure morphology and chemical composition. The beam used in TEM is a broad static beam, intense enough to pass through the sample, while in SEM, the beam is focused in a fine point and the sample surface is scanned line by line. The voltage used is lower than needed for TEM because the goal is not penetrating the specimen [57]. The beam in contact with the sample produces several signals. The obtained image depends on the produced signals from the electron beam and specimen interaction [58].

The scanning transmission electron microscopy (STEM) coupled with energy dispersive spectroscopy (EDS) was performed in a Hitachi SU-70 system with electron beam energy up to

30 keV. For the microscopy analysis, suspensions of LDHs with ethanol were prepared and carbon grids were submersed and dried at room temperature.

3. Results and Discussion

In this work, ZnAl (2:1) layered double hydroxides were prepared as described in section 2, with four different anions intercalated: nitrate, nitrite, citrate and tartrate. After drying the slurries, they presented a stiff texture and white coloration. The materials were manually grinded, resulting in a fine and white powder. All materials were characterized by X-RD, DLS and Zeta Potential measurements, ICP, TGA, FT-IR spectroscopy and SEM/TEM, in order to determine their main properties. The following step was the verification of the LDH materials performance in solution by release studies, monitored by HPLC and corrosion protection assays by EIS. These techniques were used to quantify the amount of corrosion inhibitor released over a month and allowed to evaluate the degradation of the carbon steel and the protective influence regarding the presence of corrosion inhibitor in solution.

3.1. Characterization

- **X-RD**

X-ray diffraction analysis of the synthesized materials allowed the identification of the principal phases present in the particles, therefore being used as a quality control tool for the success of the synthesis. The reflections patterns in X-RD diffractograms can provide information of the stacking of the layers and the arrangement of the hydroxyl group of adjacent layers [59]. Resourcing to the diffraction reflection (*006*) and the correspondent full width at half-maximum (FWHM) values, it was possible to estimate the average crystallite size for each particle, which corresponds to a single crystal in powder form, however in one particle size can be present more than one single crystal [4]. Typically, the polytype observed in LDH is a 3-layer polytype with a rhombohedral symmetry and the OH groups forming a trigonal prismatic environment. The X-RD patterns of the LDH-NO_3 and LDH intercalated with the corrosion inhibitors (nitrite, citrate and tartrate) are shown in Fig.11, 12, 13 and 14, respectively. The inhibitors X-ray patterns were compared with the base material, LDH-NO_3. In Table 2, are presented for each material analysed, the lattice parameters (*a* and *c*), basal spacing, gallery height and crystallite size, determined using the Equations 4, 5, 6, 7 and 8 (Experimental section).

Table 2: Lattice parameters, basal spacing, gallery height and crystallite size for LDH-NO_3, LDH-NO_2, LDH-citrate and LDH-tartrate.

	$a=2d_{110}$ (nm)	$c=3d_{003}$ (nm)	BS=c/3 (nm)	Gallery height (nm)	Crystallite size (nm)
LDH-NO_3	0.306	2.64	0.881	0.401	18.8
LDH-NO_2	0.308	2.34	0.781	0.301	11.3
LDH-citrate	0.303	3.58	1.19	0.713	14.2
LDH-tartrate	0.305	3.59	1.20	0.716	21.6

Figure 11 depicts the X-ray spectra of LDH-NO_3, which was the base material used for the intercalation with two of the inhibitors: citrate and tartrate. At low angles, there are two strong reflections (*003*) and (*006*) present in all spectra. According to Mahjoubi et al., the unit cell parameters and basal spacing, for ZnAl-NO_3-LDH are *a*=0.306 nm, *c*=2.653 nm and BS=0.884 nm, respectively [60]. In this work, for ZnAl-NO_3-LDH, the estimated parameters were *a*=0.306 nm, *c*=2.64 nm and BS=0.881 nm. Comparing with the previous work about ZnAl-NO_3-LDH, the obtained results were consistent.

Given 0.48 nm as the thickness of the brucite-like layer [49], the gallery height determined was 0.40 nm using Eq.6 (Experimental section). Resourcing to Tezuka et al., the ionic size of nitrate ion is 0.33 nm, therefore, relating the ion size and the gallery height, it was possible to infer that the ions were rearranged vertically [61]. In the X-RD pattern, angles comprised between 31.8º - 63º range may include reflections that correspond to ZnO contaminations, namely the (**100*), (**002*), (**101*) and (**110*) reflections.

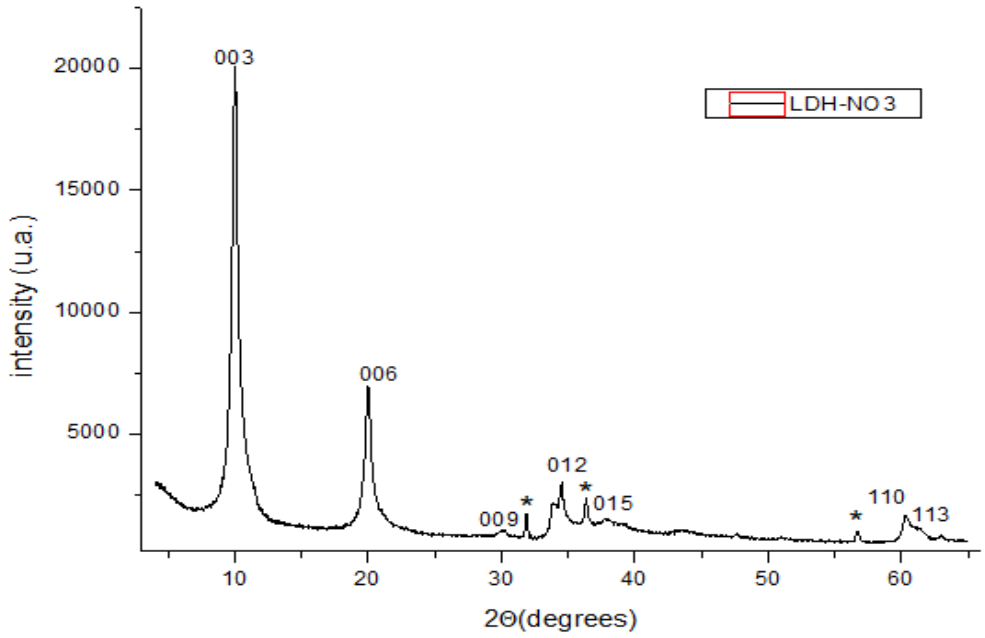

Figure 11: X-RD pattern of ZnAl-NO_3-LDH, where the peaks with * correspond to ZnO contaminations (reflection **100*, **101* and **110* with corresponding angles 31.88º, 36.37º and 56.69º).

According to Xu et al., when comparing the basal spacing of MgAl-LDH-NO_3 and MgAl-LDH-NO_2, it revealed a decreased in the value [62]. Extrapolating to the LDHs prepared in this work, with metallic ions used being Zn and Al, the same shift occurred (Figure 12). The basal spacing of ZnAl-NO_2-LDH was 0.781 nm with a corresponding gallery height of 0.301 nm. Since nitrite ion size was not found, it was analysed its geometry comparing it to nitrate ion geometry. Nitrate ion is apolar and has a triangular geometry, whereas nitrite ion has polarity due to the electron free pair of nitrogen and its geometry is triangular "V"-like. Comparing both geometries, it can be inferred that nitrite is smaller in height and possibly broader in width. Therefore, since nitrate ion size is 0.33 nm, nitrite ion size will probably be smaller. So, it is possible that the ion's size is shorter than the gallery height (0.301 nm) and the arrangement of the ions might be vertical.

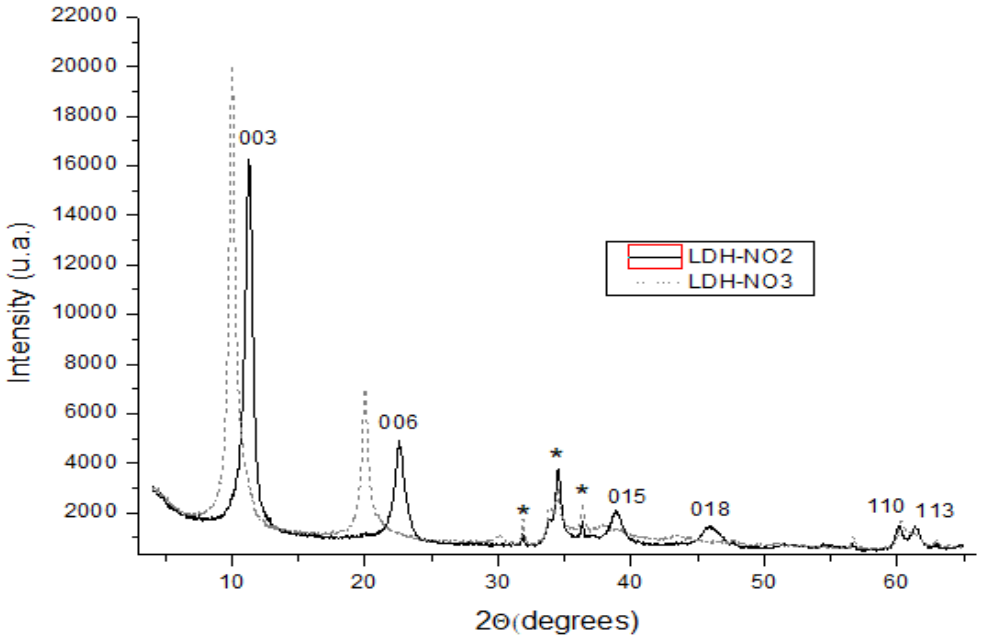

Figure 12: X-RD pattern of ZnAl-NO_2-LDH (black) and ZnAl-NO_3-LDH (grey dots), where the peak with * correspond to ZnO contaminations (reflections *_100_, *_002_ and *_101_ with corresponding angles 31.87º, 34.53º and 36.31º).

In Figures 13 and 14, comparing the (*003*) and (*006*) reflections of LDH-citrate and LDH-tartrate with LDH-NO_3 spectra, the angles corresponding to those reflections are shifted to lower values. The probable reason for this shifting of the basal peaks in citrate and tartrate LDHs X-RD patterns to a lower wave number is an increase of the interlayer spacing after intercalation with citrate and tartrate anions.

Using equation 5 and 6 (Experimental section), the basal spacing obtained for LDH-citrate was 1.19 nm and the gallery height calculated was 0.713 nm. Considering the size of citrate ion as 0.72 nm,

the gallery height suggests a vertical rearrangement of the ions within the layers, with a slight angle [51].

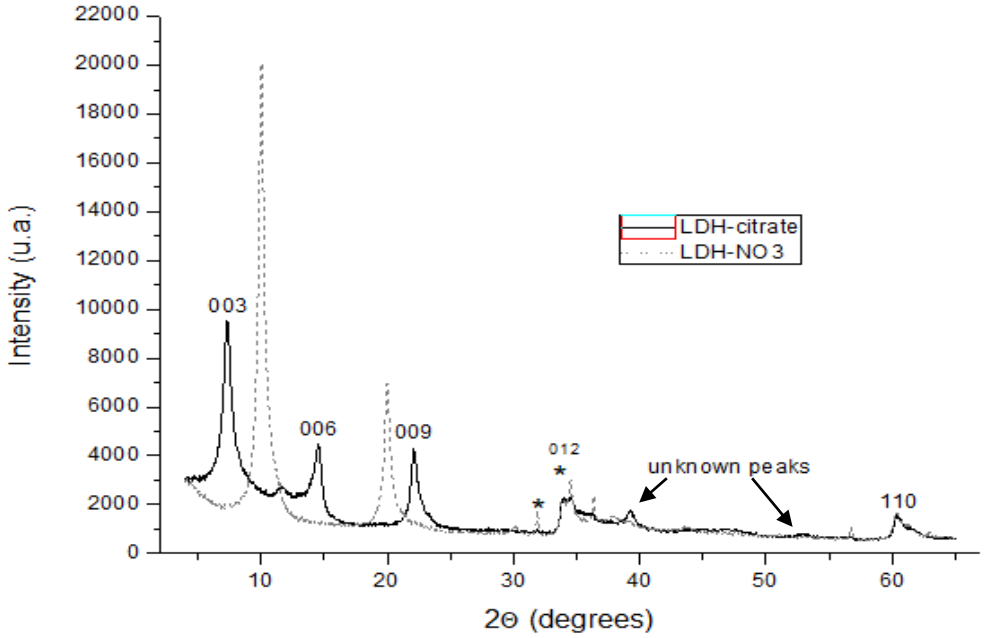

Figure 13: X-RD pattern of intercalated ZnAl-citrate-LDH (black) and ZnAl-NO_3-LDH (grey dots), where the peak with * correspond to ZnO contamination (reflection ****100* **and ****002*** **with corresponding angles 31.85º and 34.47º) and the remaining non-identified correspond to unknown peaks.**

For LDH-tartrate, the estimated basal spacing was 1.20 nm and the correspondent gallery height 0.72 nm. Being the size of the tartrate anion in an anti-conformation 0.477 nm, this indicates that its orientation is vertical [63].

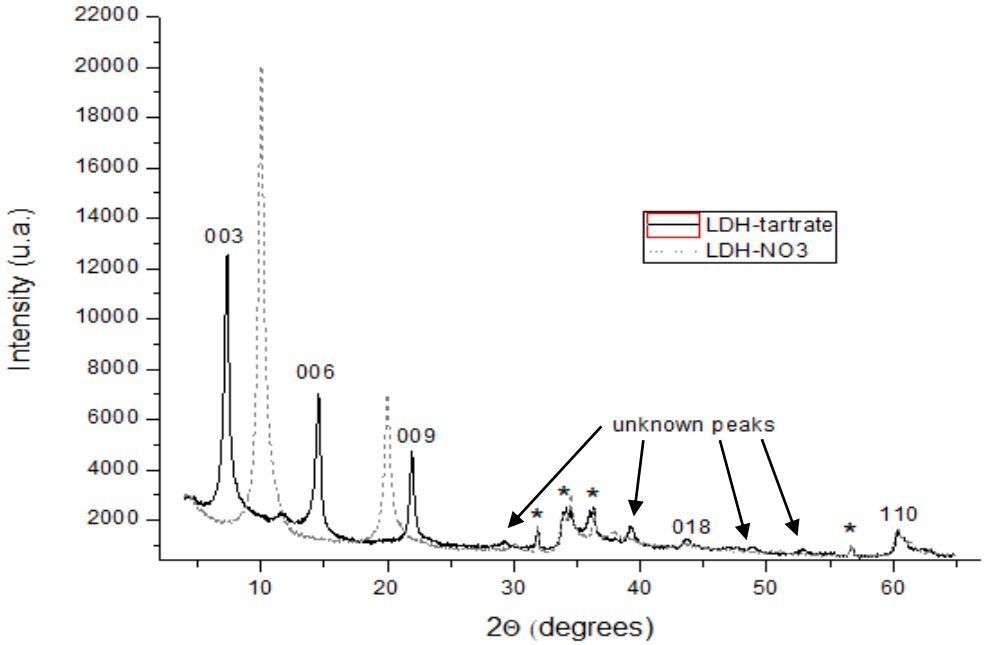

Figure 14: X-RD patterns of intercalated ZnAl-tartrate-LDH (black) and ZnAl-NO_3-LDH (grey dots), where the peaks with * correspond to ZnO contaminations (reflections **100, *002, *101* and **110* with corresponding angles 31.85º, 34.48º, 36.34º and 56.69º) and the remaining non-identified correspond to unknown peaks.

It was observable a diffraction peak around 39º only in the X-ray spectra of all inhibitors LDHs, however, it remained unknown the origin of this reflection. In LDH-citrate and LDH-tartrate, it is present a small broad peak at 53º that might correspond to a contamination of NaOH.

Layered double hydroxides are crystalline materials and the crystallinity can be related with the crystallite size calculated using X-RD. The crystallite size corresponds to the size of a single crystal and, to increase the size of the crystal, after synthesis (co-precipitation method) the particles were exposed to hydrothermal treatment. According to Galvão et al., after few hours of hydrothermal treatment, the smaller particles with higher surface energy and amorphous materials can dissolve until the saturation of the solution and the rest recrystallize, forming bigger and more stable crystals. Thus, as the time of hydrothermal treatment increases, the tendency to obtain particles with superior crystallite sizes increases as well [4]. Observing the resulting crystallite size, the value range obtained was between 11.3 and 21.6 nm. The crystallite size can be interconnected to the particle size.

- **DLS and Zeta potential**

As mentioned in the Experimental Procedures section, in sub-chapter 2.8.2., the DLS analysis gives the hydrodynamic size distribution of the particles. The estimated values range between 400 and 950 nm for all samples and the pH values of the analysed suspensions were, approximately, neutral.

Table 3: Hydrodynamic size intervals and Zeta potential of the prepared materials.

	LDH-NO_3	LDH-NO_2	LDH-citrate	LDH-tartrate
Hydrodynamic size (nm)	800-950	480-555	400-415	910-950
Zeta potential (mV)	+34.5± 0.736	+36.3 ± 1.53	-30.1 ± 1.22	-14.0 ± 0.216

According to Galvão et al., the hydrothermal treatment has a great influence in some parameters analysed and one of them is the hydrodynamic size. They concluded that during the crystal growth, there are two competing mechanisms: dissolution and recrystallization of LDHs. They found that as the duration of the hydrothermal treatment increases, the bigger is the tendency of the hydrodynamic size to raise and, consequently, the aggregation dynamics to form polycrystallite LDH particles [4]. Since DLS is sensitive to the suspension concentration, the higher values of hydrodynamic size might correspond to a more concentrated spot analysed or to a LDH longer chain.

The zeta potential values are depicted in Table 3. According to the intervals mentioned in sub-chapter 2.8.3., it was possible to attribute a level of colloidal stability to the suspensions. It was inferred that the LDH-tartrate suspension was the less stable, comparing to the other suspensions. Due to the typical LDH structure, the external layers are composed by the hydroxides and the metallic ions giving to the exposed layers a positive charge (Zn^{2+} and Al^{3+}). Since the only counter-charging species are found in the interlayer, the general charge of layered double hydroxides is positive. Therefore, the zeta potential values of LDH-NO_3 and LDH-NO_2 are consistent with the material's nature. However, when intercalation is processed, a LDH-NO_3 suspension is exposed to a solution with an excess of anionic species (citrate or tartrate), causing a formation of negatively charged layer around the positively charged one. This factor is explained by the anionic-exchange of some interlayer anions for the ones in solution and the easy complexation of the carboxylic groups with the metallic species. The higher or lower negativity of the adsorbed ions have impact in the zeta potential values measured. Citrate ion is more negatively charged compared with tartrate ion, due to its superior amount of carboxylate groups. Thence, this can be a reason for the lower zeta potential of the LDH-tartrate, depending on the quantity of ions adsorbed to the external layer.

- **SEM/TEM**

Scanning electron microscopy was used to verify the morphology (size and shape), while transmission electron microscopy gave information about the structure and crystallinity of the samples. Observing the following SEM images (Figure 15 and 16), they show the existence of lamellar material and some particles revealed to have a hexagonal shape and a size range of 2-20 µm, as expected. The substitution of anions in the LDH galleries did not promote any significant morphology modification.

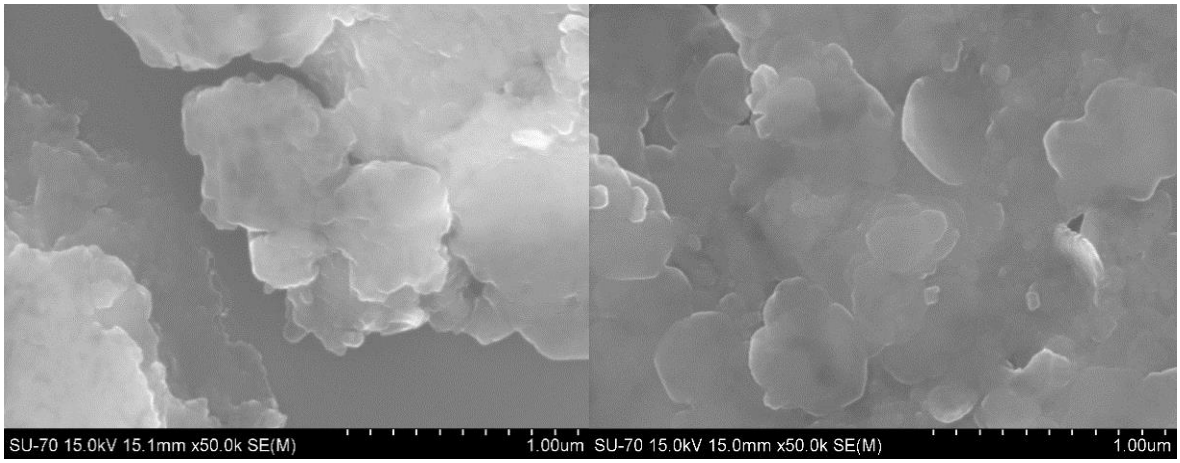

Figure 15: SEM image of LDH-NO_3 (left) and LDH-NO_2 (right).

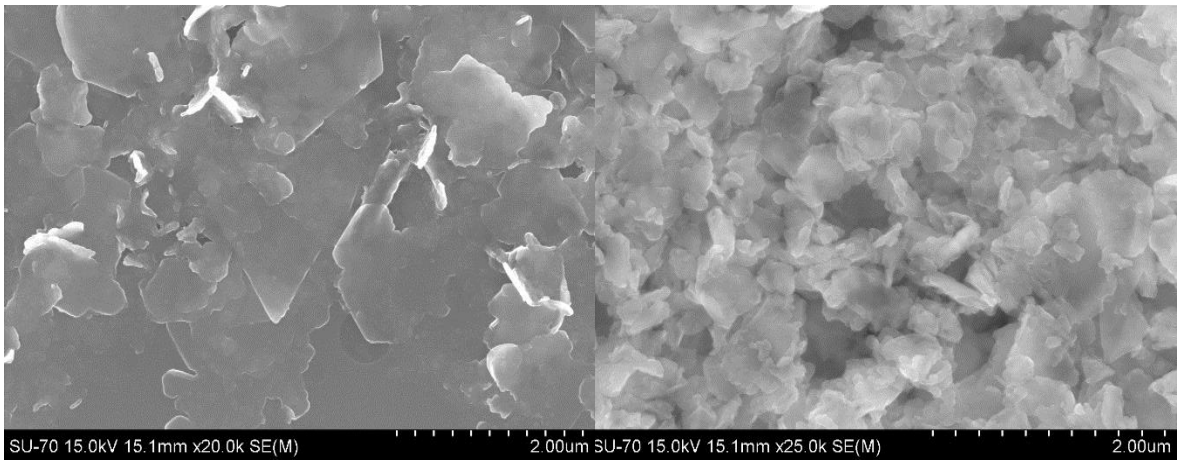

Figure 16: SEM image of LDH-citrate (left) and LDH-tartrate (right).

- **ICP**

LDHs were prepared to have a Zn/Al molar ratio of 2. In Table 4 are shown the obtained mass/molar percentages of zinc and aluminium present in each LDH prepared. Both nitrate and nitrite LDHs were synthesized from scratch with an expected Zn/Al ratio of 2. ICP testing allowed to confirm the success on the attainment of metallic ratio in the LDHs. Citrate and tartrate intercalated LDHs were prepared using the same base material (LDH-NO_3), being expectable the consistency of metallic ratio. The results exhibited in Table 4 showed coherence of Zn/Al ratio regarding to the base material and the intercalated materials – LDH-citrate and LDH-tartrate.

Table 4: Mass and molar percentages of zinc and aluminium in the LDHs and Zn/Al ratio.

	Al (% m/m)	Zn (% m/m)	Al (% mol/mol)	Zn (% mol/mol)	Zn/Al ratio
LDH-NO_3	7.2	40	0.267	0.612	2.29
LDH-NO_2	7.7	41	0.285	0.627	2.20
LDH-citrate	6.9	38	0.256	0.581	2.27
LDH-tartrate	6.7	37	0.248	0.566	2.28

- **TGA**

In the analysis of LDHs TGA profiles, the weight loss can be attributed and divided in different ranges of temperature.

At lower temperatures, mass losses are mainly due to the removal of the adsorbed surface water and the interlayer water, around 100 ºC and 250 ºC, respectively. The dehydration process begins on the surface and then continues towards the centre of particles.

However, when it comes to the following weight losses ranges, there is some uncertainty. Considering the LDH-NO_3 curve (Figure 17), it can be observed a strong drop around 200ºC and two slighter drops at 300ºC and 330ºC. According to Conterosito et al., the dehydroxylation of the layers of LDH-NO_3 would occur between 300 and 370 ºC and the principal NO loss would be located between 365 and 575 ºC [64]. Xu et al. attributed the first loss to the removal of water molecules from the interlayer space (124-135 ºC) and the second band included the collapse of the layer structure and reduction of NO_3^- anions (250-300 ºC). This band can be easily shifted to higher temperatures with the increase of the metallic ions ratio. Therefore, the interval for the intercalated nitrate anions decomposition can be between 360 and 540 ºC [65]. Raki et al. described a typical TGA/DTG curve of nitrate LDH. The first reduction corresponded to dehydration of the interlayer space up to 200ºC; the second loss, between 200 and 450ºC, was attributed to dehydroxylation of the inorganic layers and the reduction of nitrates to nitrites; above 450ºC, it can be included the condensation of hydroxyls and decomposition of nitrites [1]. Since the determination of the dehydroxilation step and the decomposition of nitrate or nitrite anions is not precise, it was decided to increase the temperature range and include both losses into the same interval (see Figure 17 and 18).

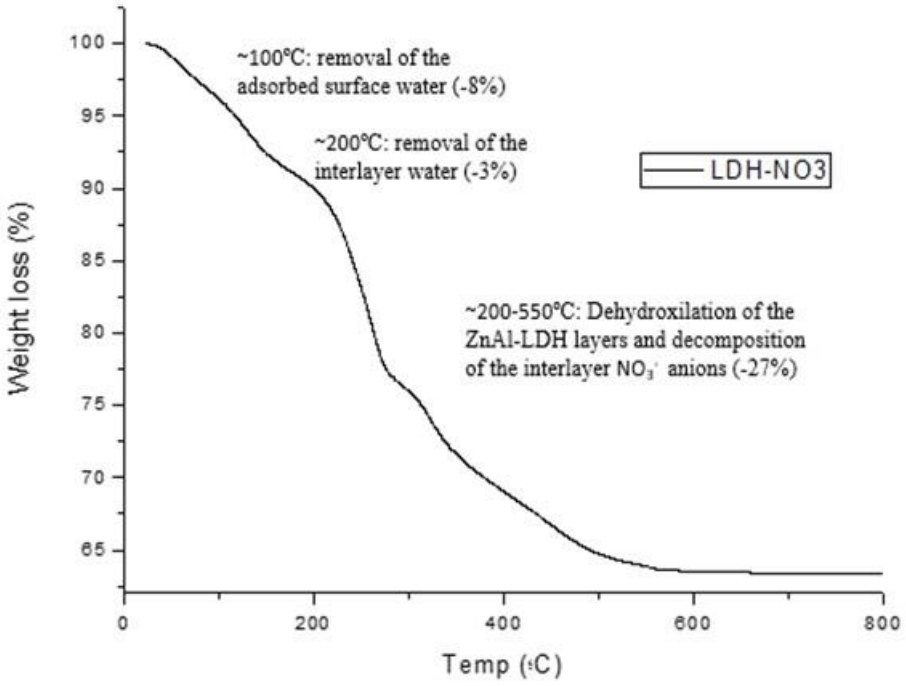

Figure 17: TGA curve of ZnAl-NO_3-LDH.

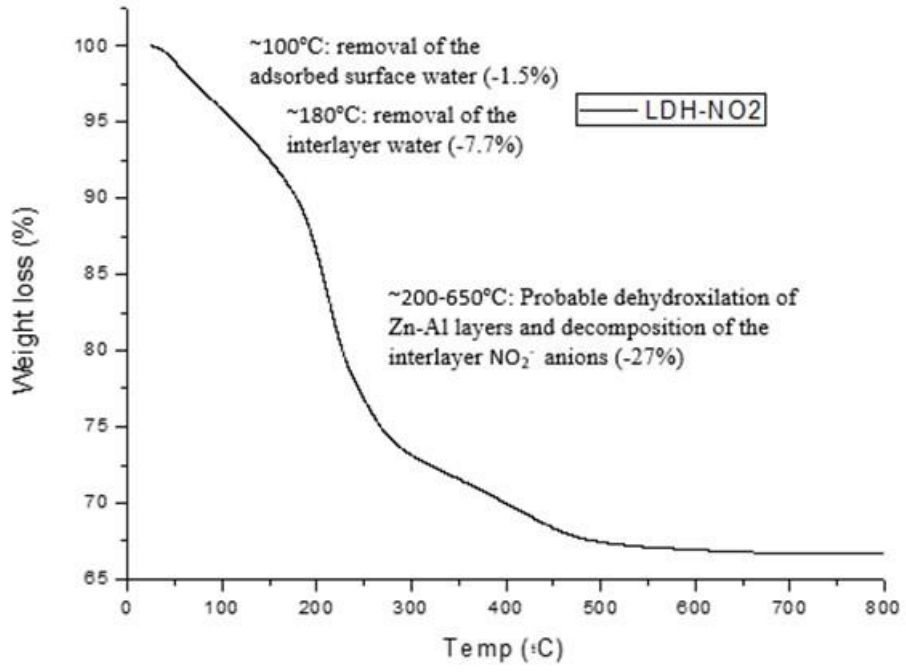

Figure 18: TGA curve of ZnAl-NO_2-LDH.

The interpretation for the TGA curve of nitrite LDH (Figure 18) is very similar to the nitrate LDH. Until 180ºC, approximately, dehydration was predominant. Although it was considered the temperature interval (200-650ºC), which includes the probable dehydroxilation of the ZnAl layers and decomposition of the interlayer NO_2^- anions, it was not easy to define to which temperature

corresponds the decomposition of nitrite anions. When considered the degradation of nitrite anions to occur only after 270ºC, the loading obtained was 10.5 % and the quantity of inhibitor released and quantified via HPLC was much higher. Therefore, considering that the decomposition starts around 240ºC and a concordant loading with the others inhibitors, it was assumed a loading of 18% for nitrite.

The most distinct mass loss in the TGA pattern of ZnAl-tartrate-LDH occurs around 400 ºC, which corresponds to the decomposition of the tartrate anions [63], as can be verified in Figure 19. The loading value read in tartrate's TGA curve was, approximately, 17%.

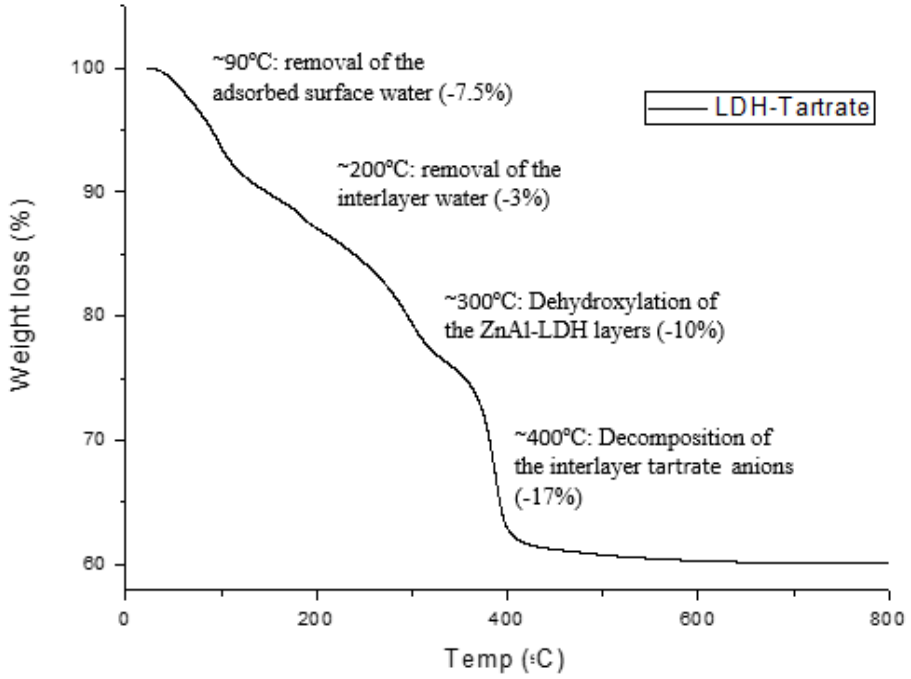

Figure 19: TGA curve of ZnAl-tartrate-LDH.

According to the tri-sodium citrate pentahydrate thermogram reported in the literature [66], the first two mass losses correspond to the dehydration process occurring between 64-88 ºC and 158-167 ºC, respectively. At higher temperatures, in this case, above 290 ºC, the sample suffers degradation. Transposing to the synthesized material in this work, the TGA curve of ZnAl-citrate-LDH showed mass losses corresponding to the dehydration between 100 ºC and 200 ºC, which are common in all LDH TGA curves. Around 375 ºC, it was observed an abrupt drop that might correspond to the degradation of the citrate anions. The difference when compared to literature values is, most likely, due to the intercalation of citrate anions into the LDH interlayer galleries, which increase their thermal resistance. Therefore, it was noticeable a 100 ºC delay between the degradation of the base material and the intercalated one. The value estimated for citrate LDH loading was, approximately, 16 %.

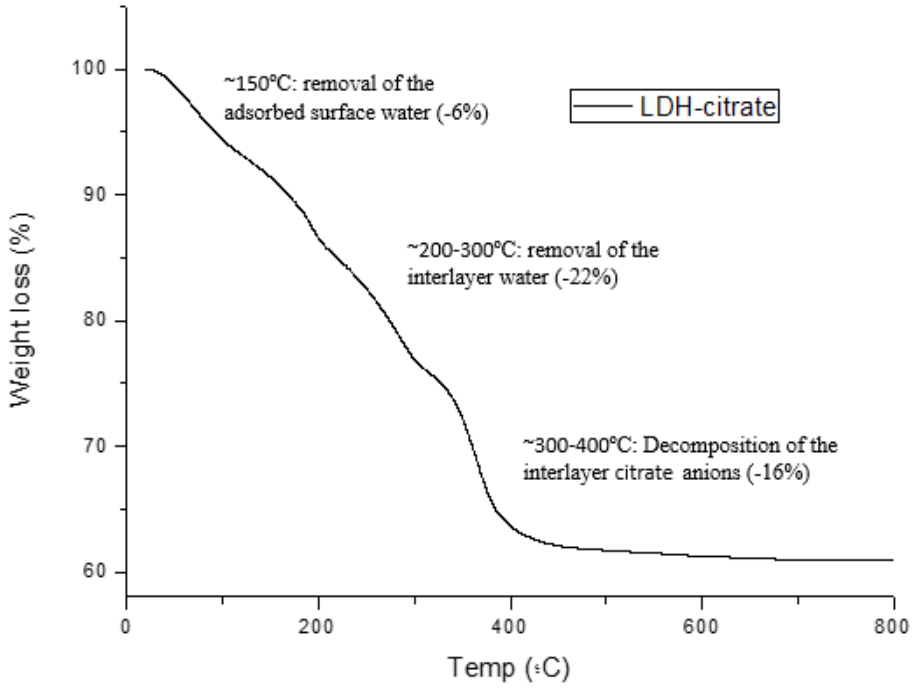

Figure 20: TGA curve of ZnAl-citrate-LDH.

- **FT-IR ATR spectroscopy**

This spectroscopic technique was used to identify functional groups in the synthetized materials. The following figures show the FT-IR spectra of the intercalated layered double hydroxides with nitrite, citrate and tartrate compared with LDH-NO_3.

Overall the bands between 1600-1200 cm^{-1} are assigned to -CO_2^- groups; 1200-1000 cm^{-1} to -C-OH; 1000-600 cm^{-1} to the metal-hydroxide group connection (-M-OH) and 600-400 cm^{-1} to the metal-oxygen connection (-M-O) [63].

The band located at 1644-1658 cm^{-1} in the FT-IR spectra of LDH-NO_3 and LDH-NO_2 is due to the deformation mode vibration of OH bonds in water molecules (δ H_2O), (Figure 21).

An intense band centred at 1346-1368 cm^{-1} corresponds to the stretching vibration of the N-O bond and stretching vibrations of nitrate group [51],[67]. Observing both spectra, LDH-NO_3 and LDH-NO_2, it was evident that in LDH-NO_2 spectra, there are two small peaks at 1360 and 1244 cm^{-1}, while in LDH-NO_3 spectra, there is an intense peak at 1346 cm^{-1}, which correspond to the bond of nitrate group. This peak is not present in LDH-NO_2 spectra.

In LDH-NO_3 spectra is observed a broad band around 3394 cm^{-1}, which corresponds to stretching vibrations of the hydroxyl groups of both, layer hydroxide moieties and interlayer water. This is one of the most dominant bands in infrared frequencies. The widening of this band can be due to the presence of water or due to strong hydrogen bond formation [16],[51]. Hydrogen bonding could be within the same molecule (intramolecular hydrogen bonding) or with neighbour molecules

(intermolecular hydrogen bonding). The peaks 1644 cm^{-1} (LDH-NO_3) and 1658 cm^{-1} (LDH-NO_2) correspond to the hydrogen bonds of water molecules. The bands that appear at wavelengths bellow 500 cm^{-1} are characteristic of metallic-oxygen (M-O) bonds.

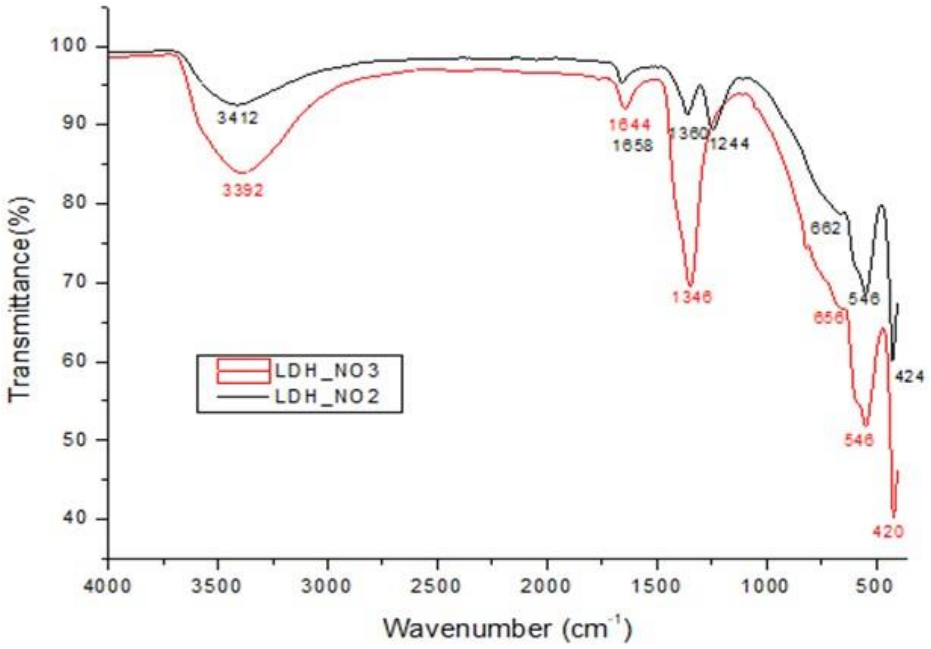

Figure 21: FT-IR spectra of ZnAl-NO_3-LDH vs ZnAl-NO_2-LDH.

The spectra of LDH-citrate (Figure 22) and LDH-tartrate (Figure 23) show the two characteristic absorption bands of the carboxylate group of the citrate anion at 1564 and 1368 cm^{-1} and the tartrate anion at 1572 cm^{-1} and 1396 cm^{-1}, which corresponds to its asymmetric and symmetric stretching modes υ_{as}(COO) and υ_{s}(COO), respectively [67].

According to Nakamoto [63], the difference $\Delta\upsilon=\upsilon_{as}-\upsilon_{a}$ gives the information about the symmetry of the interaction between the carboxylate -CO_2^- group and the hydroxylated layers.

A broad peak is observed at 3380 cm^{-1} in LDH-citrate, which corresponds to the hydroxyl, water stretching frequencies and N-O bonding. The wavenumber of this band is lower than in LDH-nitrate, which, according to Perera et al. [51], might indicate that the electron density around the functional groups has increased. Most likely, the electron density around OH groups has increased due to the presence of carboxylate and hydroxyl groups in large quantities in LDH-citrate anions, that are capable of form strong hydrogen-bonding network [51].

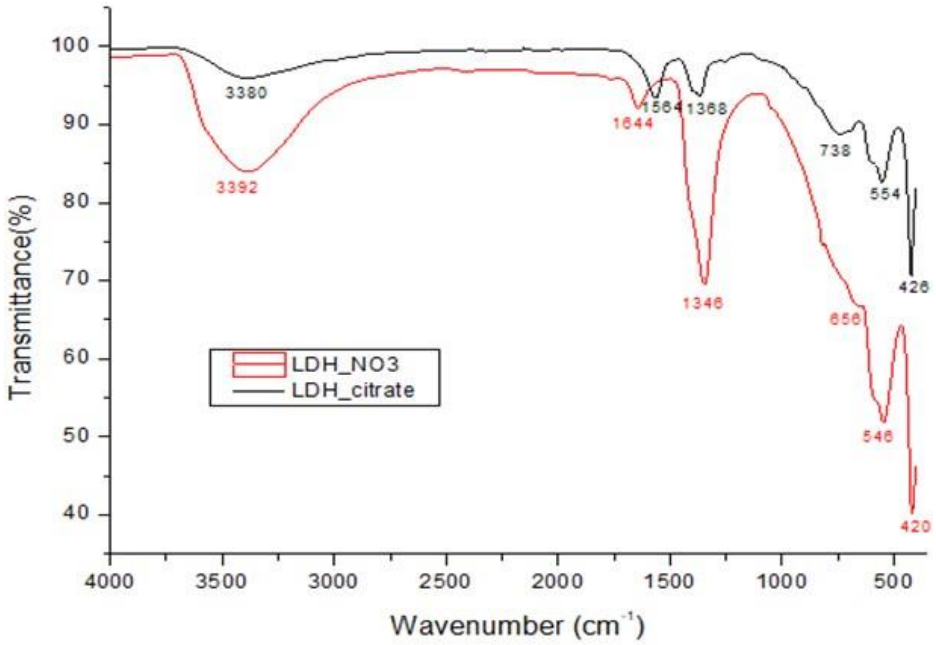

Figure 22: FT-IR spectra of ZnAl-NO_3-LDH vs ZnAl-citrate-LDH.

Figure 23 compares the FT-IR spectra of the base material (LDH-NO_3) and LDH-tartrate. Two bands of small intensity, at 1120 and 1080 cm^{-1} can be observed in the FT-IR spectra of the LDH-tartrate, that can be ascribed to two stretching vibrations of the alcoholic groups in tartrate anion (CO bond) [69]. In the intercalated materials, LDH-citrate and LDH-tartrate, the spectra show that the characteristic band of the nitrate group – 1346 cm^{-1} – is not present, which confirms the success of the intercalation with the inhibitors.

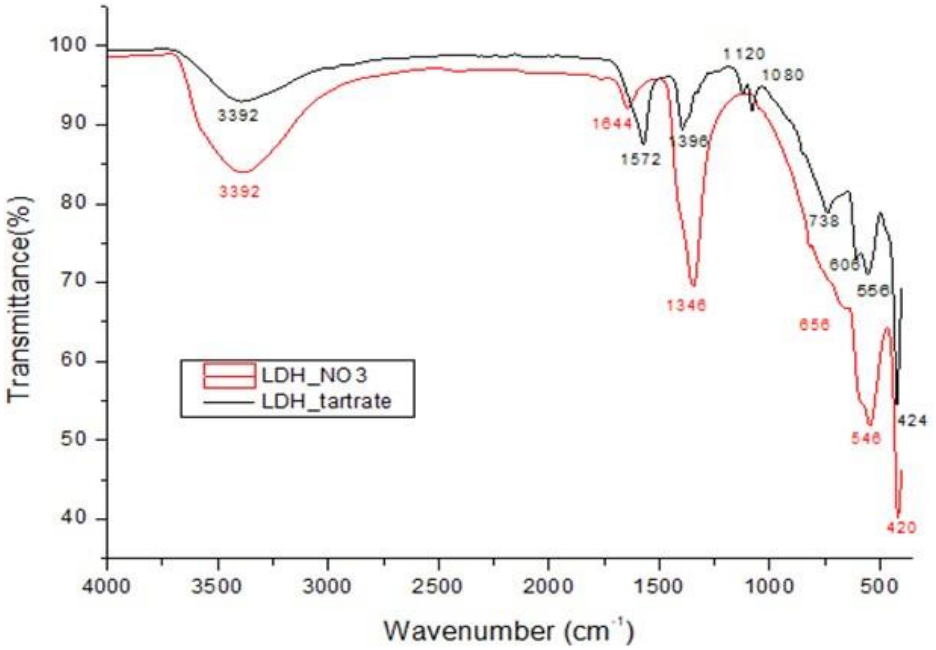

Figure 23: FT-IR spectra of ZnAl-NO_3 -LDH vs ZnAl-tartrate- LDH.

3.2. Encapsulation/LDH functionalization with silica

The previous studies were performed to analyse the performance of the inhibitors when integrated directly in a concrete mixture. In this section attempts were made to encapsulate the LDH within a mesoporous silica shell following procedures previously reported in literature [45], aiming to see the surface modification influence in the release profiles. However, release tests were not performed due to lack of time. The functionalized materials LDH-NO_3 and LDH-citrate were analysed using FT-IR spectroscopy and SEM/TEM. As mentioned above in section 2.4., the functionalization was tested varying some of the reactants concentration and quantities.

The following spectra correspond to the infrared spectrum of LDH-NO_3 in comparison with its encapsulated version, using the indicated quantities in the procedure (Figure 24) and 10 times the indicated quantities in the procedure (Figure 25).

After functionalization, it was noticed that the identifiable band of stretching mode of hydroxide groups (3300-3470 cm^{-1}) reduced greatly, the characteristic band of nitrate group almost disappeared (around 1350 cm^{-1}) and the bands representative of the bonds of metal-oxygen (M-O) and metal-oxygen-hydrogen (M-O-H) (800-400 cm^{-1}) were also very diminished.

The major differences found between the spectra of LDH-NO_3 and LDH-NO_3@$mSiO_2$, maintaining procedure proportion, were the presence of N-H bounding of the surfactant (CTAB) at 2854 and 2924 cm^{-1}, the intense peak at 1029 cm^{-1}, characteristic of Si-O bounding.

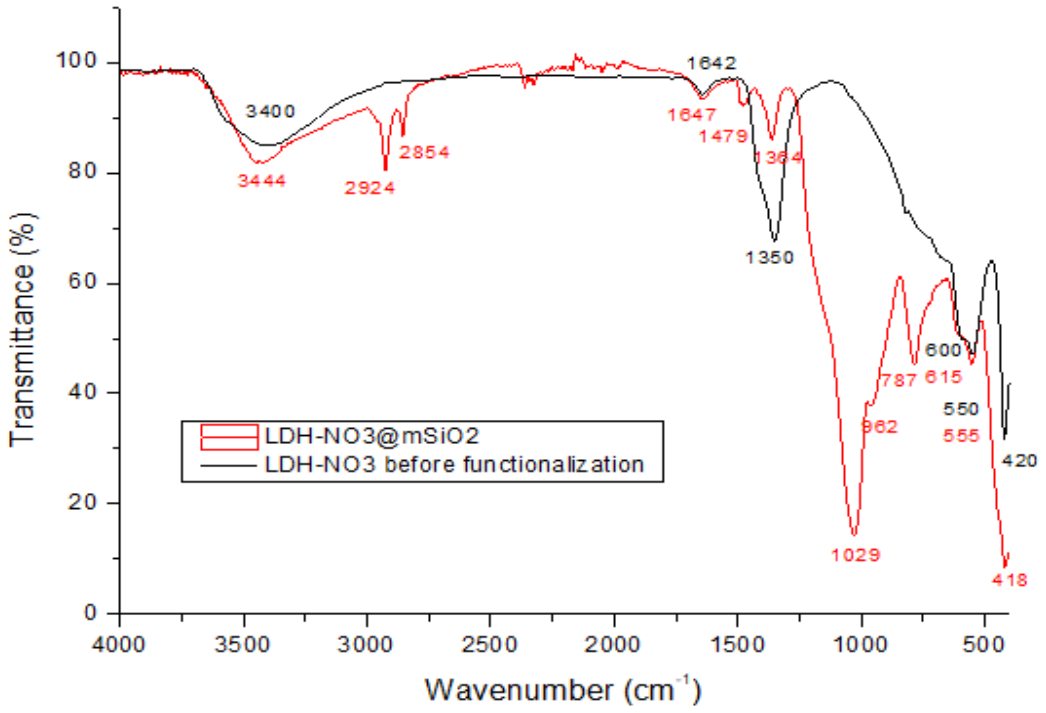

Figure 24: FT-IR spectra of LDH-NO_3 before encapsulation (black) and LDH-NO_3@$mSiO_2$ (red) nanocapsules (procedure proportion maintained).

In Figure 25, it was also observed the characteristic peak of Si-O bounding at 1064 cm^{-1} and the absence of nitrate's group characteristic band at 1350 cm^{-1}. In this trial, there was not found the characteristic peaks of N-H bounding of CTAB.

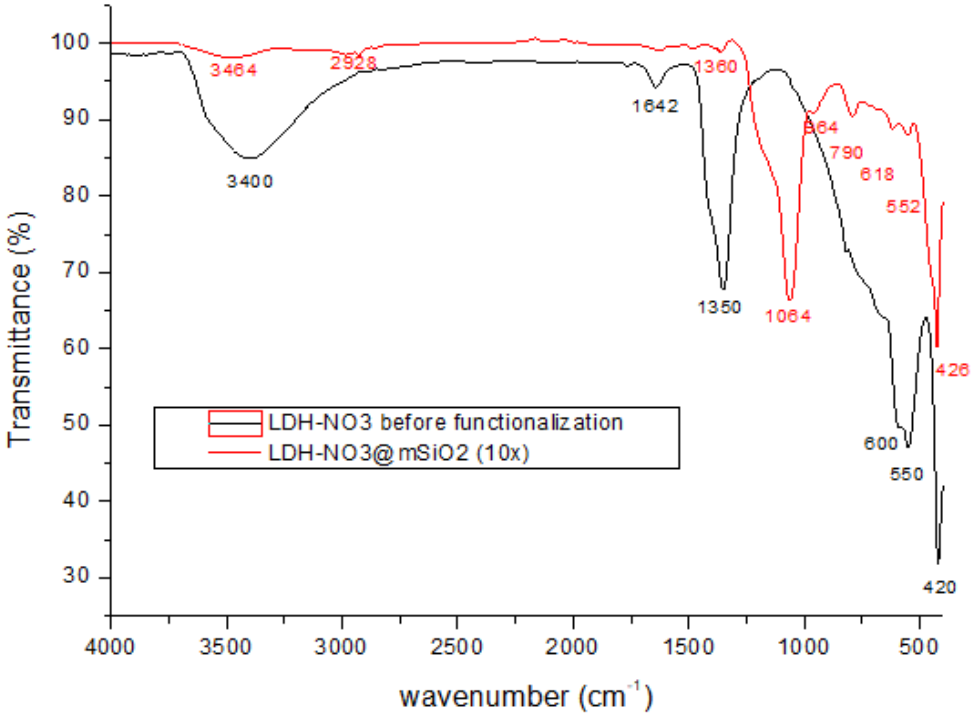

Figure 25: FT-IR of LDH-NO_3 before functionalization (black) and LDH-NO_3@$mSiO_2$ (red) nanocapsules (with reactants quantities 10 times superior).

According to Madejová et al., peaks below 1200 cm^{-1} correspond to the intense Si-O-Si stretching and bending vibrations [70]. In the spectrums of LDH-NO_3@$mSiO_2$ maintaining the procedure proportion and using the reactants quantities 10 times superior, both bands were verified. For the spectrum of Figure 24, the Si-O-Si stretching and bending bands appear at 1029 cm^{-1} and at 787 cm^{-1}, respectively. In the Figure 25, the spectrum of the nanocapsules of LDH-NO_3 and silica using reactants quantities 10 times superior (red) showed the two same peaks at 1064 cm^{-1} and 790 cm^{-1}, though less intense. The appearance of the characteristic band of Si-O bond showed the success of the functionalization.

Figure 26 depicts the FT-IR spectrum of LDH-citrate before and after encapsulation using the procedure proportion. In this spectrum, can be also observed the two stretching and bending Si-O-Si bands at 1051 cm^{-1} and 791 cm^{-1}, respectively.

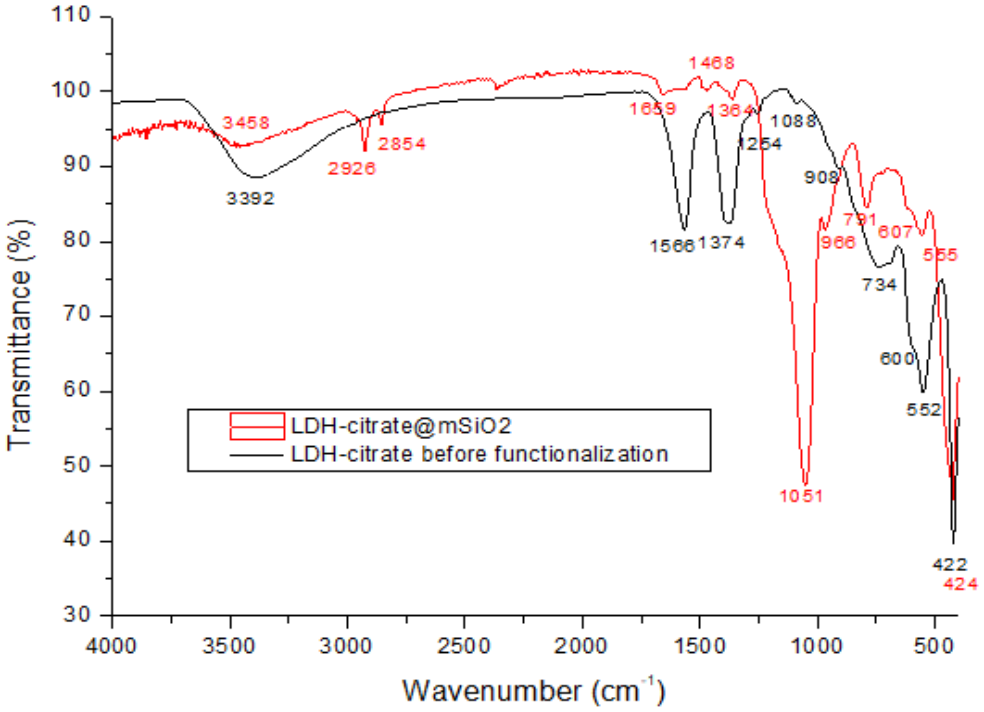

Figure 26: FT-IR of LDH-citrate before encapsulation (black) and LDH-citrate@mSiO$_2$ (red) nanocapsules (procedure proportion maintained).

Using SEM, it was possible to confirm the morphological structure of the particles prepared and TEM returns the structure and crystallinity of the samples. In Figure 27, microscopic images of silica particles and LDH are exposed and it was observable a heterogeneous suspension, being identifiable some LDH lamellas and some parts that could correspond to silica moieties. Observing the images captured, it was not possible to conclude if the encapsulation was successful. It would be necessary to repeat the encapsulation for further interpretation.

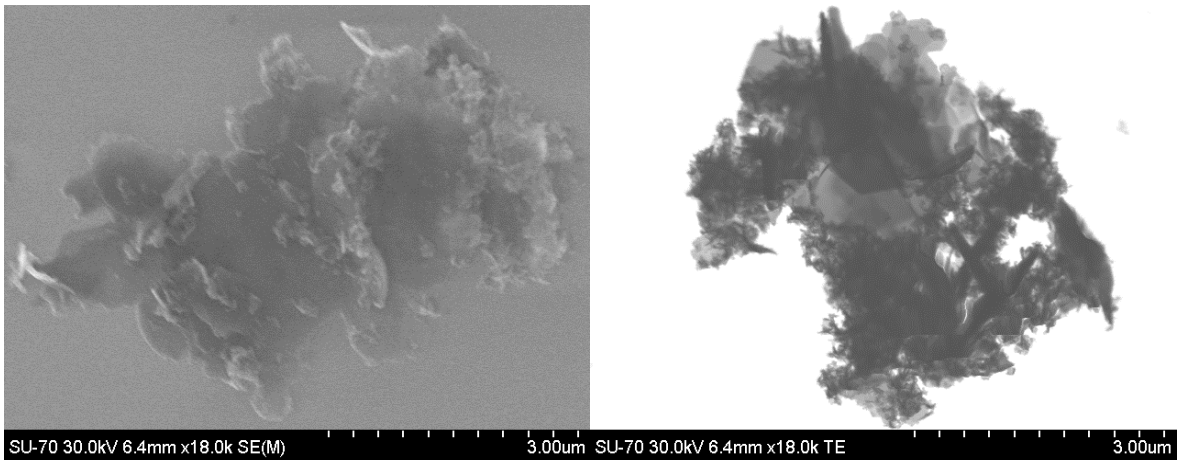

Figure 27: SEM image (left) and TEM image (right) images of LDH-NO$_3$@mSiO$_2$, using 10 times the quantity of reactants.

3.3. Release study of corrosion inhibitors from LDHs

The release of inhibitors from LDH galleries was assessed in NaCl solutions with different concentrations (5, 50 and 500 mM), since chloride anion is known to be one of the most important corrosion triggers. The released inhibitor was monitored and quantified by HPLC as described before in the experimental section.

Overall, as the chloride ion concentration increased, the amount of inhibitor released increased as well, as shown by the release profiles of the three inhibitors in Figure 28, 29 and 30. This event can be explained by the anionic-exchange ability of LDHs. The higher the concentration of chlorides in solution, the higher is the anionic-exchange and, consequently, the higher is the release of corrosion inhibitors. The profiles showed precisely the direct relation between the medium concentration in NaCl and the amount of inhibitor released. In general, the release of inhibitor increased with time, however, this was not the case for citrate, probably due to degradation of the compound in solution. In the release profiles of nitrite ([NaCl]=5, 50 and 500 mM) and tartrate ([NaCl]=50 and 500 mM), it was possible to identify two stages of release. When the LDHs intercalated with inhibitors are exposed to the sodium chloride solutions, the interlayer anions move from the interlayer spacing to the surroundings. This displacement is promoted by the concentration gradient between the inhibitor and the aggressive specie. The first hours of the release and the crescent phase in the profile correspond to the higher concentration gradient. When the inhibitors quantity in both sides (between the double layer of hydroxides/metals and the solution) equalize, the equilibrium is reached and the second stage of the release is achieved.

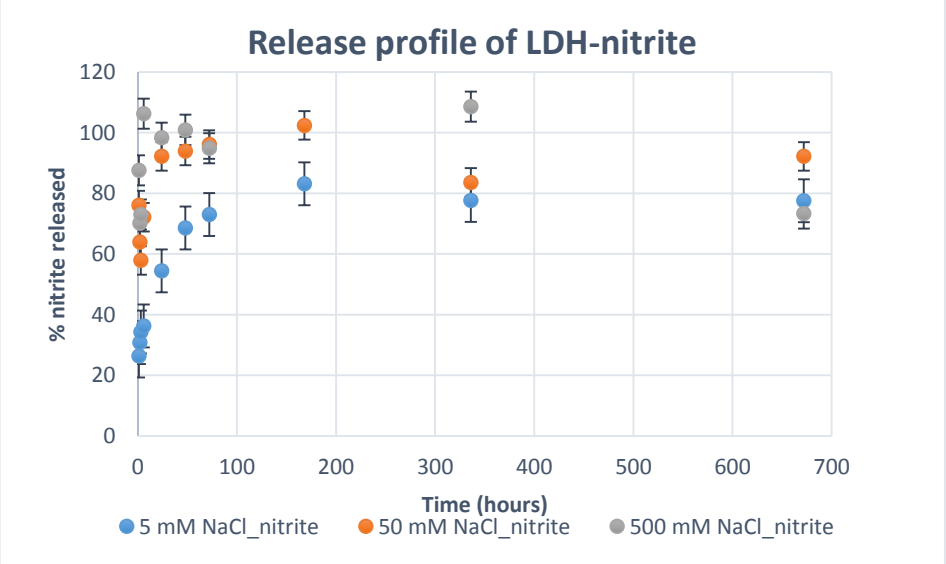

Figure 28: Release profile of LDH-nitrite at [NaCl]=5,50 and 500 mM and respective standard deviation.

In the case of the nitrite release, although it was observed some oscillating values, the profiles showed an exponential profile that is coincident with the behaviour exposed before. The most clear profiles were observed in the lower NaCl concentration solutions, while, at 500 mM of NaCl, the inhibitor's amount suffered some oscillation. There are some values above 100 %, which can be associated to a systematic error during the aliquots collection in the experimental procedure.

The following graphic depicts the release profile of citrate and it revealed to be the more disperse.

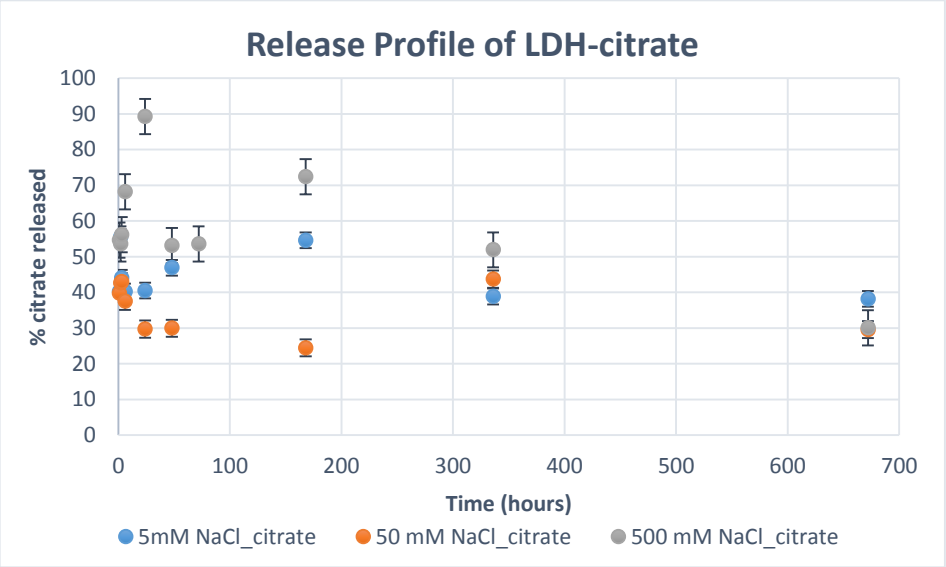

Figure 29: Release profile of LDH-citrate at [NaCl]=5,50 and 500 mM and respective standard deviation.

It was observed that the obtained inhibitor quantities oscillated over time, revealing a decrease for the higher chloride solutions (50 and 500 mM) after 2 weeks. There was not observable the expected profile and the drop of inhibitors amount might indicate that some samples suffered degradation or complexation in solution.

The release profile of LDH-tartrate (Figure 30, below) showed an evolutional behaviour, which means that, at the less concentrated solutions in sodium chloride, there were some evidences of a crescent profile after 2 weeks, after which the amount of released inhibitor decreased. At intermediate NaCl solution (50 mM), the released tartrate quantity was considerably superior and it was visible the initial phase of release during the first hours. When the concentration could stabilize, in the second phase of the release, tartrate quantity in solution revealed a decrease. Only for the suspension prepared with the highest concentration of NaCl was obtained a clearer profile with the expected development.

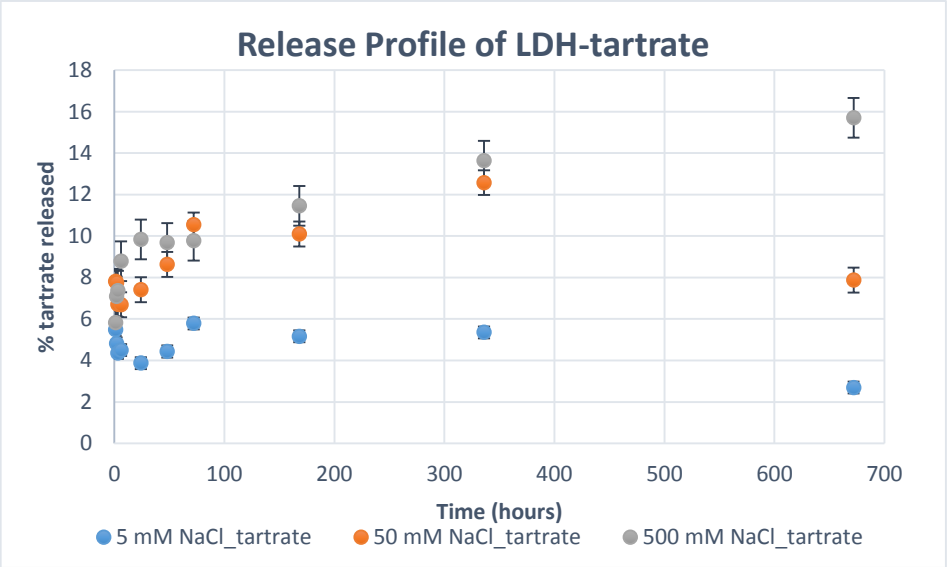

Figure 30: Release profile of LDH-tartrate at [NaCl]=5,50 and 500 mM and respective standard deviation.

In order to compare the amount of released inhibitor between the immobilized inhibitors at [NaCl]= 500 mM, the different profiles of corrosion inhibitors were plotted together (Figure 31).

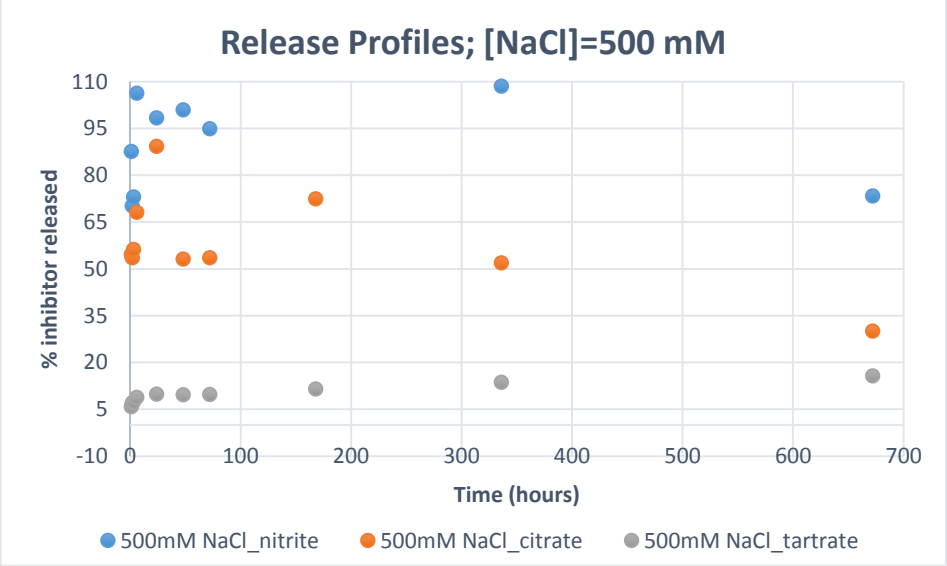

Figure 31: Comparative release profile of LDH-nitrite, LDH-citrate and LDH-tartrate at [NaCl]=500 mM.

The upper representation showed more clearly the differences between the quantities of inhibitors released, since the profiles were more evident when exposed to a more concentrated solution in chlorides. The profiles showed that the amount of nitrite released was 2 times higher than citrate and 10 times higher than tartrate. Therefore, due to its higher quantity in contact with the surface intended to protect, it would be expected a better protective performance from nitrite than from the remain inhibitors.

3.3.1. Kinetic models of the release

After the quantification of the amount of inhibitor released over 4 weeks, the results were adjusted to three different kinetic models: the power law, the Higuchi's model and the pseudo-second order model.

The simplest model of the Power Law equation or Peppa's model relates the concentration at a certain time and at equilibrium, which represents the release of a solute, being the solute, in this case, the inhibitive species intercalated into the LDHs and it is presented in the equation below.

Considering the Fickian diffusion in a thin film in Equation 9, two possible limiting conditions were found. On one hand, the expression indicates that the first 60% of the fractional release can be characterized by a constant multiplied by the square root of time, and on the other hand, when the releasing rate is independent of time, the kinetics order is zero.

$$\frac{M_t}{M_\infty} = 4.\left[\frac{D.t}{\pi.l^2}\right]^{1/2} \quad \text{Eq.9}$$

$$\frac{M_t}{M_\infty} = k_1.\sqrt{t} + k_2.t \quad \text{Eq.10}$$

Being M_t, the quantity of inhibitor at t hours of release; M_∞, the quantity of inhibitor at equilibrium; D, the diffusion coefficient; l, the initial film thickness and k_1 and k_2, constants that incorporate the characteristics from both sides (the solution and the solute).

Many release processes are found to fit between these two limiting cases. Therefore, combining Equation 9 (Fickian mechanism) and Equation 10 (Non-Fickian mechanism), the Equation 11 can be.

$$\frac{M_t}{M_\infty} = k.t^n \quad \text{Eq.11}$$

Where k is a constant that incorporates the characteristics from both sides (the solution and the solute) and n is the diffusional exponent, which can indicate the transport mechanism. When the geometry of the particle equates to a thin film, n is equal to 0.50, the diffusion follows a quasi-fickian model and when n is greater than 0.50, the diffusion is anomalous or non-fickian [71],[72]. If the obtained reaction order is lower than 0.5, the inhibitors diffusion followed Fick's law.

The Higuchi's model relies on the release of a compound from a thin layer to the environment. To describe the inhibitor concentration gradient, Higuchi used a pseudo-state approach, which can be considered when the system initially has an excess of inhibitor. When the initial inhibitor concentration is much higher than its solubility, it takes longer to dissolve the inhibitor excess at a distance h from the surface in question. Therefore, at this position, the concentration is considered to be constant during a certain amount of time.

If the "gel" does not swell or dissolve, pseudo-steady state conditions are provided for inhibitor diffusion. Using Fick's second law, the increasing amount of released inhibitor from the interlayer space of LDHs at time *t*, M_t, can be described as follows:

$$\frac{M_t}{A} = h.(C_{ini} - \frac{C_s}{2}) \quad \text{Eq.12}$$

Considering a simple geometry for the mass transport and after derivation, the equation obtained is:

$$\frac{M_t}{A} = \sqrt{(2.C_{ini} - C_s).D.t.C_s} \quad \text{Eq.13}$$

Having considered an initial excess of the inhibitor ($C_{ini} >> C_s$),

$$\frac{M_t}{A} = \sqrt{2}.C_{ini}.D.t.C_s \quad \text{Eq.14}$$

Equation 14 can be simplified to the following form:

$$\frac{M_t}{A} = k.\sqrt{t} \quad \text{Eq.15}$$

Where $k = \sqrt{2}.C_{ini}.D.C_s$; being C_{ini}, the initial concentration of the inhibitor; C_s, inhibitor concentration at the surface; *A*, contact area.

The classical Higuchi's equation describes a "square root of time" release kinetics [73].

It was also used the Pseudo-second order (PSO) model that initially was deduced by Ho and Mckay for the kinetic analysis of adsorption [74]. From the PSO model based on adsorption capacity:

$$\frac{dq_t}{dt} = k.(q_e - q_t)^2 \quad \text{Eq.16}$$

Being the driving force (q_e-q_t), proportional to the free fractions of active sorption spots. Integrating the expression considering the initial conditions (*t*=0, q_t=0), the equation obtained for pseudo-second-order law is:

$$q_t = \frac{q_e^2.k.t}{1 + q_e.k.t} \quad \text{Eq.17}$$

Simplifying the expression and applying linearity:

$$q_t = \frac{t}{\frac{1}{k.q_e^2} + \frac{t}{q_e}} \rightarrow \frac{t}{q_t} = \frac{1}{k.q_e^2} + \frac{t}{q_e} \quad \text{Eq.18}$$

Where q_t and q_e are the amount of adsorption (g/kg) at time *t* and equilibrium, respectively; *t* is adsorption time (min); *k* is the pseudo-second-order rate constant of adsorption (kg/(g.min)). In this work, the rate of adsorption is replaced by the percentage of released inhibitor and the parameters of the PSO model are determined resorting to the slope and y-interception obtained after representation and linear regression of $\frac{t}{q_t}\ vs\ t$ [75].

The three kinetic models were applied for all inhibitors and sodium chloride concentrations. All fittings will be presented in section B of the Appendix. Generally, the model that fitted the results

better was the Power Law (Peppa's Model) and the pseudo-second order model was the least applicable. For nitrite, the adjustments to the Power Law were better for the higher concentrations in chlorides, as can be verified in Table 5. For the remaining inhibitors, varying NaCl concentration and inhibitor, the best model was also Power Law (Table 5). However, for citrate, the kinetic constants were slightly oscillating. For the intermediate chloride concentration, the kinetic constant should be between 0.02069 and 0.02154, which was not observable, and its coefficient of determination was the lowest. For tartrate, the kinetic constants and the correspondent coefficient of determination decreased with the increasing of chlorides concentration.

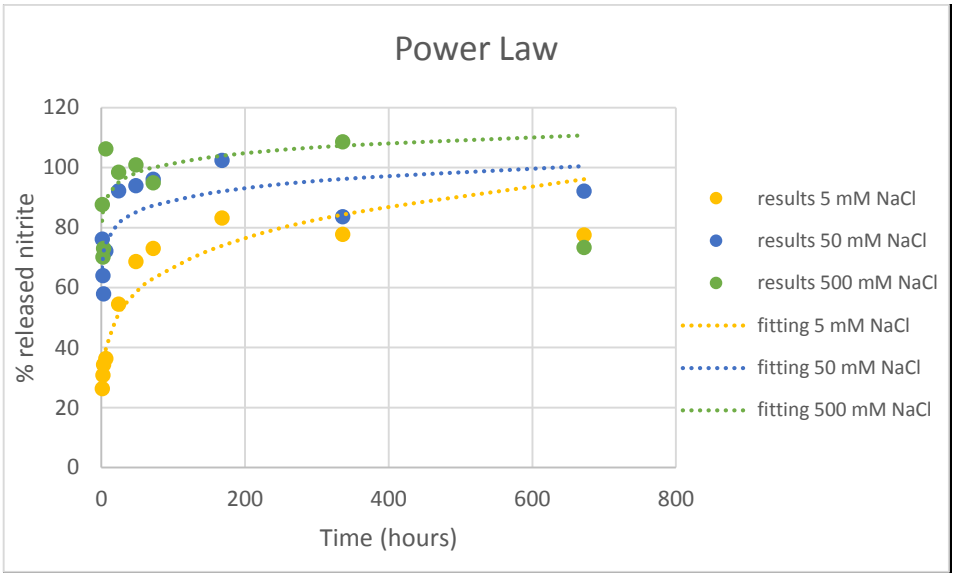

Figure 32: Release profiles of nitrite ion in [NaCl]=5, 50 and 500 mM solutions. Fittings of experimental data to Power Law (Peppa's Model).

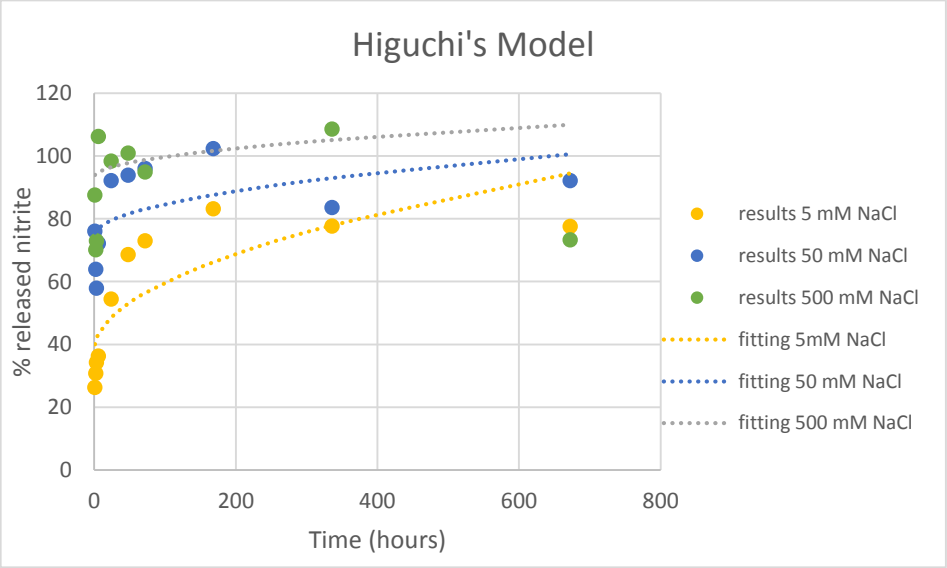

Figure 33: Release profiles of nitrite ion in [NaCl]=5, 50 and 500 mM solutions. Fitting of experimental data to Higuchi's Model.

Regarding to Higuchi's model, the adjustment of the nitrite experimental values was good, even though the kinetic constants were decreasing, which was not expectable. The pseudo-second order model was the less adjustable to the data.

Analysing the kinetic constants (Table 5), it was concluded that the kinetic model that had the best adjustment to the experimental data was Peppa's model.

Table 5: Kinetic constants of each system for Peppa's model, Higuchi's model and Pseudo-second order (PSO) model, where * indicates kinetic constants of non-adjustable fittings and coefficient of determination of the fittings.

System\ kinetic constant's and r^2	Peppa's model	r^2	Higuchi's model	r^2	PSO model	r^2
[NaCl]=5 mM; nitrite	0.004126	0.9731	2.183	0.8418	0.001140	0.8935
[NaCl]=50 mM; nitrite	0.007408	0.9970	0.9998	0.8418	*	0.6505
[NaCl]=500 mM; nitrite	0.01028	0.9984	0.6438	0.8418	*	0.1876
[NaCl]=5 mM; citrate	0.02069	0.9999	*	0.9249	*	0.2354
[NaCl]=50 mM; citrate	0.02323	0.9982	*	0.8418	*	0.1571
[NaCl]=500 mM; citrate	0.02154	0.9986	*	0.0649	*	0.0051
[NaCl]=5 mM; tartrate	0.1940	0.9993	*	0.8418	*	0.0005
[NaCl]=50 mM; tartrate	0.05372	0.9974	0.1180	0.8418	*	0.4698
[NaCl]=500 mM; tartrate	0.02300	0.9873	0.3523	0.8418	0.003240	0.9733

The rate constants for each model were determined and, through these values, it was possible to infer some information about the transport of the inhibitor's anions. As mentioned before, increasing the concentration of chlorides in solution, increases the anionic-exchange ability of LDHs. Therefore, it was expected to observe an increase of the rate constants with the increasing of chloride ion concentration. Nitrite experimental data was well adjusted to the model and the rate constants were crescent, which revealed the relation between the anionic-exchange ability and the rate constants. The same was not observable for Higuchi's and Pseudo-second order models. A negative rate constant has no physical meaning and, in these cases, showed that the exchange cannot be adjusted to the proposed kinetics models.

3.4. Electrochemical Impedance Spectroscopy (EIS) Study

Electrochemical impedance spectroscopy was used to evaluate the anti-corrosion performance of the LDH-inhibitors. Several EIS curves were represented to allow the interpretation of the data obtained. For 24 hours and 2 weeks of immersion in NaCl solutions, was traced the distribution of impedances

of the three NaCl concentrations for LDH-NO_3, LDH-NO_2, LDH-citrate, LDH-tartrate and reference solution (NaCl). Then, fixating the frequency 0.01 Hz, for each NaCl concentration and, for 24 hours and 2 weeks of contact, the impedances of each LDH and reference solution were represented. Since the concentration which caused higher degradation of steel substrate was at highest NaCl concentration (500 mM,), the correspondent impedance values were selected for comparison. The representations below allowed to verify the inhibitors behaviour after fixed periods of time in contact with carbon steel. Figure 34 showed the electrochemical impedances of NaCl solutions (ref) at 5, 50 and 500 mM and pH=13 (in the beginning of the study), after 24 hours and 2 weeks.

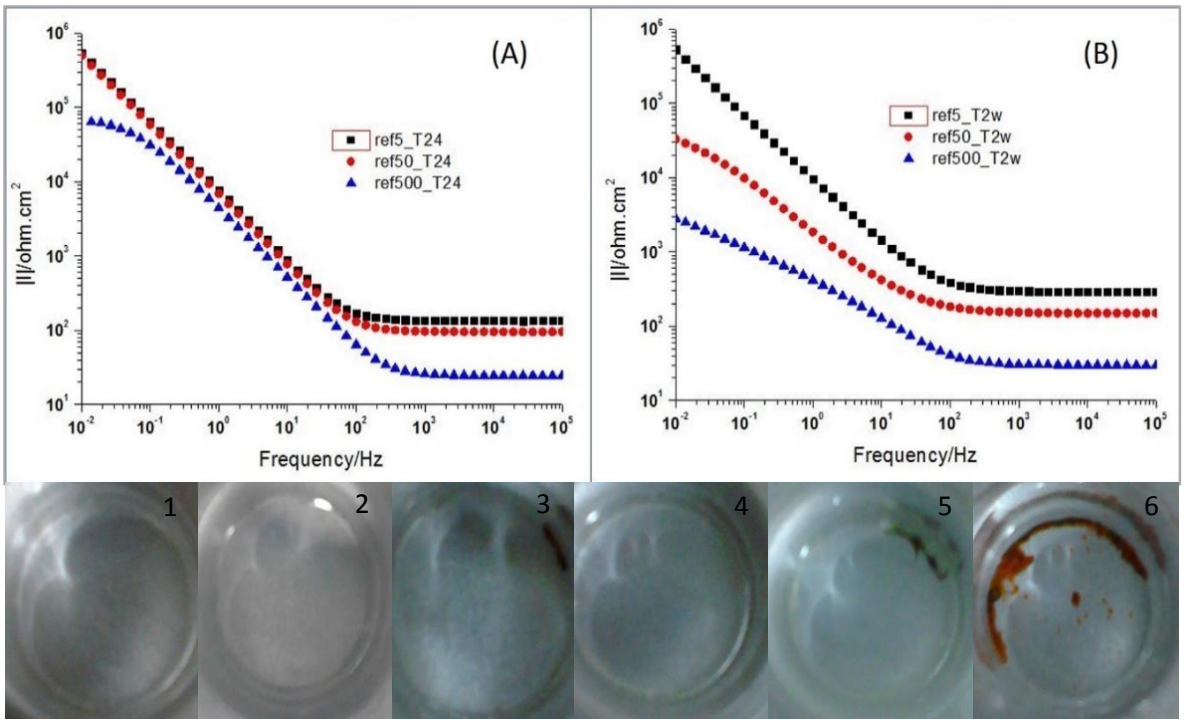

Figure 34: Impedance distribution after 24 hours (A) and 2 weeks (B) of contact with [NaCl]=5, 50 and 500 mM solutions (Reference) and pH=13; photographic recordings of carbon steel surface after 24 hours (T24) with [NaCl]=5, 50 and 500 mM (images 1, 2 and 3, respectively) and 2 weeks (T2w) with [NaCl]=5, 50 and 500 mM (images 4, 5 and 6, respectively).

Knowing that concrete's pH is, approximately, 13, the solutions were prepared to replicate concrete's conditions, namely the basicity. During the first hours, a passive and protective layer is formed over the carbon steel board, protecting it from the chloride ion action. However, after some time, due to the contact of the solution with the atmosphere (presence of CO_2) the pH value starts to decrease. Thus, chloride anions start to penetrate this protective layer and the surface became more vulnerable to corrosion attack.

For the higher concentration of NaCl, after 24 hours, the impedance values were lower than for 5 and 50 mM NaCl solutions and it can be confirmed by image observation (Figure 34), where it was found

spots of corrosion. After 2 weeks, the impedance values are very distinct, being detectable differences of the orders of magnitude. The lower the chloride concentration, the higher the resistance to corrosion. Observing images 4, 5 and 6 of Figure 34, this fact was confirmed, due to the increase of corrosion spots and rust as chloride concentration in solution increased.

Figure 35 is referent to the base material, LDH-NO_3, which was also tested and assessed its behaviour in sodium chloride solutions.

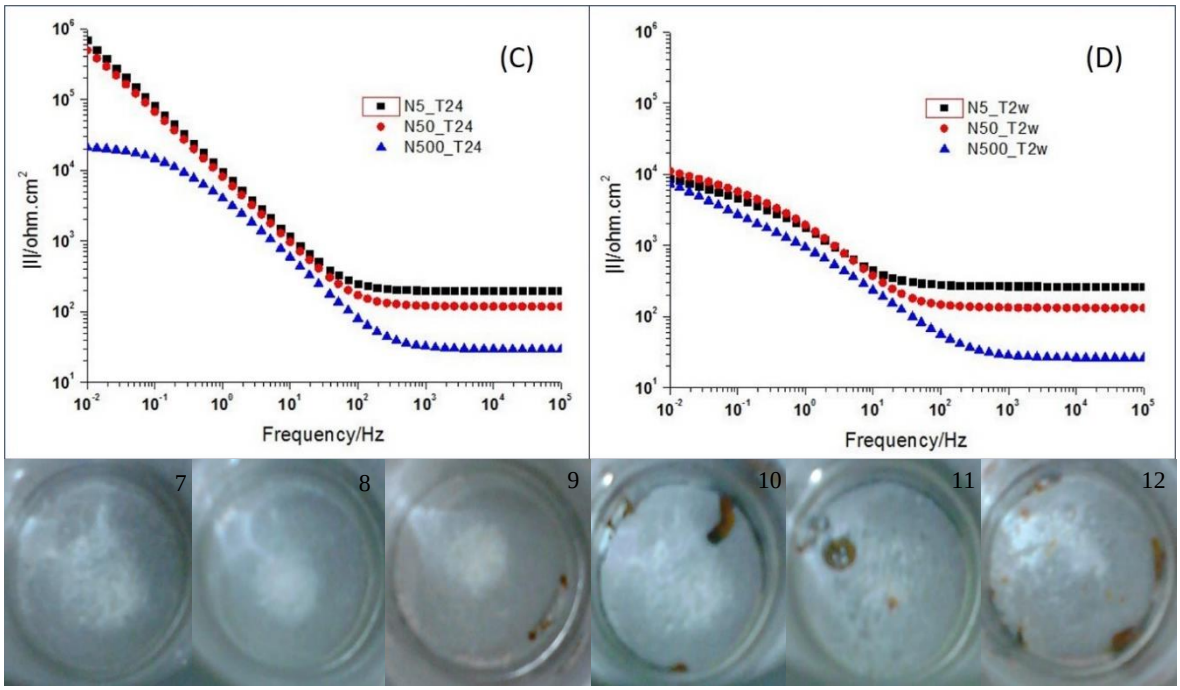

Figure 35: Impedance distribution after 24 hours and 2 weeks of contact for LDH-NO_3 in [NaCl]=5, 50 and 500 mM (C, D) and pH=13; photographic recordings of carbon's steel surface after 24 hours (T24) (images 7, 8 and 9) and 2 weeks (T2w) (images 10, 11 and 12).

It was verified that after 24 hours (Figure 35 C), the impedance values for the solutions with lower concentrations of chlorides were superior, while for the higher NaCl concentration suspension, the resistance was much lower, which could be confirmed by the corrosion spots visible in image 9. After 2 weeks, the impedance values were all around the same magnitude, which revealed the ineffectiveness of LDH-NO_3 for carbon steel protection, increasing the corrosion activity for specific conditions when compared with reference. The images 10, 11 and 12 show the formation of oxide blisters and spots of active corrosion.

The three inhibitors tested in this study were identified as *B* for LDH-NO_2, *C* for LDH-citrate and *D* for LDH-tartrate.

In Figure 36 is presented the information collected relative to the suspensions with LDH-NO_2. Nitrite is already, industrially, included in anti-corrosion solutions because of its immediate action in

corrosion protection. For more prolonged solutions, nitrite must be combined with other corrosion inhibitor or encapsulated to achieve the desired effect.

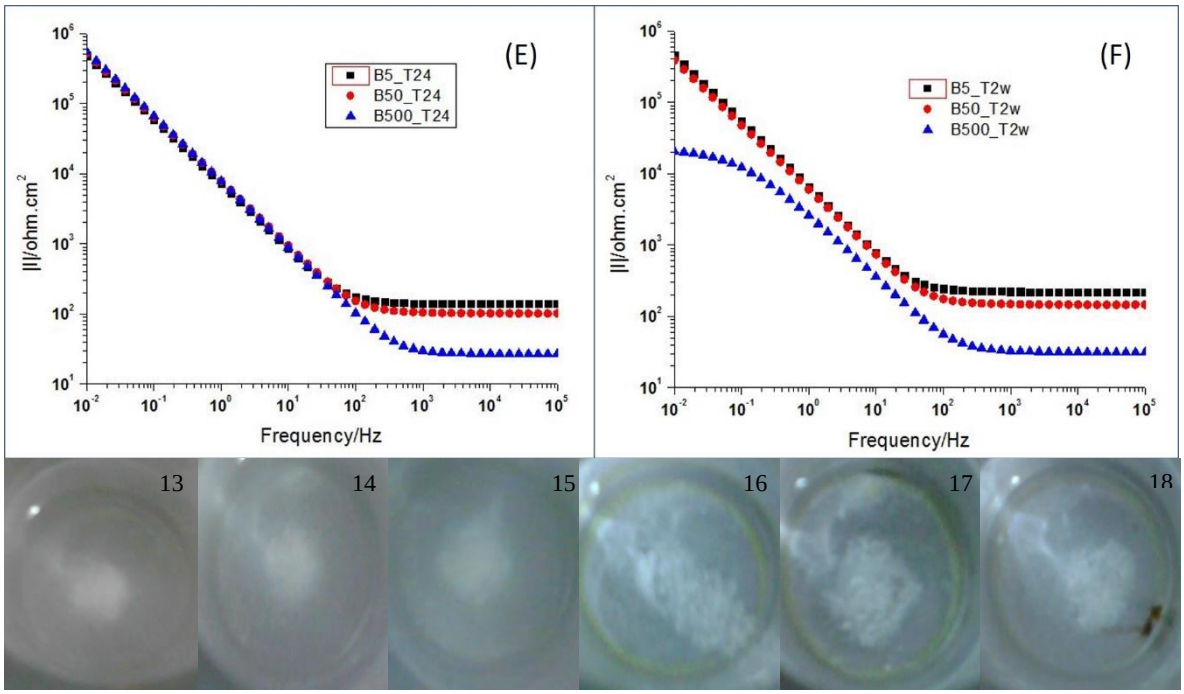

Figure 36: Impedance distribution after 24 hours and 2 weeks of contact for LDH-NO_2 (B) in [NaCl]=5, 50 and 500 mM (E, F) and pH=13; photographic recordings of carbon's steel surface after 24 hours (T24) (images 13, 14 and 15) and 2 weeks (T2w) (images 16, 17 and 18).

After 24 hours, nitrite anion in solution offered anti-corrosive protection, independently of the chloride concentration, inferred by the impedance values in image E of Figure 36. At short periods of time, besides the effect of higher pH values, nitrite itself offers the same type of protection, which means that, onto the carbon steel surface, nitrite forms a physical barrier against corrosion. Images 13, 14 and 15 showed no evidence of corrosion attack. After 2 weeks of contact with the aggressive species, the surfaces in contact with the suspensions of LDH-NO_2 with 5 and 50 mM NaCl solutions were free of corrosion spots, reflecting the anti-corrosive performance of nitrite at lower chloride concentrations. However, for the higher chloride concentration suspension, the resistance to corrosion decreased (Figure 36 F), revealing that, for higher aggression conditions of exposure to carbon steel, the passive layer gave in and the chlorides reached the surface, corroding the substrate. Figures 37 and 38 show the electrochemical impedance values and photographic evidences of citrate and tartrate performance as a corrosion inhibitors, respectively.

Observing the graphs (G) and (I), the impedance distributions of LDH-citrate and LDH-tartrate suspensions revealed to be very similar. At the higher NaCl concentration for citrate, the last value of impedance is slightly lower than for tartrate and it can be connected to the appearance of the small spots of corrosion observed in image 21 and the absence in image 27.

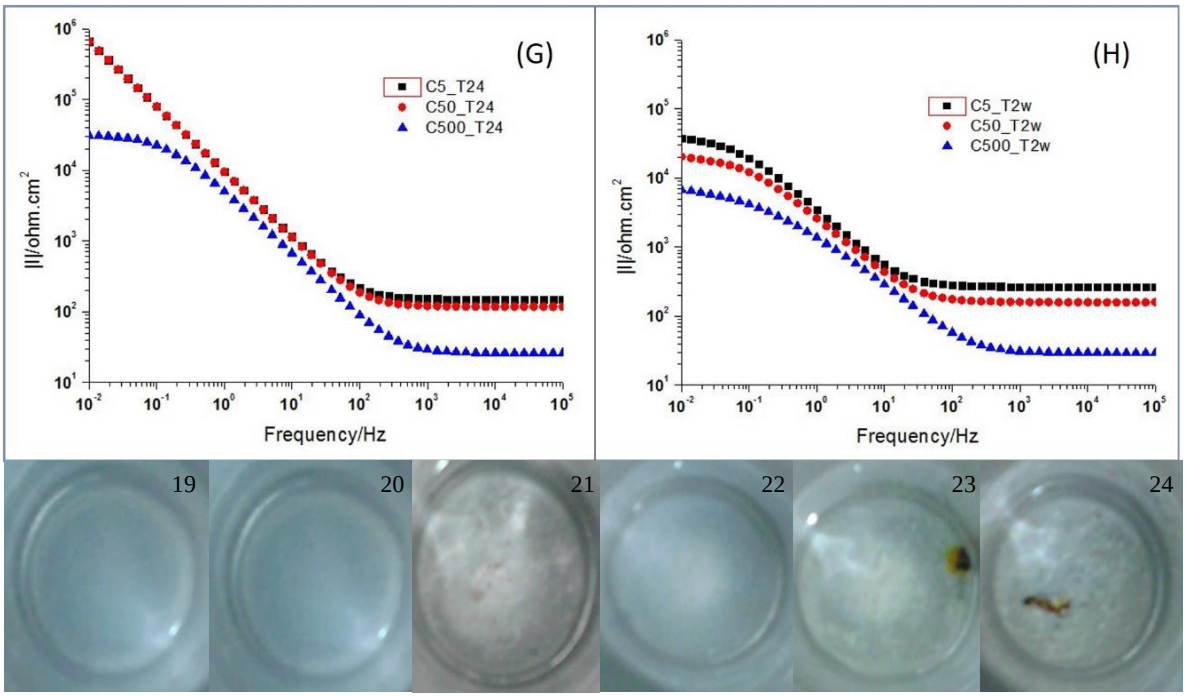

Figure 37: Impedance distribution after 24 hours and 2 weeks of contact for LDH-citrate in [NaCl]=5, 50 and 500 mM (G, H) and pH=13; photographic recordings of carbon's steel surface after 24 hours (T24) (images 19, 20 and 21) and 2 weeks (T2w) (images 22, 23 and 24).

After two weeks of contact, the steel surface showed blisters and spots of corrosion in contact with the more concentrated suspensions in chlorides, namely with [NaCl]= 50 and 500 mM (images 23 and 24 for citrate; images 29 and 30 for tartrate). For both inhibitors, the impedance values at these two NaCl concentrations were approximated. At lower concentrations of chlorides, tartrate revealed a slightly better performance as an anti-corrosive, when comparing the impedance values ($|I|_{citrate,T2w}=3\times10^4$ ohm.cm^2 and $|I|_{tartrate,T2w}=10^5$ ohm.cm^2). Comparing the steel surfaces for LDH-citrate and LDH-tartrate, after 2 weeks of immersion was also possible to observe that the ones in the presence of tartrate presented less corrosion attack and cleaner surfaces.

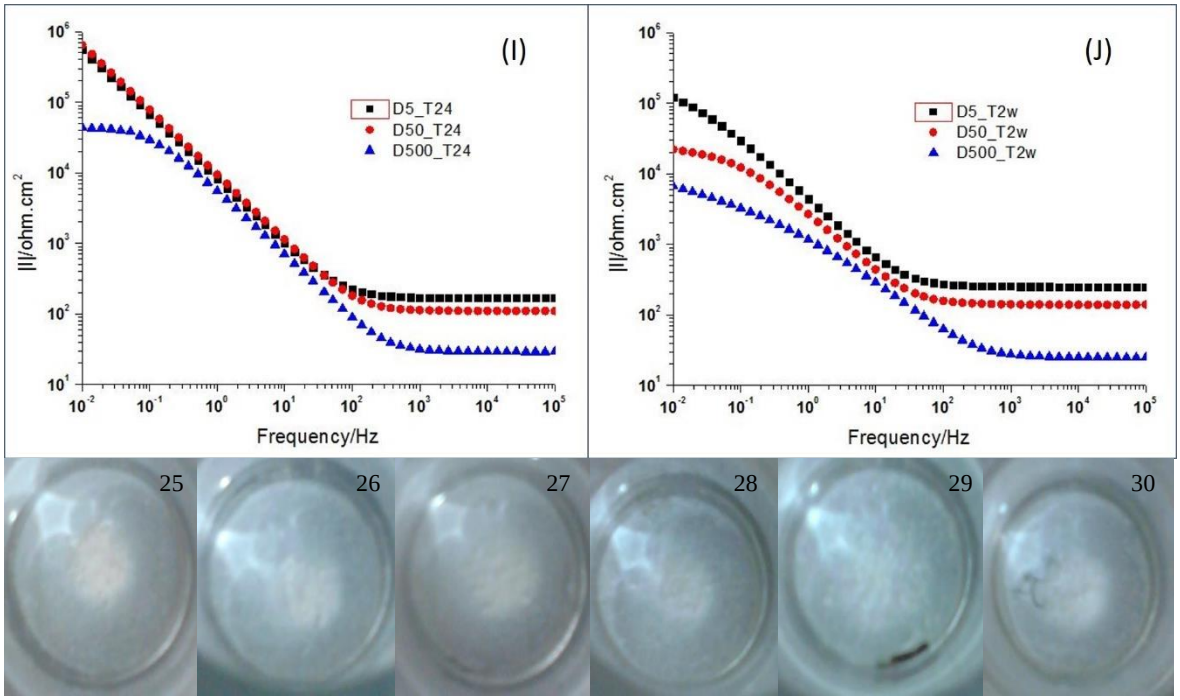

Figure 38: Impedance distribution after 24 hours and 2 weeks of contact for LDH-tartrate in [NaCl]=5, 50 and 500 mM (I, J) and pH=13; photographic recordings of carbon's steel surface after 24 hours (T24) (images 25, 26 and 27) and 2 weeks (T2w) (images 28, 29 and 30).

The impedance distributions of LDH-NO_2, LDH-citrate, LDH-tartrate, LDH-NO_3 (base material) suspensions and the reference solution at the higher chlorides concentration (500 mM), after 24 hours and 2 weeks, are depicted in Figure 39 (graphs K and L).

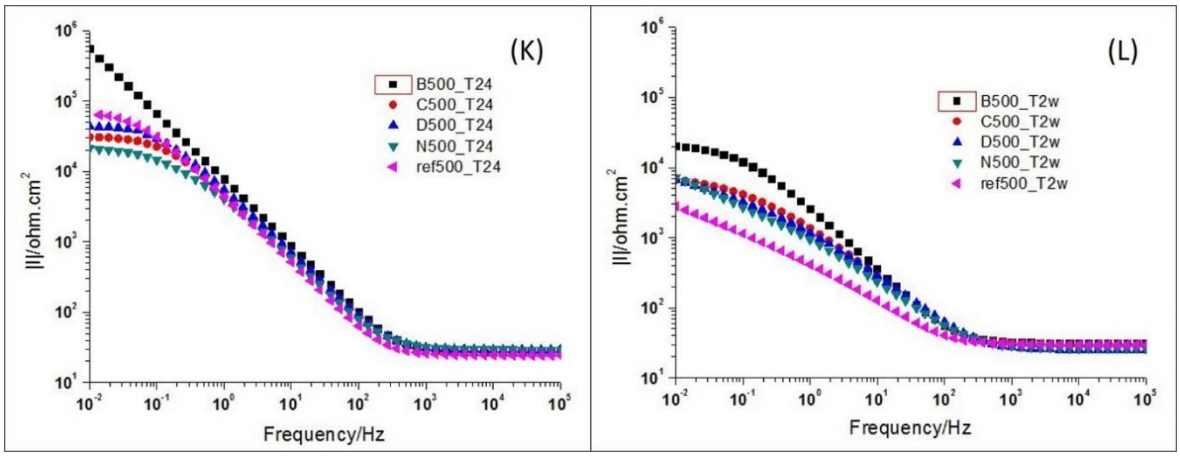

Figure 39: Impedance distribution of LDH-NO_2 (B), LDH-citrate (C), LDH-tartrate (D), LDH-NO_3 (N) and reference solution (ref) with [NaCl]=500 mM, after 24 hours and 2 weeks of contact with the carbon steel board.

It was detectable that, after 24 hours, nitrite showed the best performance, respecting to corrosion protection as expected and the remaining inhibitors were less effective as protective inhibitors. After 2 weeks of contact, the impedance values decreased one to two orders of magnitude, revealing that, in general, chlorides reached the substrate and the material started to corrode. However, comparing the impedances of the three inhibitors, LDH-NO_2 revealed that, even though passivation stage suffered declination and the surface experienced active corrosion, it was the inhibitor that offered a better performance and superior anti-corrosion protection.

The following figures represent the resistance to an alternated current at a fixed frequency (0.01 Hz), for different concentrations of the aggressive specie (chloride) and different LDH compositions.

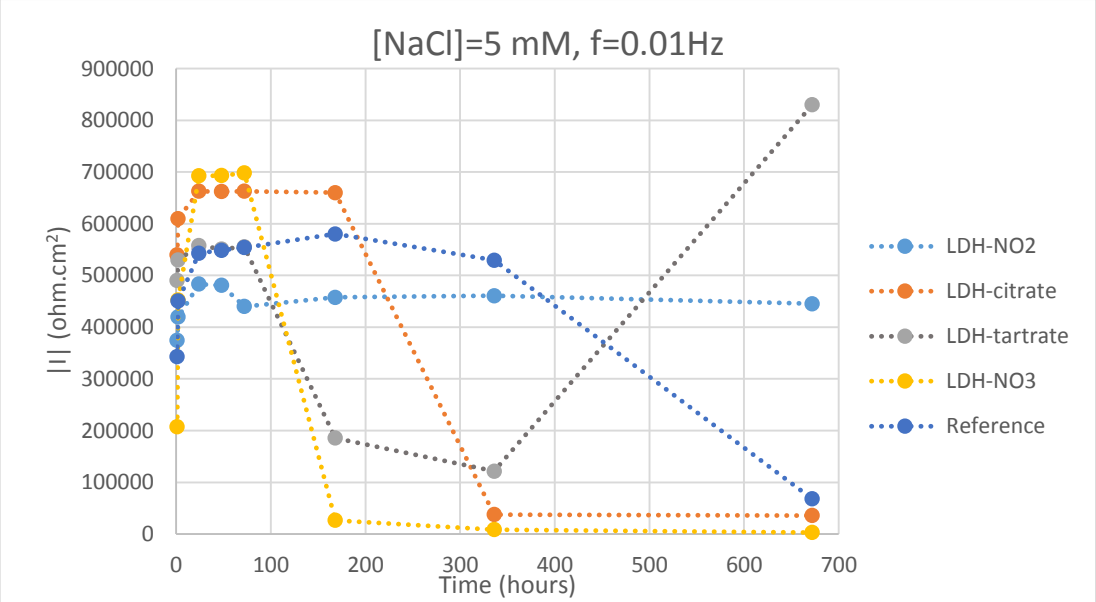

Figure 40: Impedance versus time at constant frequency for: LDH-NO_2 (light blue), LDH-citrate (orange), LDH-tartrate (grey), LDH-NO_3 (yellow) and reference-NaCl solution at 5mM (dark blue).

In Figure 40, it was observable that, for all suspensions until 72 hours of contact, the impedance values kept elevated due to the passive layer caused by the basicity of the suspensions in touch with the carbon steel board. At the less aggressive exposure conditions, LDH-NO_2 would have a lasting and stable performance, because, even when pH started to decrease, the nitrite anion in solution provided protection against the chloride corrosive activity.

Analysing the rest of the inhibitors, LDH-citrate provided an effective protection until the first week, after which started to fail as an inhibitor and LDH-tartrate efficiency declined after 72 h after exposure to the carbon steel substrate. The reference solution was a 5 mM sodium chloride solution that, even though, had no additive what so ever, its performance protecting carbon steel surface was good up to two weeks.

Observing LDH-tartrate impedance profile, it was observed that the last impedance value collected was much higher that would be expected given the release profile. This can probably be explained by a leak after a week. The leak was caused by spots of corrosion in the substrate and, after insulating again the tube, to the remaining suspension, was added fresh NaCl suspension (5 mM, pH=13), which may have caused the passivation of the substrate, resulting in a higher impedance value.

As the concentration of the intrusive specie increased, it was observable that the passivation effect from the high pH remained until 72 hours after the initial contact. LDH-NO_2 suspension was the only that preserved and improved its action, as can be validated in Figure 41.

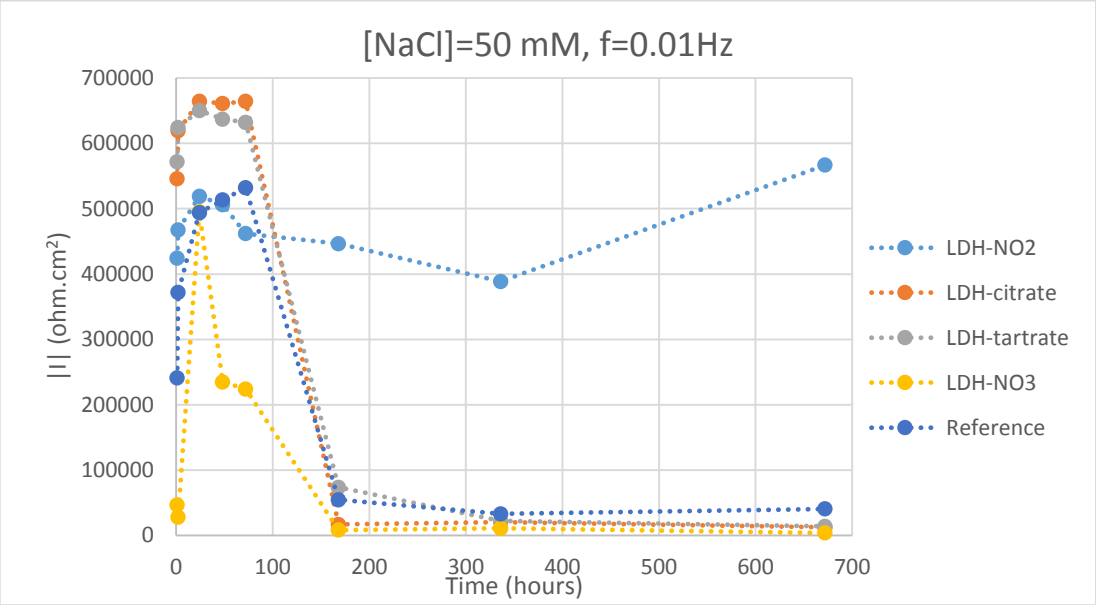

Figure 41: Impedance versus time at constant frequency for: LDH-NO_2 (light blue), LDH-citrate (orange), LDH-tartrate (grey), LDH-NO_3 (yellow) and reference-NaCl solution at 50 mM (dark blue).

In Figure 42, it was observable the materials reaction towards an intrusive specie at its higher concentration. When the surrounding conditions are very aggressive (500 mM), the passive layer failed very quickly (after the first hour), because of chloride higher concentration. Carbon steel surface suffered corrosive attacks, which were proven with the photographic proves at the time of measurement after 24 hours and 2 weeks (Figure 36, 37 and 38). The inhibitor that offered the most prolonged anti-corrosive effect was nitrite and, though, it failed sooner than at lower concentrations of chloride, its performance was the expected. Earlier, the inclusion of nitrite as an anti-corrosive additive was discussed, due to its effectiveness as an early approach towards corrosion. As a long-term option, nitrite must be combined with other anti-corrosive solutions, to provide a better performance to concrete.

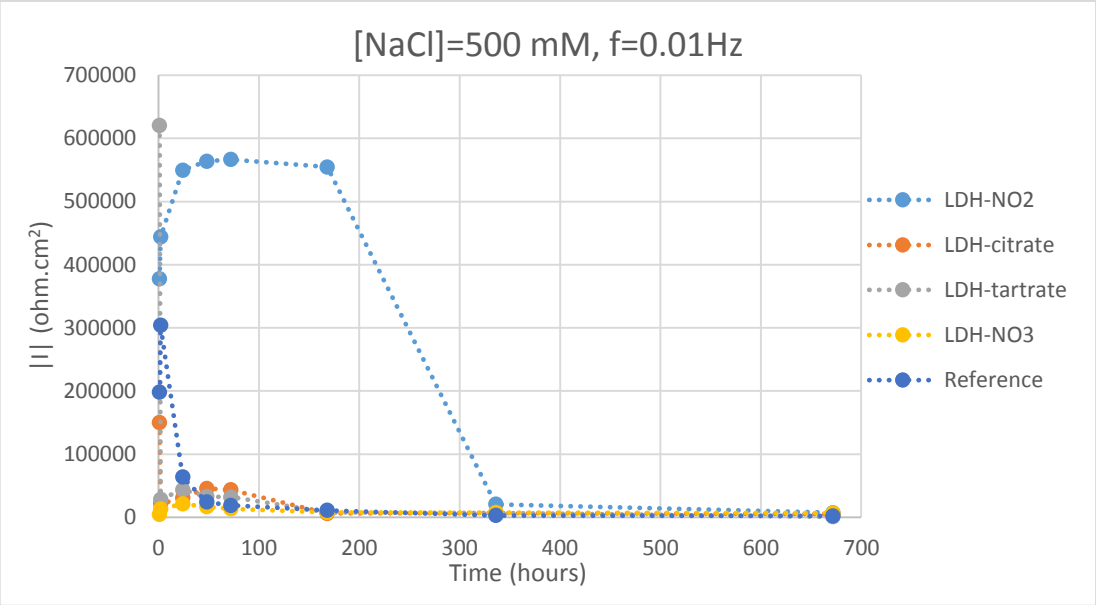

Figure 42: Impedance versus time at constant frequency for: LDH-NO_2 (light blue), LDH-citrate (orange), LDH-tartrate (grey), LDH-NO_3 (yellow) and reference-NaCl solution at 500mM (dark blue).

4. Conclusions and Prospects

The main goal of this work was to prepare and characterize layered double hydroxides intercalated with corrosion inhibitors (nitrite, citrate and tartrate) and investigate their performance as anti-corrosive protectors in reinforced concrete. Therefore, the synthesis of LDH-NO_3 (base material) and LDH-NO_2 (one of the intercalated inhibitor) was proceeded by co-precipitation and the intercalation of citrate and tartrate ions was performed using LDH-NO_3 (base material). The materials were characterized using several techniques, which revealed a successful intercalation of the active species. Release and electrochemical impedance studies were developed in sodium chloride solutions to evaluate the performance of the inhibitors. When analysing the release studies, it was concluded that for higher NaCl concentrations, the released amount of inhibitor was superior. The quantity of inhibitor released was bigger for nitrite, followed by citrate and tartrate. The release of citrate was found to be more irregular than the others, as the release of nitrite and tartrate showed an increase during the first hours and an eventual stabilization overtime. The electrochemical impedance studies demonstrated that nitrite was the inhibitor to provide a better protection. Citrate and tartrate offer also some protection, mainly, at lower NaCl concentrations.

The release and performance studies were performed in solution, allowing the results to be more immediate. It would be more realistic to integrate the intercalated LDHs into a concrete mixture and expose small concrete samples to the same aggressive conditions. Knowing that the inhibitors displacement is stimulated by the presence of another anionic species capable of permute, it would

be expected a slower release of the inhibitors in concrete comparing to the release in solution. In the concrete mixture, chloride ions take more time to penetrate and the corrosive process would be also prolonged due to the slower entrance of the aggressive species into concrete structure.

Functionalization was performed to assess the advantages of encapsulating the inhibitors for a prolonged release to the surroundings. In section 3.2., it was explained the procedure and the information about the characterization. It was followed one procedure, varying the concentration of the reactants and the medium (aqueous to ethanoic). When used an aqueous medium, TEOS hydrolysis occurs very quickly and there is no control in the process. Therefore, it was used ethanol as solvent to slow down the process of hydrolysis and condensation of TEOS and allow a more controlled formation of the silica nanocapsules. FT-IR spectra and SEM images showed the uncertainty towards the success of the encapsulation. Thus, it would be necessary to assess new trials for the encapsulation. Only LDH-NO_3 and LDH-citrate were encapsulated and it was not possible to test their release and performance profiles, due to lack of time. Therefore, it would be auspicious for the work to encapsulate all LDHs intercalated with the inhibitory species, test them in solution and integrate them in a concrete mixture, in order to evaluate the effect of encapsulation in the release and inhibitory profiles.

To conclude, this work allowed to verify if the inclusion of these new corrosion inhibitors into reinforced concrete's mixture, would protect the steel structure from corrosion symptoms for longer periods. Although the thesis plan included the test of concrete samples with the inhibitor additives incorporated, there was not the opportunity to do so, during available time. Nevertheless, now, there is more detailed information about which inhibitors should be investigated in concrete mixtures for further conclusions.

5. References

[1] L. Raki, J. J. Beaudoin, and L. Mitchell, "Layered double hydroxide-like materials: Nanocomposites for use in concrete," *Cem. Concr. Res.*, vol. 34, no. 9, pp. 1717–1724, 2004.

[2] F. Li and X. Duan, "Applications of Layered Double Hydroxides," *Struct. Bond.*, vol. 119, no. September 2005, pp. 193–223, 2006.

[3] C. Forano, U. Costantino, V. Prévot, and C. T. Gueho, *Chapter 14.1 - Layered Double Hydroxides (LDH)*, vol. 5. 2013.

[4] T. L. P. Galvão, C. S. Neves, A. P. F. Caetano, F. Maia, D. Mata, E. Malheiro, M. J. Ferreira, A. C. Bastos, A. N. Salak, J. R. B. Gomes, J. Tedim, and M. G. S. Ferreira, "Control of crystallite and particle size in the synthesis of layered double hydroxides: Macromolecular insights and a complementary modeling tool," *J. Colloid Interface Sci.*, vol. 468, pp. 86–94, 2016.

[5] L. P. F. Benício, R. A. Silva, J. A. Lopes, D. Eulálio, R. M. M. dos Santos, L. A. de Aquino, L. Vergütz, R. F. Novais, L. M. da Costa, F. G. Pinto, J. Tronto, L. P. F. Benício, R. A. Silva, J. A. Lopes, D. Eulálio, R. M. M. dos Santos, L. A. de Aquino, L. Vergütz, R. F. Novais, L. M. da Costa, F. G. Pinto, and J. Tronto, "Layered Double Hydroxides: Nanomaterials for Applications in Agriculture," *Rev. Bras. Ciência do Solo*, vol. 39, no. 1, pp. 1–13, Feb. 2015.

[6] J. He, M. Wei, B. Li, Y. Kang, D. G. Evans, and X. Duan, "Preparation of layered double hydroxides," in *Struct. Bond.*, vol. 119, Beijing: Springer-Verlag, 2006, pp. 89–119.

[7] Y. Kuang, L. Zhao, S. Zhang, F. Zhang, M. Dong, and S. Xu, "Morphologies, preparations and applications of layered double hydroxide micro-/nanostructures," *Materials (Basel).*, vol. 3, no. 12, pp. 5220–5235, 2010.

[8] J. A. Gursky, S. D. Blough, C. Luna, C. Gomez, A. N. Luevano, and E. A. Gardner, "Particle-particle interactions between layered double hydroxide nanoparticles," *J. Am. Chem. Soc.*, vol. 128, no. 26, pp. 8376–8377, 2006.

[9] G. Hu, N. Wang, D. O'Hare, and J. Davis, "One-step synthesis and AFM imaging of hydrophobic LDH monolayers," *Chem. Commun. (Camb).*, vol. 1, no. 3, pp. 287–289, 2006.

[10] Z. P. Xu, G. S. Stevenson, C.-Q. Lu, G. Q. M. Lu, P. F. Bartlett, and P. P. Gray, "Stable suspension of layered double hydroxide nanoparticles in aqueous solution," *J. Am. Chem. Soc.*, vol. 128, no. 1, pp. 36–37, 2006.

[11] X. Lei, L. Yang, F. Zhang, D. G. Evans, and X. Duan, "Synthesis of Oriented Layered Double Hydroxide Thin Films on Sulfonated Polystyrene Substrates," *Chem. Lett.*, vol. 34, no. 12, pp. 12–13, 2005.

[12] D. R. Hines, S. A. Solin, U. Costantino, and M. Nocchetti, "Physical properties of fixed-charge layer double hydroxides," *Phys. Rev. B*, vol. 61, no. 17, pp. 348–358, 2000.

[13] Y. Lin, D. Li, D. G. Evans, and X. Duan, "Modulating effect of Mg-Al-CO 3 layered double hydroxides on the thermal stability of PVC resin," *Polym. Degrad. Stab.*, vol. 88, pp. 286–293, 2005.

[14] C. Nyambo, E. Kandare, and C. A. Wilkie, "Thermal stability and flammability characteristics of ethylene vinyl acetate (EVA) composites blended with a phenyl phosphonate-intercalated layered double hydroxide (LDH), melamine polyphosphate and / or boric acid," *Polym. Degrad. Stab.*, vol. 94, no. 4, pp. 513–520, 2009.

[15] E. Li, Z. Ping, and V. Rudolph, "Applied Catalysis B : Environmental MgCoAl – LDH derived heterogeneous catalysts for the ethanol transesterification of canola oil to biodiesel," *Appl. Catal. B Environ.*, vol. 88, pp. 42–49, 2009.

[16] A. I. Tsyganok, M. Inaba, T. Tsunoda, K. Suzuki, K. Takehira, and T. Hayakawa, "Combined partial oxidation and dry reforming of methane to synthesis gas over noble metals supported on Mg – Al mixed oxide," *Appl. Catal. A Gen.*, vol. 275, pp. 149–155, 2004.

[17] Y. Yuan and W. Shi, "Applied Clay Science A novel LDH nano fi ller intercalated by silsesquioxane for preparing organic / inorganic hybrid composites," *Appl. Clay Sci.*, vol. 67–68, pp. 83–90, 2012.

[18] B. Manoranjan and M. Lakshmi, "The first example of Michael addition catalysed by modified Mg – Al hydrotalcite," *J. Mol. Catal. A Chem.*, vol. 146, pp. 279–284, 1999.

[19] S. Kerchiche, "New way for iron introduction in LDH matrix used as catalysts for Friedel – Crafts reactions," *Arab. J. Chem.*, 2012.

[20] F. L. Theiss, G. A. Ayoko, and R. L. Frost, "Iodide removal using LDH technology," *Chem. Eng. J.*, vol. 296, pp. 300–309, 2016.

[21] D. E. Sparks, T. Morgan, P. M. Patterson, S. A. Tackett, E. Morris, and M. Crocker, "New sulfur adsorbents derived from layered double hydroxides I : Synthesis and COS adsorption," vol. 82, pp. 190–198, 2008.

[22] S. Iftekhar, V. Srivastava, and M. Sillanpää, "Synthesis and Application of LDH Intercalated Cellulose Nanocomposite for Separation of Rare Earth Elements (REEs)," *Chem. Eng. J.*, 2016.

[23] L. N. M. Ribeiro, A. C. S. Alcântara, M. Darder, P. Aranda, F. M. Araújo-Moreira, and E. Ruiz-Hitzky, "Pectin-coated chitosan – LDH bionanocomposite beads as potential systems for colon-targeted drug delivery," *Int. J. Pharm.*, vol. 463, no. 1, pp. 1–9, 2014.

[24] D. G. Evans and X. Duan, "Preparation of layered double hydroxides and their applications as additives in polymers , as precursors to magnetic materials and in biology and medicine," *Chem. Commun.*, pp. 485–496, 2006.

[25] J. Choy, S. Choi, J. Oh, and T. Park, "Clay minerals and layered double hydroxides for novel

biological applications," *Appl. Clay Sci.*, vol. 36, pp. 122–132, 2007.

[26] S. Zheng and J. Li, "Inorganic – organic sol gel hybrid coatings for corrosion protection of metals," *J. Sol-Gel Sci Technol*, vol. 54, pp. 174–187, 2010.

[27] D. Snihirova, L. Liphardt, G. Grundmeier, and F. Montemor, "Electrochemical study of the corrosion inhibition ability of ' smart ' coatings applied on AA2024," *J. Solid State Electrochem*, vol. 17, no. 8, pp. 2183–2192, 2013.

[28] J. W. Boclair and P. S. Braterman, "Layered double hydroxide stability. 1. Relative stabilities of layered double hydroxides and their simple counterparts.," *Chem. Mater.*, vol. 11, no. 2, pp. 298–302, 1999.

[29] J. G. Cabrera and R. Rivera-Villarreal, Eds., *International Conference on the Role of Admixtures in High Performance Concrete*. Monterrey, Mexico: Rilem Publications S.A.R.L, 1999.

[30] J. Seurre, B. Pellerin, and J.-P. Bigas, "US 2012/0059090 A1:ADJUVANT SYSTEM FOR PREFABRICATED CONCRETE," 2012.

[31] T. Angelskar, H. Gebhardt, B. Leikauf, and V. Mader, "US5997630: CONCRETE ACCELERATORS," 1999.

[32] I. Biczock, "Concrete Corrosion Concrete Protection," *Chem. Publ.*, vol. 4, p. 543, 1967.

[33] S. K. Poznyak, J. Tedim, L. M. Rodrigues, A. N. Salak, M. L. Zheludkevich, L. F. P. Dick, and M. G. S. Ferreira, "Novel inorganic host layered double hydroxides intercalated with guest organic inhibitors for anticorrosion applications.," *ACS Appl. Mater. Interfaces*, vol. 1, no. 10, pp. 2353–62, Oct. 2009.

[34] T. A. Söylev and M. G. Richardson, "Corrosion inhibitors for steel in concrete: State-of-the-art report," *Constr. Build. Mater.*, vol. 22, no. 4, pp. 609–622, 2008.

[35] P. Pedeferri, L. Bertolini, B. Elsener, E. Redaelli, R. B. Polder, P. Pedeferri, E. Redaelli, and R. B. Polder, *Corrosion of Steel in Concrete - Prevention, Diagnosis, Repair*. 2013.

[36] Z. Yang, H. Fischer, and R. Polder, "Modified hydrotalcites as a new emerging class of smart additive of reinforced concrete for anticorrosion applications: A literature review," *Mater. Corros.*, vol. 64, no. 12, pp. 1066–1074, 2013.

[37] A. Bentur, N. Berke, and S. Diamond, *Steel Corrosion in Concrete: Fundamentals and civil engineering practice*. CRC Press, 1998.

[38] M. Ormellese, P. Milano, S. Goidanich, P. Milano, G. Fumagalli, P. Milano, P. Milano, M. Ormellese, L. Lazzari, S. Goidanich, G. Fumagalli, and A. Brenna, "A study of organic substances as inhibitors for chloride-induced corrosion in concrete in concrete," *Corros. Sci.*, vol. 51, no. March 2016, pp. 2959–2968, 2009.

[39] T. Thi Xuan Hang, T. A. Truc, T. H. Nam, V. K. Oanh, J. B. Jorcin, and N. Pébère, "Corrosion

protection of carbon steel by an epoxy resin containing organically modified clay," *Surf. Coatings Technol.*, vol. 201, no. 16–17, pp. 7408–7415, 2007.

[40] H. Hayatdavoudi and M. Rahsepar, "Smart inhibition action of layered double hydroxide nanocontainers in zinc-rich epoxy coating for active corrosion protection of carbon steel substrate," *J. Alloys Compd.*, vol. 711, pp. 560–567, 2017.

[41] H. Geng, P. Duan, W. Chen, and Z. Shui, "Carbonation of sulphoaluminate cement with layered double hydroxides," *J. Wuhan Univ. Technol. Mater. Sci. Ed.*, vol. 29, no. 1, pp. 97–101, 2014.

[42] F. Zhang, M. Sun, S. Xu, L. Zhao, and B. Zhang, "Fabrication of oriented layered double hydroxide films by spin coating and their use in corrosion protection," *Chem. Eng. J.*, vol. 141, no. 1–3, pp. 362–367, 2008.

[43] D. Li, F. Wang, X. Yu, J. Wang, Q. Liu, P. Yang, Y. He, Y. Wang, and M. Zhang, "Anticorrosion organic coating with layered double hydroxide loaded with corrosion inhibitor of tungstate," *Prog. Org. Coatings*, vol. 71, no. 3, pp. 302–309, 2011.

[44] M. L. Zheludkevich, D. G. Shchukin, K. A. Yasakau, H. Möhwald, and M. G. S. Ferreira, "Anticorrosion Coatings with Self-Healing Effect Based on Nanocontainers Impregnated with Corrosion Inhibitor," *Chem. Mater.*, vol. 100, no. 5, pp. 402–411, 2007.

[45] R. Harrison, L. Li, Z. Gu, and Z. P. Xu, "Controlling mesoporous silica-coating of layered double hydroxide nanoparticles for drug control release," *Microporous Mesoporous Mater.*, vol. 238, pp. 97–104, 2017.

[46] H. Günzler and A. Williams, *Handbook of Analytical Techniques*, vol. 1–2. 2008.

[47] L. Gray and B. R. Appleman, "EIS: Electrochemical Impedance Spectroscopy," *J. Prot. Coatings Linings*, vol. 20, no. 2, pp. 66–74, 2003.

[48] R. Anbarasan, W. D. Lee, and S. S. Im, "Adsorption and intercalation of anionic surfactants onto layered double hydroxides—XRD study," *Bull. Mater. Sci.*, vol. 28, no. 2, pp. 145–149, 2005.

[49] Y. Shen, X. Zhao, X. Zhang, S. Li, D. Liu, and L. Fan, "Removal of Cu2+ from the aqueous solution by tartrate intercalated layered double hydroxides," *Desalin. Water Treat.*, vol. 33, no. 1, pp. 159–169, 2014.

[50] D. A. Islam, D. Borah, and H. Acharya, "Controlled synthesis of monodisperse silver nanoparticles supported layered double hydroxide catalyst," *RSC Adv.*, vol. 5, no. 17, pp. 13239–13245, 2015.

[51] J. Perera, M. Weerasekera, and N. Kottegoda, "Slow release anti-fungal skin formulations based on citric acid intercalated layered double hydroxides nanohybrids.," *Chem. Cent. J.*, vol. 9, p. 27, 2015.

[52] S. H. Kim, W. Il Lee, and J. M. Park, “Assessment of dispersion in carbon nanotube reinforced composites using differential scanning calorimetry,” *Carbon N. Y.*, vol. 47, no. 11, pp. 2699–2703, 2009.

[53] S. Bhattacharjee, “DLS and zeta potential - What they are and what they are not?,” *J. Control. Release*, vol. 235, pp. 337–351, 2016.

[54] “http://www.lsinstruments.ch/technology/dynamic_light_scattering_dls/.” .

[55] D. Mahl, J. Diendorf, W. Meyer-Zaika, and M. Epple, “Possibilities and limitations of different analytical methods for the size determination of a bimodal dispersion of metallic nanoparticles,” *Colloids Surfaces A Physicochem. Eng. Asp.*, vol. 377, no. 1–3, pp. 386–392, 2011.

[56] M. Rehkämper, M. Schönbächler, and C. H. Stirling, “Multiple collector ICP-MS: Introduction to instrumentation, measurement techniques and analytical capabilities,” *Geostand. Newsl.*, vol. 25, no. 1, pp. 23–40, 2001.

[57] “https://www.fei.com/introduction-to-electron-microscopy/sem/.” .

[58] W. Zhou and Z. L. Wang, Eds., *Scanning Microscopy for Nanotechnology: Techniques and Applications*. New York: Springer US, 2007.

[59] C. Forano, T. Hibino, F. Leroux, and C. Taviot-Guého, “Chapter 13.1 Layered Double Hydroxides,” in *Handbook of Clay Science*, vol. 1, no. C, 2006, pp. 1021–1095.

[60] F. Z. Mahjoubi, A. Khalidi, M. Abdennouri, and N. Barka, “Zn–Al layered double hydroxides intercalated with carbonate, nitrate, chloride and sulfate ions: Synthesis, characterization and dyes removal properties,” *J. Taibah Univ. Sci.*, vol. 11, no. 1, pp. 90–100, 2015.

[61] S. Tezuka, R. Chitrakar, A. Sonoda, K. Ooi, and T. Tomida, “Studies on selective adsorbents for oxo-anions. Nitrate ion-exchange properties of layered double hydroxides with different metal atoms,” *Green Chem.*, vol. 6, no. 2, pp. 104–109, 2004.

[62] J. Xu, Y. Song, Q. Tan, and L. Jiang, “Chloride absorption by nitrate, nitrite and aminobenzoate intercalated layered double hydroxides,” *J. Mater. Sci.*, vol. 52, no. 10, pp. 5908–5916, 2017.

[63] V. Prevot, C. Forano, J. P. Besse, and F. Abraham, “Syntheses and Thermal and Chemical Behaviors of Tartrate and Succinate Intercalated Zn(3)Al and Zn(2)Cr Layered Double Hydroxides.,” *Inorg. Chem.*, vol. 37, no. 17, pp. 4293–4301, 1998.

[64] E. Conterosito, L. Palin, D. Antonioli, D. Viterbo, E. Mugnaioli, U. Kolb, L. Perioli, M. Milanesio, and V. Gianotti, “Structural Characterisation of Complex Layered Double Hydroxides and TGA-GC-MS Study on Thermal Response and Carbonate Contamination in Nitrate- and Organic-Exchanged Hydrotalcites,” *Chem. - A Eur. J.*, vol. 21, no. 42, pp. 14975–14986, 2015.

[65] Z. P. Xu and H. C. Zeng, “Decomposition pathways of hydrotalcite-like compounds Mg1-xAlx(OH)2(NO3) x.nH2O as a continuous function of nitrate anions,” *Chem. Mater.*, vol. 13, no. 12, pp. 4564–4572, 2001.

[66] J. Gao, Y. Wang, and H. Hao, “Investigations on dehydration processes of trisodium citrate hydrates,” *Front. Chem. Sci. Eng.*, vol. 6, no. 3, pp. 276–281, 2012.

[67] L. Y. Wang, G. Q. Wu, and D. G. Evans, “Synthesis and characterization of a layered double hydroxide containing an intercalated nickel(II) citrate complex,” *Mater. Chem. Phys.*, vol. 104, no. 1, pp. 133–140, 2007.

[68] A. C. Bertoli, “Estudos teóricos, espectroscópicos e identificação via ESI-MS de complexos citrato: metal (Cd2+, Pb2+, Cu2+, Zn2+ e Fe2+) em solução aquosa,” Universidade Federal de Lavras, 2014.

[69] W. Zhang, J. He, and C. Guo, “Second staging of tartrate and carbonate anions in Mg-Al layered double hydroxide,” *Appl. Clay Sci.*, vol. 39, no. 3–4, pp. 166–171, 2008.

[70] J. Madejová, “FTIR techniques in clay mineral studies,” *Vib. Spectrosc.*, vol. 31, no. 1, pp. 1–10, 2003.

[71] C. S. Brazel and N. A. Peppas, “Modeling of drug release from swellable polymers,” *Eur. J. Pharm. Biopharm.*, vol. 49, no. 1, pp. 47–58, 2000.

[72] P. L. Ritger and N. A. Peppas, “A simple equation for description of solute release I. Fickian and non-fickian release from non-swellable devices in the form of slabs, spheres, cylinders or discs,” *J. Control. Release*, vol. 5, no. 1, pp. 23–36, 1987.

[73] J. Siepmann and N. A. Peppas, “Higuchi equation: Derivation, applications, use and misuse,” *Int. J. Pharm.*, vol. 418, no. 1, pp. 6–12, 2011.

[74] F.-C. Wu, R.-L. Tseng, S.-C. Huang, and R.-S. Juang, “Characteristics of pseudo-second-order kinetic model for liquid-phase adsorption: A mini-review,” *Chem. Eng. J.*, vol. 151, no. 1–3, pp. 1–9, 2009.

[75] Y.-S. Ho, “Review of second-order models for adsorption systems,” *J. Hazard. Mater.*, vol. 136, no. 3, pp. 681–689, 2006.

Appendix

A. Calibration Curves

As it was mentioned in section 2.6., calibration curves obtained with nitrite, citrate and tartrate standard solutions were traced. Aqueous solutions were prepared of each specie and aliquots of 1 or 2 mL were fulfilled with the corresponding NaCl solution.

For each concentration exists one curve for each inhibitor, thus, the total of curves is 9.

Starting by the lower NaCl concentration – 5mM:

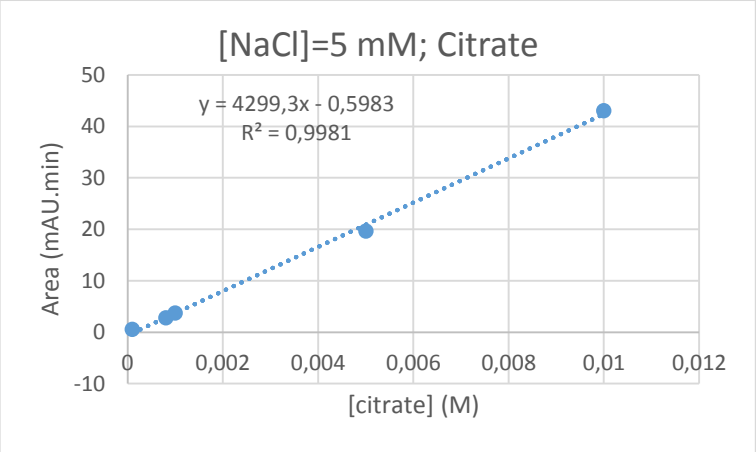

Figure A. 1: Calibration curve for citrate in a 5 mM NaCl solution.

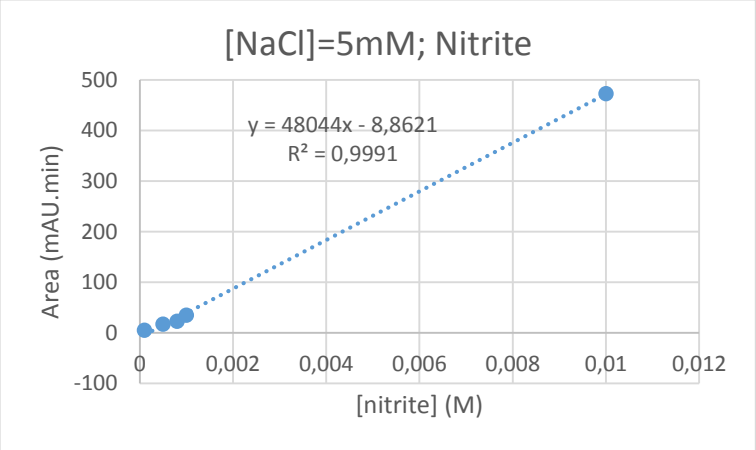

Figure A. 2: Calibration curve for nitrite in a 5 mM NaCl solution.

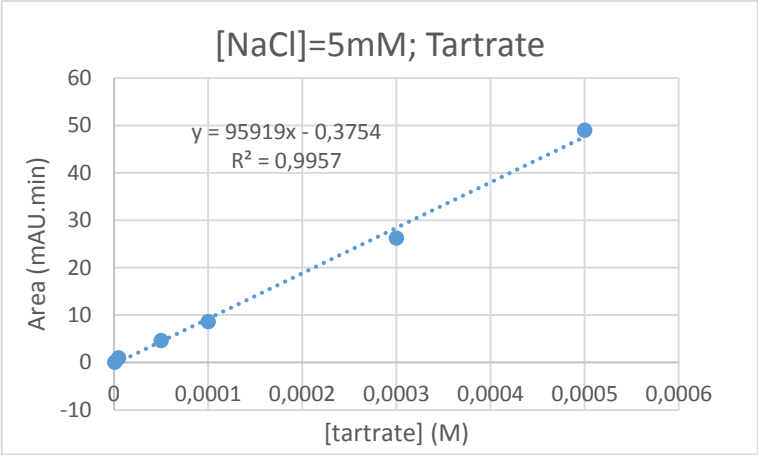

Figure A. 3: Calibration curve for tartrate in a 5 mM NaCl solution.

For the intermediate NaCl concentration – 50mM:

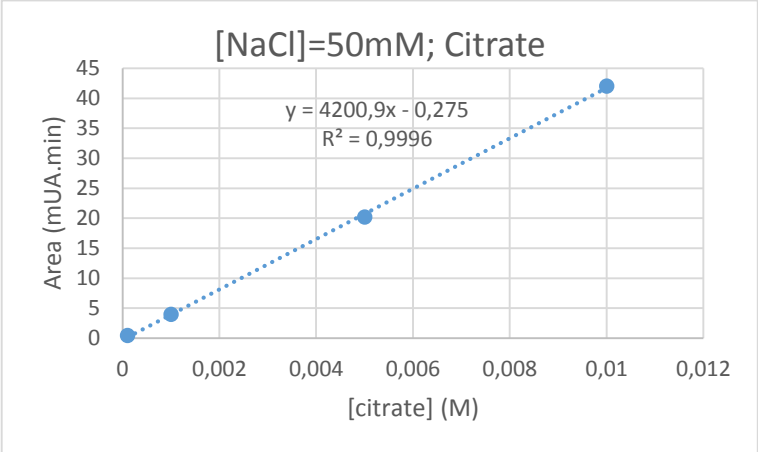

Figure A. 4: Calibration curve for citrate in a 50 mM NaCl solution.

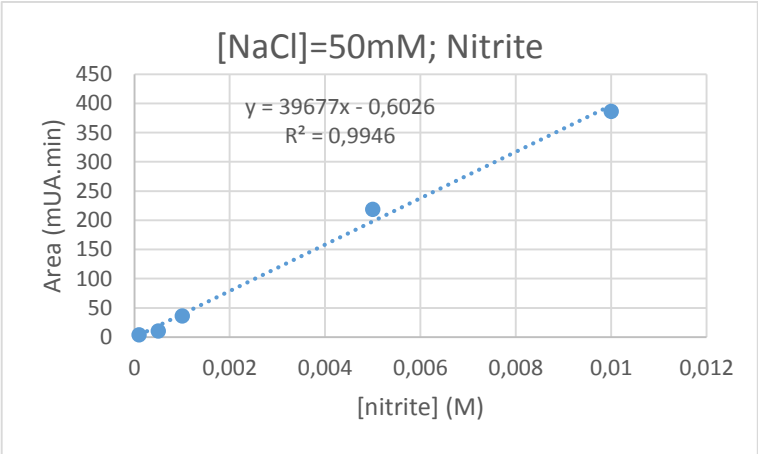

Figure A. 5: Calibration curve for nitrite in a 50 mM NaCl solution.

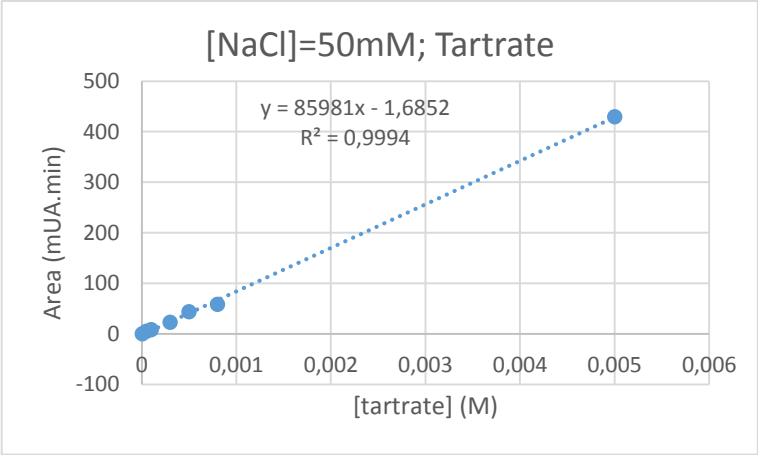

Figure A. 6: Calibration curve for tartrate in a 50 mM NaCl solution.

Lastly, for the higher concentration in chloride – 500mM:

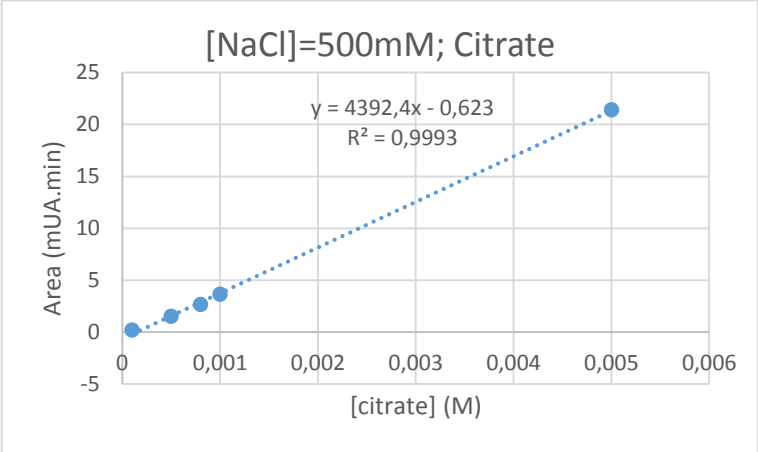

Figure A. 7: Calibration curve for citrate in a 500 mM NaCl solution.

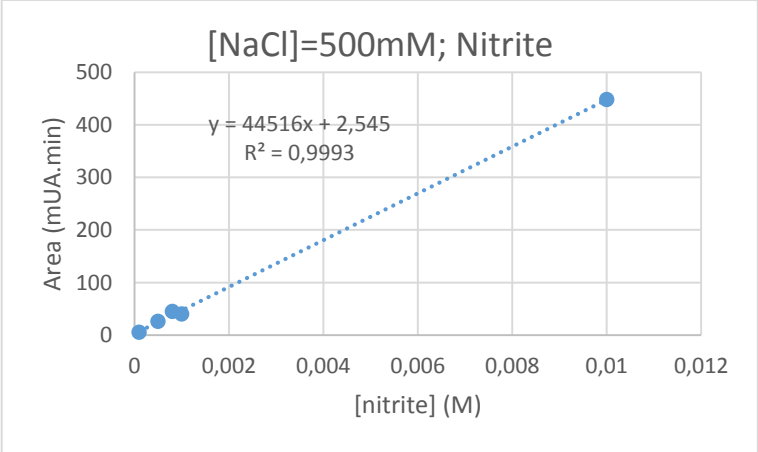

Figure A. 8: Calibration curve for nitrite in a 500 mM NaCl solution.

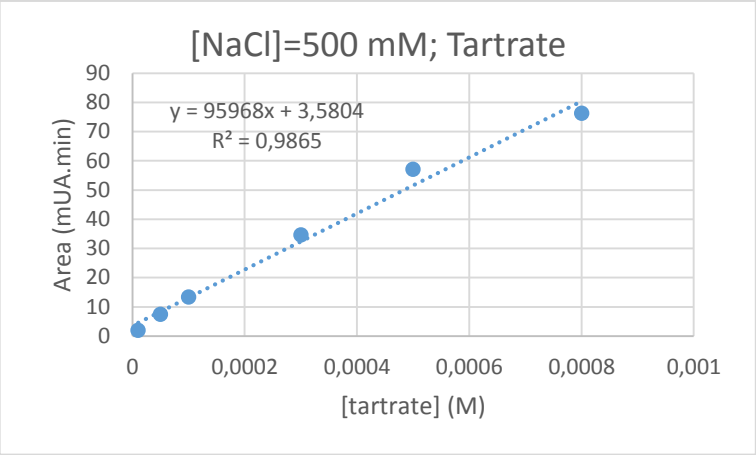

Figure A. 9: Calibration curve for tartrate in a 500 mM NaCl solution.

B. Kinetic Models

The kinetic models studied were explained with detail in section 3.2.1. and behind each, there is a mathematical treatment implied.

B.1. Nitrite's release fittings

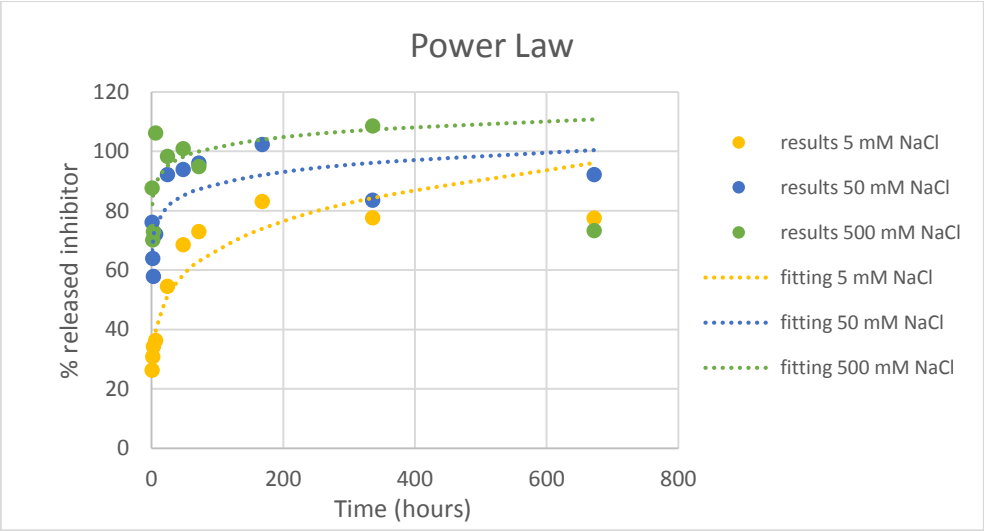

Figure B. 1: Fitting of experimental data of nitrite's release using Power Law.

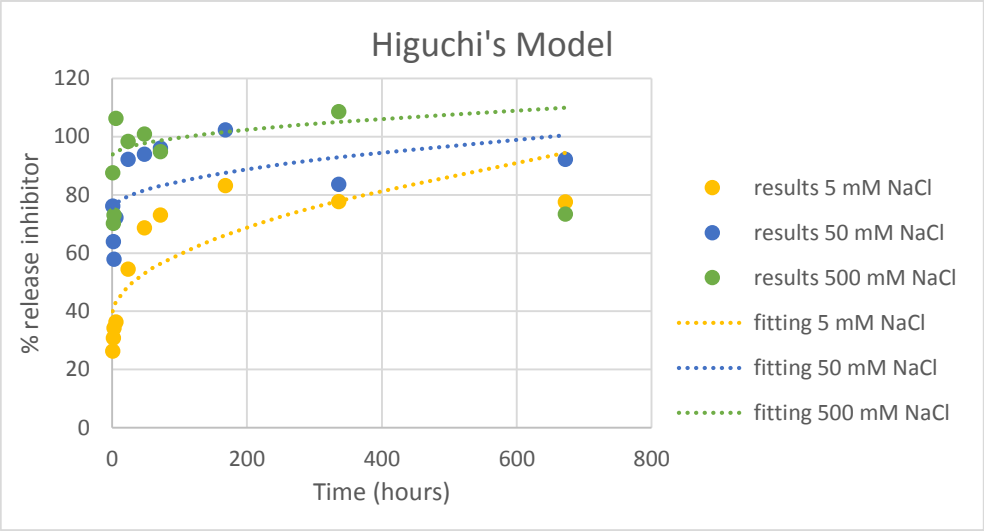

Figure B. 2: Fitting of experimental data of nitrite's release using Higuchi's square root of time (diffusion model).

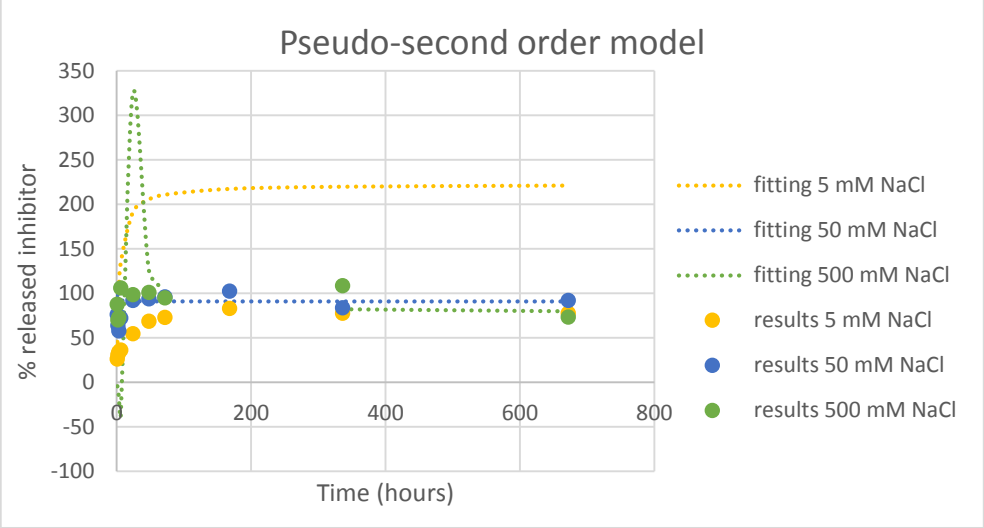

Figure B. 3: Fitting of experimental data of nitrite's release using Pseudo-second order.

B.2. Citrate's release fittings

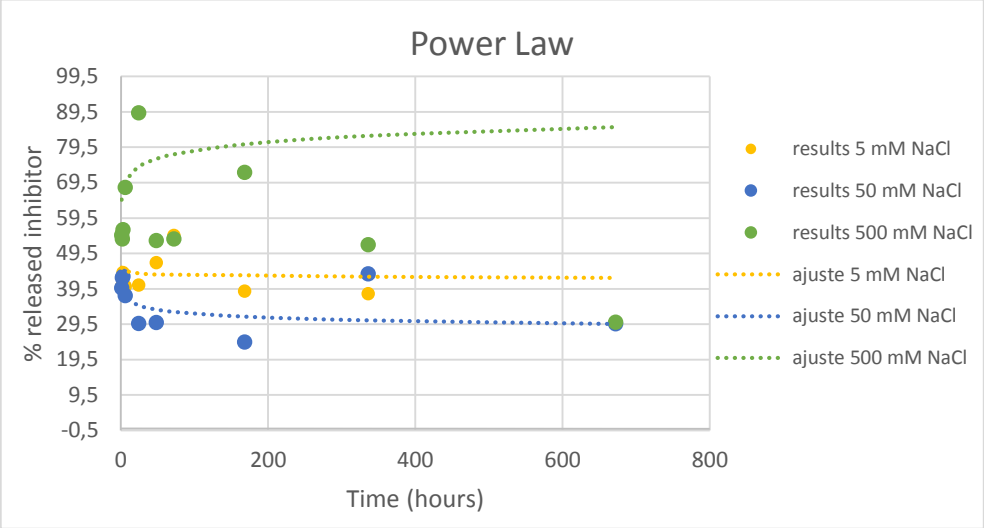

Figure B. 4: Fitting of experimental data of citrate's release using Power Law.

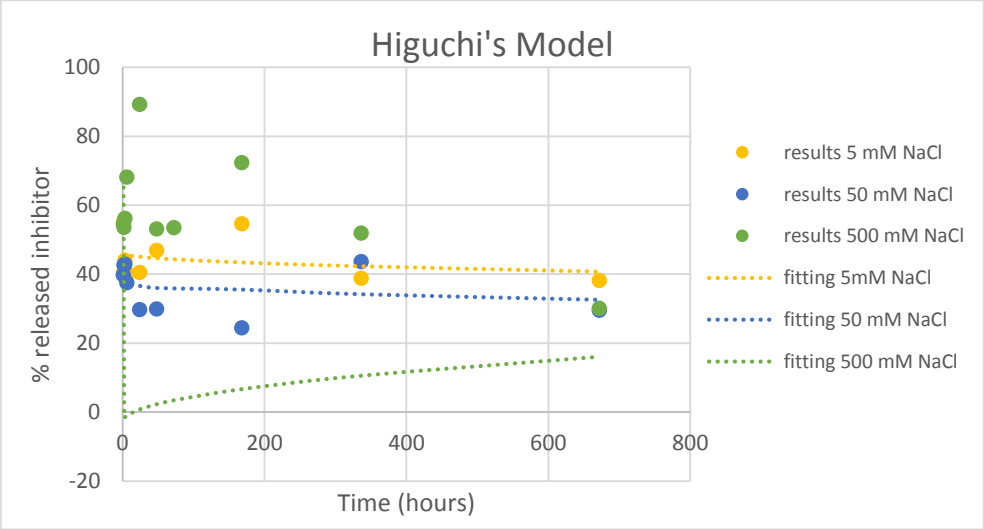

Figure B. 5: Fitting of experimental data of citrate's release using Higuchi's square root of time (diffusion model).

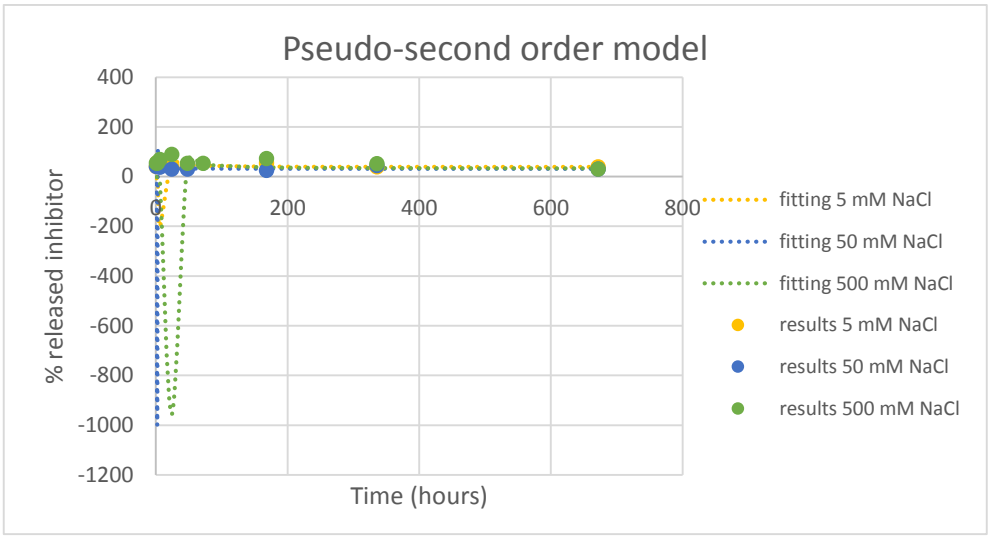

Figure B. 6: Fitting of experimental data of citrate's release using Pseudo-second order model.

B.3. Tartrate's release fittings

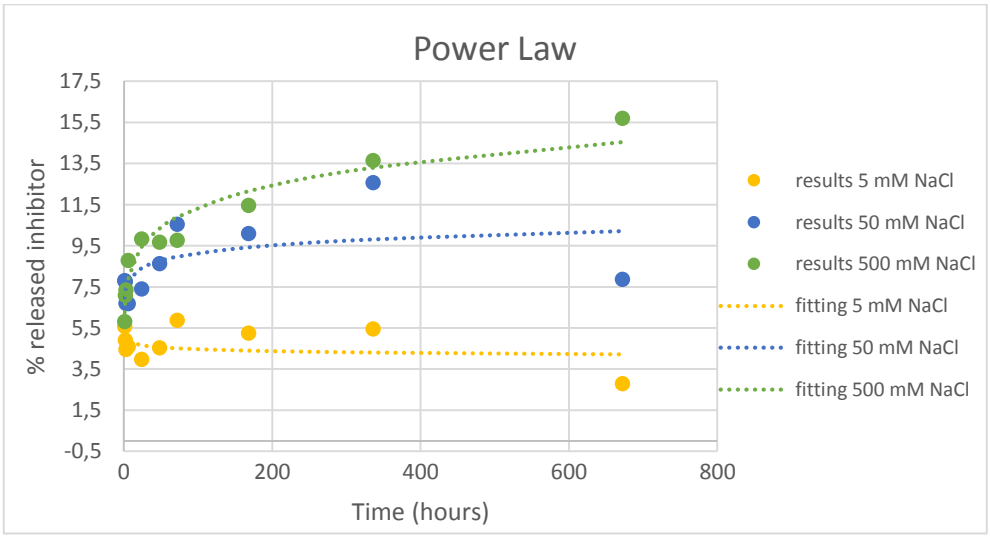

Figure B. 7: Fitting of experimental data of tartrate's release using Power Law.

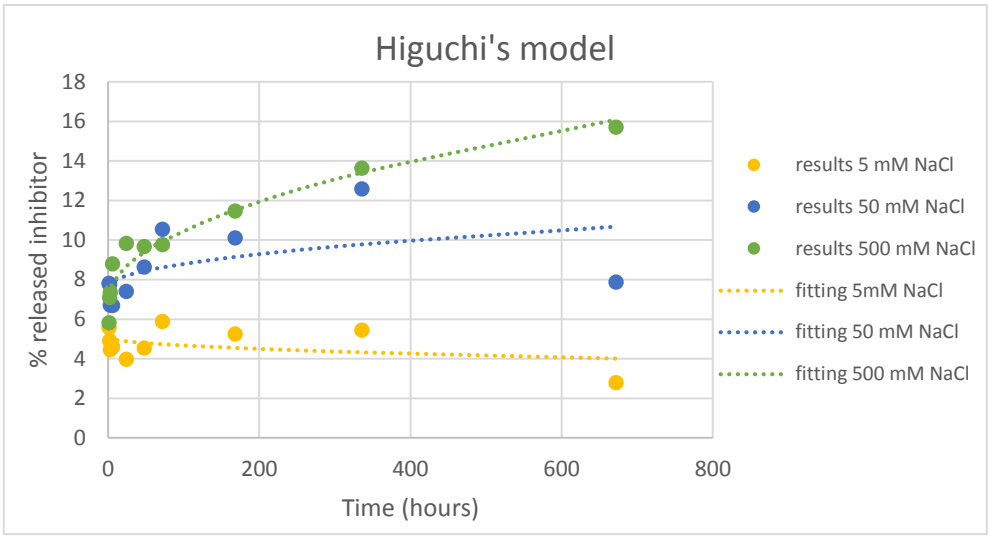

Figure B. 8: Fitting of experimental data of tartrate's release using Higuchi's square root of time (diffusion model).

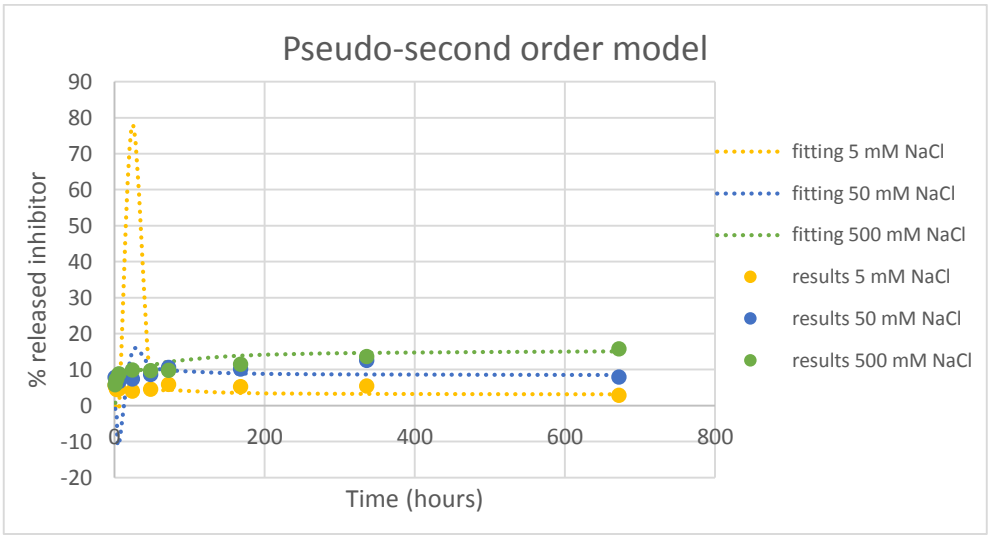

Figure B. 9: Fitting of experimental data of tartrate's release using Pseudo-second order model.